

Novel Sensing Technology and Mesoscale Modelling Approaches for Meteorological Investigations over a Mining Facility

by
Amir Nazem

A Thesis
presented to
The University of Guelph

In partial fulfilment of requirements
for the degree of
Master of Sciences
in
Engineering

Guelph, Ontario, Canada
© Amir Nazem, August, 2019

ABSTRACT

NOVEL SENSING TECHNOLOGY AND MESOSCALE MODELLING APPROACHES FOR METEOROLOGICAL INVESTIGATIONS OVER A MINING FACILITY

Amir Nazem

University of Guelph, 2019

Advisor:

Dr. Amir A. Aliabadi

This thesis investigates two distinctive experimental and numerical approaches to study meteorological dynamics over a complex open-pit mining facility in northern Canada. In the first approach, a novel airborne sensing instrument capable of measuring vertical profiles of atmospheric boundary layer variables, such as temperature, wind velocity components, pressure, and relative humidity, is designed, tested, and calibrated in a wind tunnel. The instrument is then successfully operated in an environmental field campaign measuring meteorological dynamics over the mining facility in May 2018. In the second approach, a numerical weather prediction system, Weather and Research Forecast (WRF) model, is adapted with topographical and land use changes over the mining facility to simulate meteorological dynamics over the mining facility. The adaptation of the WRF model for this application is novel and resulted in better numerical predictions of meteorological dynamics over the mining facility. This thesis makes a contribution toward better understanding of meteorological processes over open-pit mining facilities using new experimental and numerical methodologies.

Acknowledgements

This work could not be completed without the consistent and passionate guidelines from Dr. Amir A. Aliabadi. I would like to express my thanks to Dr. David W. Lubitz for his guidance in supporting the wind tunnel experiments and the extensive time he invested to help me decipher the governing equations of Weather Research and Forecasting (WRF).

Completing this work would not be possible without the technical support of Rowan Williams Davies and Irwin Inc. (RWDI) and financial support from the Discovery Grant program (401231) from the Natural Sciences and Engineering Research Council (NSERC) of Canada, Government of Ontario through the Ontario Centres of Excellence (OCE) under the Alberta-Ontario Innovation Program (AOIP) (053450), and Emission Reduction Alberta (ERA) (053498).

I pay special gratitude to my parents who have supported me throughout my years of education both emotionally and financially. Finally, I am extremely thankful to my family members and friends for their unconditional love, support, and blessings throughout my life.

Dedication

I would like to dedicate the present work to the ambitious and successful mind, Elon Reeve Musk. Without a shadow of doubt, his orchestra of success inspire and motivate wanderers all over this planet.

Quote

“No one believes the simulation results except the one who performed the calculation, and everyone believes the experimental results except the one who performed the experiment.”

Anonymous

Contents

Abstract	ii
Acknowledgements	iii
Dedication	iv
Quote	v
List of Tables	ix
List of Figures	xiii
List of Abbreviations	xiv
List of Mathematical Symbols	xvi
1 Introduction	1
1.1 The Broad View	1
1.2 How Does This Thesis Fit into the Overall Picture?	2
1.3 Review of Meteorological Sensing Technologies	2
1.4 Review of Numerical Weather Prediction (NWP) Modelling	7
1.5 Objectives	10
1.6 Mining Project, Area Fugitive Emission Measurements and Collaboration De- tails	11
1.7 Thesis Structure	12
1.8 Summary	12
2 Meteorological Measurements from a Tethered and Navigated Air Blimp (TANAB) System	14
2.1 Tethered and Navigated Air Blimp (TANAB) Specification	15
2.2 Gondola Motion	16
2.3 Mini Weather Station	19
2.4 TriSonica TM Mini Calibration	22
2.4.1 Wind Tunnel Test Summary	23

2.4.2	Procedure for Assessing TriSonica™ Mini Performance in Measuring Turbulence Statistics	29
2.5	Procedure for Gondola Calibration	29
2.6	TANAB Field Observation	30
2.7	Summary	31
3	Description of the Weather Research and Forecasting (WRF) Model	32
3.1	Introduction to WRF	32
3.1.1	Vertical Coordinate	33
3.2	Governing Equations	37
3.3	Road Map for Adapting the WRF Model to the Mining Facility	38
3.3.1	PBL Schemes and Physics Models in WRF	40
3.4	Updating the Terrestrial Information	40
3.4.1	The Choice of Static Dataset	41
3.4.2	Adding the SRTM Terrain Data	42
3.4.3	Updating The SRTM Terrain Data with Mining Facility LiDAR Data from 2018	44
3.4.4	Modifying Land Use Classification	46
3.4.5	Updated High Resolution Topography and Land Use Classification	49
3.5	Incorporation of a Lake Model	49
3.5.1	UEMS Predictions Compared with Air Soundings	52
3.6	Conclusions	52
4	Results and Discussion	53
4.1	Part 1: Meteorological Sensing	53
4.1.1	TriSonica™ Mini Performance against Pitot Tube	53
4.1.2	R.M. YOUNG 81000 Performance against Pitot Tube	55
4.1.3	TriSonica™ Mini Performance against R.M. YOUNG 81000	55
4.1.4	TriSonica™ Mini Performance when Mounted on Gondola	57
4.1.5	Calibration Factors	59
4.1.6	TANAB Field Observation	62
4.1.7	Part 1: Conclusions	65
4.2	Part 2: Mesoscale Meteorological Modelling	65
4.2.1	Lake Model Analysis	67
4.2.2	Albedo	68
4.2.3	Surface Emissivity	68
4.2.4	Roughness Length	70
4.2.5	The Effects of Updating the Topography and Land Use Classifications on Wind Vectors	75
4.2.6	The Effects of Updating the Topography and Land Use Classifications on Surface Potential Temperature at 2 m	75

4.2.7	The Effects of Updating the Topography and Land Use Classifications on Surface Relative Humidity at 2 m	76
4.2.8	Model Comparison to Sounding Data	76
4.2.9	Model Comparison to TANAB Data	83
4.2.10	Part 2: Conclusions	83
5	Conclusions and Further Work	87
5.1	Meteorological Sensing	87
5.2	Mesoscale Modelling	88
5.3	Future Work	90
	References	90
A	Source Codes	98
A.1	Fortran Program Converting ASCII to Binary	98
A.2	C Subroutine Converting ASCII to Binary	100
A.3	Linux Command Lines to Compile the Fortran Code	103
A.4	Python Program for Fast Matrix Element Substitution	104
A.5	Python Program Assigning Latitudes and Longitudes to the LiDAR Data . .	106
A.6	The Content of the Index File Created for Feeding High Resolution Terrain Topography to UEMS	108
A.7	Python Program Extracting Background Roughness Length	109
A.8	Python Program Comparing WRFOUT and Soundings (Horizontal Wind Speed)	111
A.9	Python Program Calibrating TriSonica Mini against Pitot Tube	113
B	Published Work	118
B.1	Peer-Reviewed Journal Papers	118
B.2	Refereed Conferences	119
B.3	Poster Presentations	119

List of Tables

2.1	TriSonica™ Mini’s specifications summary [4].	20
2.2	A summary of specifications for wind sensors used in the wind tunnel calibration experiment.	23
2.3	Change in variances and turbulence intensities as a function of the wind tunnel’s wind peed.	25
3.1	The choice of horizontal grid spacing.	39
3.2	The micro physics parameterizations used in the WRF simulations.	41
4.1	Effects of the change in azimuthal angle on TriSonica™ Mini’s performance in measuring mean wind speed calculated in terms of bias, RMSE, and MPE.	54
4.2	Effects of the change in azimuthal angle on R.M. YOUNG 81000 performance in measuring mean wind speed calculated in terms of bias, RMSE, and MPE.	56
4.3	Performance of TriSonica™ Mini in measuring turbulence statistics of wind velocity component compared against R.M. YOUNG 81000 calculated in terms of bias and RMSE.	56
4.4	Effects of the change in azimuthal angle on mounted TriSonica™ Mini performance in measuring mean wind speed calculated in terms of bias and RMSE.	57
4.5	Performance of mounted TriSonica™ Mini in measuring turbulence statistics of wind velocity component compared against R.M. YOUNG 81000 calculated in terms of bias and RMSE.	59
4.6	TriSonica™ Mini’s calibration factors for mean velocity measurements.	60
4.7	TriSonica™ Mini’s calibration factors for turbulence statistics measurements.	60
4.8	TriSonica™ Mini’s calibration factors when mounted on gondola for mean velocity measurements.	61
4.9	TriSonica™ Mini’s calibration factors when mounted on gondola for turbulence statistics measurements.	61
4.10	Davenport classification of effective terrain aerodynamic roughness length-scale; extracted from [33].	73

List of Figures

1.1	The flow chart of the new methodologies to determine the GHG emission fluxes from an open-pit mining facility. This thesis contribution's to the overall methodology is outlined.	3
2.1	The instrument development outlined in the overall project.	15
2.2	Left: TANAB system in operation, right: schematic of gondola assembly with all the sensors onboard.	16
2.3	Positioning of the balloon against the dominant wind direction.	17
2.4	The wind-rose corresponding to 56 hours of flight, reported in the local coordinate system of the sensor. The numbers on the plot indicates the number records collected at 10 Hz.	18
2.5	TANAB and three stabilizing ropes deployed at the mining facility. The system measures in the unstable atmospheric boundary layer.	18
2.6	TANAB and two stabilizing ropes deployed at the mining facility. The system measures in the stable atmospheric boundary layer.	19
2.7	Left: the distribution of pitch angles recorded by TriSonica™ Mini's compass; right: the distribution of roll angles recorded by TriSonica™ Mini's compass.	20
2.8	The TriSonica™ Mini; figure extracted from [4]	21
2.9	Ultrasonic anemometer vector relation; the anemometer measures the time required to transmit a signal to calculate the wind speed; top: transducer/receiver 1 sends the pulse; bottom: Transducer/receiver 2 sends the pulse. . . .	22
2.10	Wind tunnel at the University of Guelph: 1=honeycomb, 2=contraction, 3=test section, 4=diffuser, and 5=fan.	24
2.11	The flow chart representing the wind tunnel test.	24
2.12	Contours of air velocity at four wind levels (2, 4, 6, and 8 m s ⁻¹); the measurement locations are marked on the plots.	25
2.13	Variation in wind speed at each wind level.	26
2.14	Schematic of the experimental setup at wind tunnel. On the right: arrays of same size blocks to introduce turbulence to the flow and on the left: the instrument (shown with plus sign) tested against the Pitot tube (shown as a probe). Considering the contours of wind speed at tunnel's test section area, both the instrument and the Pitot tube were positioned 60 cm from the bottom wall.	26

2.15	The view of TriSonica™ Mini (left) and the Pitot tube (right) in wind tunnel.	27
2.16	Contours of wind velocity at four wind levels (2, 4, 6, and 8 m s ⁻¹) with array of blocks upstream. The measurement locations are marked on the plots. Note, introducing the upstream blocks slightly increases the wind speed at each level compared with the Fig.2.12.	28
2.17	The view of R.M. YOUNG 81000 (left) and Pitot tube (right) at wind tunnel.	29
2.18	The view of gondola and Pitot tube at the wind tunnel.	30
3.1	Mesoscale modelling as it is outlined in the flow chart of the overall project.	33
3.2	Schematic of hybrid-terrain following vertical coordinate system; figure extracted from [62].	34
3.3	Hybrid terrain-following vertical coordinate system.	35
3.4	C-grid staggering; figure extracted from [62]. Ω is the contravariant of the vertical velocity.	36
3.5	Five nested domains and surface elevation.	39
3.6	The road map to update the topography dataset.	41
3.7	The road map to update the land use data set.	42
3.8	Inhomogeneity and discontinuity resulted by adding multiple SRTM tiles; at the border of each tile, series of terrain height inconsistencies appear that are up to 200 m. Note, the source of Inhomogeneity goes back to the SRTM data set.	44
3.9	Aircraft's pathway (red dashed line) over the mining facility as mapped by the ordered LiDAR filenames; note that the LiDAR data is missed in yellow squares. The aircraft started measurements at point 1 and finished at point 2. The numbers in the blocks indicate the LiDAR data filenames.	45
3.10	LiDAR map (processed in ParaView) on top of the mining facility. The extreme top, bottom, left, and right are pin pointed and their corresponding latitude and longitude are identified.	45
3.11	Noise in the data when MODIS Land Use 20-class 15" WPS geogrid binary format is read by Python and is converted to WPS geogrid binary format. The selected tile covers the land between 50° to 60° latitude and -120° to -108° longitude including the mining facility. Note that the re-generated tile is presented adjacent to the original tile. (left: the re-generated tile and right: the original tile)	47
3.12	Original MODIS 15", 20-class product at the mining facility area of interest colour-coded per classifications of Friedl et al. [25], modified in April 2014.	47
3.13	Most recent satellite picture of the mining facility; Google Earth, June 2018.	48
3.14	Colour-coded land use classifications overlaid on the mining facility map with respect to the standard MODIS land classes: Grasslands = 10 (orange), Urban and Built-up = 13 (red), Barren and Sparsely Vegetated = 16 (gray), and Water = 17 (blue) colour-coded per classifications of Friedl et al. [25].	48

3.15	The updated topography, over the mining facility, with the latest LiDAR dataset; figure extracted from [53].	50
3.16	The updated land use classifications; figure extracted from [53].	51
4.1	TriSonica TM Mini's performance in measuring mean wind speed against Pitot tube at different azimuth angles.	54
4.2	R.M. YOUNG 81000 performance in measuring mean wind speed against Pitot tube at different azimuth angles.	55
4.3	TriSonica TM Mini's performance in measuring $\overline{u^2}$ against R.M. YOUNG 81000.	56
4.4	TriSonica TM Mini's performance in measuring $\overline{v^2}$ against R.M. YOUNG 81000.	57
4.5	TriSonica TM Mini's performance in measuring \overline{U} and \overline{V} against Pitot tube when mounted on gondola.	58
4.6	TriSonica TM Mini's performance in measuring $\overline{u^2}$ against R.M. YOUNG 81000 when unmounted and mounted on gondola.	59
4.7	Diurnal variation of the horizontal wind speed; figures extracted from [54].	63
4.8	Diurnal variation of the turbulence kinetic energy; figures extracted from [54].	63
4.9	Diurnal variation of turbulence statistics; figures extracted from [54]	64
4.10	Profiles of turbulence statistics at 4-hr time intervals; figures extracted from [54].	66
4.11	The cross section of the tailings pond used to study the contours of lake temperature.	67
4.12	Contours of lake temperatures at different hours of a day on a cross section located at the middle of the pond; times in Local Standard Time (LST).	69
4.13	Temperature instability across the first lake layer; May 18, 2018 at 1500 LST.	70
4.14	Contours of albedo over the inner domain during the simulation period; times in Local Standard Time (LST)	71
4.15	Surface emissivity during the simulation period; times in Local Standard Time (LST).	72
4.16	Aerodynamic roughness lengthscale during the simulation period; times in Local Standard Time (LST).	74
4.17	Effects of topography and land use classification changes on 10-m horizontal wind velocity magnitude and direction at 0200 LST; left: default topography and land use; right: modified topography and land use; figures are retrieved from [53].	75
4.18	Effects of topography and land use classification changes on 10-m horizontal wind velocity magnitude and direction at 1400 LST; left: default topography and land use; right: modified topography and land use; figures are retrieved from [53].	76
4.19	Effects of topography and land use classification changes on surface potential temperature 2 m at 0200 LST; left: default topography and land use; right: modified topography and land use; figures are retrieved from [53].	77

4.20	Effects of topography and land use classification changes on surface potential temperature 2 m at 1400 LST; left: default topography and land use; right: modified topography and land use; figures are retrieved from [53].	77
4.21	Effects of topography and land use classification changes on surface relative humidity 2 m at 0200 LST; left: default topography and land use; right: modified topography and land use; figures are retrieved from [53].	78
4.22	Effects of topography and land use classification changes on surface relative humidity 2 m at 1400 LST; left: default topography and land use; right: modified topography and land use; figures are retrieved from [53].	78
4.23	The location of sounding stations with respect to the largest model domain in UEMS.	79
4.24	Horizontal wind speed for UEMS and sounding data averaged over three days.	80
4.25	Horizontal wind direction at 00Z; UEMS comparison against sounding data.	81
4.26	Horizontal wind direction at 12Z; UEMS comparison against sounding data.	82
4.27	Water vapor mixing ratio for UEMS and sounding data averaged over three days.	84
4.28	Potential temperature for UEMS and sounding data averaged over three days.	85
4.29	Wind speed comparison of UEMS predictions and TANAB measurements; figure extracted from [53].	86

List of Abbreviations

AOA	Angle of Attack
ABL	Atmospheric Boundary Layer
AFWA	Air Force Weather Agency
ASCII	American Standard Code for Information Interchange
AMS	American Meteorological Society
ARW	Advanced Research WRF
CBL	Convective Boundary Layer
CFD	Computational Fluid Dynamics
CLM	Community Land Model
ECMWF	European Center for Medium-Range Weather Forecasting
FAA	Federal Aviation Administration
FSL	Forecast Systems Laboratory
GEM	Global Environmental Multi scale
GFS	Global Forecast System
GPS	Global Positioning System
IDV	Integrated Data Viewer
LES	Large-Eddy Simulation
LiDAR	Light Detection and Ranging
LST	Local Standard Time

MODIS	MODerate resolution Imaging Spectroradiometer
NCEP	National Centers for Environmental Prediction
NCAR	National Center for Atmospheric Research
NOAA	National Oceanic and Atmospheric Administration
NMM	Non-hydrostatic Mesoscale Mode
NWP	Numerical Weather Prediction
PBL	Planetary Boundary Layer
RADAR	RADio Detection And Ranging
RMSE	Root Mean Squared Error
SBL	Stable Boundary Layer
SODAR	SONic Detection And Ranging
SRTM	Shuttle Radar Topography Mission
SUAV	Small Unit Unmanned Aerial Vehicle
TANAB	Tethered And Navigated Air Blimp
UAS	Unmanned Aircraft System
UAV	Unmanned Aerial Vehicle
UEMS	Unified Environmental Modelling System
USGS	United States Geological Survey
WPS	WRF Preprocessing System
WRF	Weather and Research Forecasting
YSU	Yonsei University Scheme

List of Mathematical Symbols

Latin Symbols

C	Speed of Sound
c	Land Surface Heat Capacity
c_p	Specific Heat of Air at Constant Pressure
c_v	Specific Heat of Air at Constant Volume
F	Force
g	Gravitational Acceleration (9.81 m s^{-2})
H	Height
k	Turbulent Kinetic Energy
L	Length
M	Soil Moisture Availability
p	Static Pressure
P_0	Reference Pressure, 10^5 Pa
R_d	Gas Constant for Dry Air
Re	Reynolds Number
t	Time
T	Matrix of Rotation
V	Velocity

X	Inertial Coordinate
x''	Local Coordinate
Y	Inertial Coordinate
y''	Local Coordinate
Z	Inertial Coordinate
z''	Local Coordinate

Greek Symbols

α	Albedo
γ	Ratio of Specific Heats
∇	Differential Operator
ϵ	Surface Emissivity
η	Non-dimensional Number Representing the Vertical Grid Level at AWRP ARW (0-1)
θ	Euler Angle, Rotation Around Y Axis, Potential Temperature
λ_t	Thermal Inertia
μ	Dynamic Viscosity, Mass Per Unit Area
ρ	Density
σ_{SB}	Stephen-Boltzmann Constant
ϕ	Euler Angle, Rotation Around X Axis
Φ	Geopotential
ψ	Euler Angle, Rotation Around Z Axiswith aim
ω	Rotation Rate
Ω	Contravariant of the Vertical Velocity

Chapter 1

Introduction

1.1 The Broad View

The importance of maintaining the global temperature increase to less than 1.5°C by the end of this century relies upon reducing the production of anthropogenic Green House Gases (GHG) [46]. A large portion of the global anthropogenic GHG productions result from open-pit mining [46].

The common methodology for evaluating the emissions of GHG from open-pit mines is based on inventory guidelines in which the emissions from different stationary sources across a mining facility are combined. This is also known as the bottom-up approach. The major drawback of using the bottom-up approach is the fact that it does not incorporate atmospheric measurements and relies on assumptions of the strength of each GHG source within a facility that may not be up-to-date [46].

The top-down approach, however, makes use of an aircraft to directly measure the atmospheric meteorological conditions and mixing ratios of GHGs. The plane flies around a virtual box over the facility at multiple altitudes[46]. The flight paths are then plotted on a two-dimensional vertical screen boxing the facility. The total flux of GHG through this screen is calculated by considering the aircraft wind measurements and the mixing ratio of GHGs using the divergence theorem [29]. The downside of this methodology is limitations of flying around a facility. This includes the challenge of flying at low altitudes, flying at night, and the cost of flying.

To evaluate the emission of GHGs from a large scale open-pit mining facility without the limitations of bottom-up or top-town approaches, while considering the atmospheric conditions, requires novel approaches. The new methodologies incorporate high resolution

numerical modelling to forecast the fluxes of GHG as a function of time and space. To set up a high resolution numerical model, the vertical profiles of atmospheric variables including wind speed, temperature, and pressure are required as boundary and initial conditions. It is also required to have surface temperature and mixing ratios of GHGs as they vary both spatially and temporally. The accuracy of the model's predictions then rely upon the accuracy of the initial and boundary condition data. The more accurate this data, the more accurate and realistic the forecasts of GHG fluxes.

1.2 How Does This Thesis Fit into the Overall Picture?

This thesis develops and contributes to two distinct methodologies to acquire accurate profiles of atmospheric variables in support of high resolution numerical modelling of GHG transport. The first approach developed a novel airborne sensing instrument called the Tethered And Navigated Air Blimp (TANAB) to directly measure the vertical profiles of atmospheric variables. The instrument then operated across an open-pit mining facility and the records were post processed. The second approach updated the data structure of a mesoscale weather model, the Weather Research and Forecasting (WRF), with the latest land development in the facility. The model predictions were then compared against the ground based measurements and air soundings. Figure 1.1 shows the flow chart of the new approaches to calculate the emission fluxes of GHG from an open-pit mining facility.

1.3 Review of Meteorological Sensing Technologies

The Atmospheric Boundary Layer (ABL) is defined as the first layer of the air near the earth surface that responds to the surface processes on time scales of one hour or less [7, 68]. The three-dimensional structure of the ABL is the key for the understanding of surface-atmosphere exchange processes [68]. The phenomena occurring in the ABL, which are governed by turbulent transport and mixing, are of high importance in air quality, weather, and climate dynamics [35].

Meteorological measurements of temperature, pressure, humidity, wind velocity vector, and fluxes of heat, momentum, and atmospheric constituents are crucial in understanding the transport mechanisms of momentum, energy, and pollutants in the ABL [34]. The existing meteorological knowledge about ABL are available from in-situ records such as those measured by meteorological masts, ground-based, or remote sensing platforms. In-situ mea-

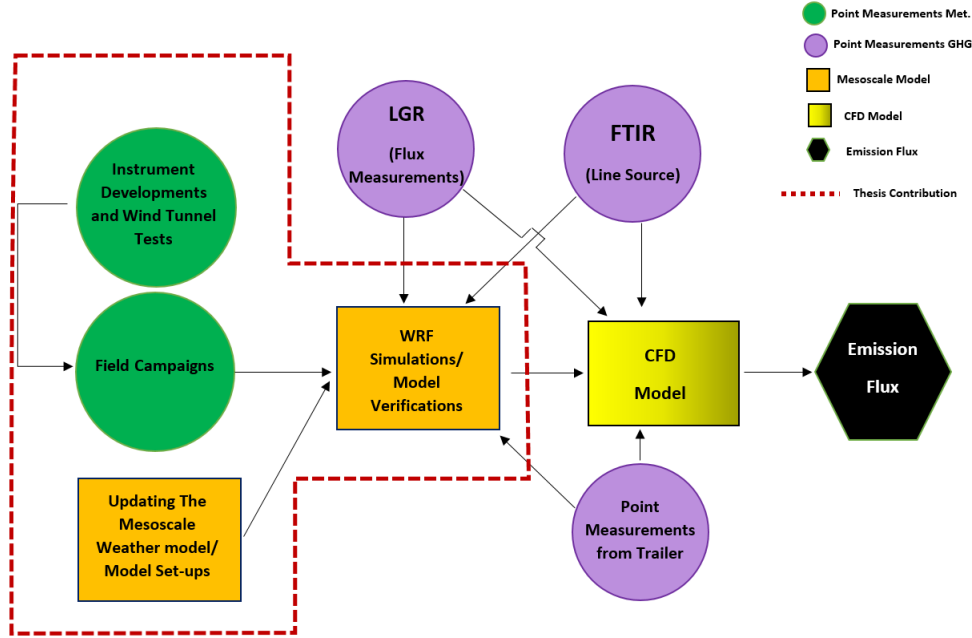


Figure 1.1: The flow chart of the new methodologies to determine the GHG emission fluxes from an open-pit mining facility. This thesis contribution's to the overall methodology is outlined.

measurements are performed by numerous instruments such as anemometers, thermometers, while remote sensing measurements are performed by SOnic Detection And Ranging (SODAR), Light Detection And Ranging (LiDAR), RAdio Detection and Ranging (RADAR), satellites, or other technologies.

The major drawback of meteorological masts is the lack of positioning flexibility and a limited range for altitudes of observation. Logistical challenges put limits on mast locations. For example, if a mast is not erected within a flat terrain, complex topographical slopes complicate flow field and flux measurements. Wilczak et al. [76] showed that for an unstable condition over sloped terrain, a one degree tilt in the anemometer results in 64 % fractional error estimation of vertical component of Reynolds stress.

Ultrasonic anemometry for atmospheric studies have been available since the early 1970s. The cost of maintenance is very low because the sensor is made up of solid state and non-moving parts. The response time and starting threshold for both wind speed and direction are negligible. These two characteristics make the ultrasonic anemometer a good candidate for air pollution dispersion and other applications requiring high accuracy at very low wind speeds [70]. For atmospheric studies the frequency of measurements is usually between 10

and 40 Hz [7, 8]. The atmospheric measurements at high frequency rates are able to detect the finer time and length scales of turbulence. The results of numerous field campaign studies [24, 42] point out the preference for 10 Hz sampling rate.

Sonic Detection And Ranging (SODAR) technique uses the Doppler effect with a multi beam configuration to determine the wind speed and direction. A SODAR consists of antennas that transmit and receive acoustic signals. A SODAR maps the profile of atmospheric variables such as wind speed, wind direction, vertical wind speed, and turbulence kinetic energy. The vertical measurement range can reach up to 3 km, which is the function of the frequency, power output, atmospheric stability, and turbulence. The noises in the environment highly affect the performance of a SODAR. The frequency of measurements, however, is low as it takes a relatively long time for the acoustic signal to reach the top level of the range and echo back, hence, fine scales of turbulence are not possible to measure by a SODAR [7].

Light Detection And Ranging (LiDAR) technique transmits laser pulses into the atmosphere, where light scattering occurs by aerosol particles, ice crystal, water vapor, or trace gases such as ozone. The returning scattered beams that reach the receiver exhibit a time delay that is related to the distance of the measurement location to the ground. LiDARs reveal cloud distance or the pollution concentration. The frequency shift of the returning signal can be used to calculate the wind speed [1].

Radio Detection and Ranging (RADAR) instruments have been mostly effective for measuring precipitation by means of transmitting signals that contain information about atmospheric aerosols. RADARs can cover an area about 400 km around a site of interest. Post processing the RADAR measurements reveals the horizontal view of the atmosphere at each elevation angle as well as the vertical contours of the atmospheric aerosols at each direction. Severe weather conditions could be detected by analyzing the shape, size, and strength of a RADAR return signal. For instance, the height of the vertical slices shows the strength of a weather storm [2].

Despite the recent technological advancements in remote sensing, the high temporal and spatial resolution measurements of the atmospheric winds still benefit from in-situ measurements. An onboard fast recording sensor that could freely traverse in the atmosphere would be an ideal instrument to measure the turbulence characteristics of ABL [28].

In order to help determine properties of ABL in more detail, measurement techniques capable of providing the detailed vertical profiles of temperature, moisture, and winds within the atmospheric boundary layer (ABL) are needed. Acquiring the vertical profile of at-

atmospheric parameters is possible by remote sensing satellites or in-situ probes installed on aircraft, balloons, and Unmanned Aerial Vehicles (UAVs) [39].

Aircraft measurements expand the spatial and temporal coverage of the atmospheric properties because they travel great distances. The high speed of the platform enables the instruments to measure a significant number of eddies in a short time period. The measurements later need to be corrected to convert the plane records from a moving reference frame into a fixed reference frame. The conversion takes into account the aircraft's velocity components and angular orientations (roll, pitch, yaw) [10, 12]. Typically, wind velocity vector measurements onboard of an aircraft are performed by incorporating a five-hole Pitot tube installed in front of the plane (to avoid the flow distortion caused by the plane itself). Using the five-hole pitot tubes, the full wind vector could be determined [11]. The major drawbacks of using aircraft in ABL studies include 1) operating cost, 2) inability to detect the lower altitudes due to the flight regulations, and 3) limitations due to the weather conditions and night time flights.

UAVs, such as fixed-wing or rotor-wing drones, are powered aircraft that can fly without the need of an onboard human operator. Previously, UAV applications were specific to military operations, but, recently they have found applications in other fields [20]. Also, a drone could be equipped with radioactive, chemical, magnetic, imagery, or biological sensors in rescue emissions, agriculture, petroleum, mineral exploration, mapping, ecological, environmental, and meteorological studies [36, 37, 64].

Unmanned Aircraft Systems (UASs) are defined as either a fixed-wing or rotor-wing platform that weighs fewer than 25 kg and their environmental sensing applications date back to 1970s to measure temperature, humidity, pressure, and wind velocity up to 3048 m in altitude [34]. Recently, Small Unit Unmanned Aerial Vehicles (SUAVs) have been used in Antarctica to study the temperature profiles of ABL and the evolution of ABL structure during the flying season [17]. In another study, SUAVs were used to evaluate the ABL parameterization schemes embedded in the Advanced Weather Research and Forecasting (AR-WRF) model [50]. The measurements enabled profiling of temperature and relative humidity up to 3 km representing stable and convective ABLs.

UAVs, provide a dynamic platform for atmospheric studies. Hemingway et al. [34] deployed UAVs with vertical resolutions of approximately 3 m and 1.5-2 m for temperature and relative humidity measurements, respectively. The main drawbacks of using UAVs in atmospheric studies are the battery's short life and the air distortion produced by their motors or engines. UAVs are deployed in a wide range of meteorological research applications.

Using either hot air or a light gas (such as helium) balloons have been used in studying atmospheric turbulence. There are two kinds of approaches in utilizing the balloons, 1) tethered balloon that can be reused and navigated once launched, and 2) radiosondes which will not be returned once launched. The balloons could be equipped with multiple sensors to record the ABL structure once ascending in the atmosphere [72].

A “Radiosonde”, as defined by the official American Meteorological Society (AMS) glossary, is an expendable meteorological instrument package, often borne aloft by a free-flight balloon, that measures, from the surface to the stratosphere, the vertical profiles of atmospheric variables and transmits the data via radio to a ground receiving system [3]. Vilho Vaisala and Pavel Molchanov both independently invented and developed the radiosonde (rawinsonde) in the late 1920s in Finland and the Soviet Union. Radiosondes expand the understanding of profiles of the atmospheric variables above the earth surface all the way up to troposphere and stratosphere [52]. Over 900 stations all over the world contribute to the radiosonde network by launching the weather balloons two times a day at 00Z and 12Z. That way the records are concurrent and consistent for each station across the globe. Sometimes intermediate launches at 06Z, 18Z occur to record the high impact weather situations, such as severe weather outbreak or a land falling tropical cyclone.

Tethered balloons could be used to record the atmospheric properties for hours without distorting the surrounding air as much as motored or engined UAVs. Also, regulations are less restrictive on tethered balloons as opposed to other airborne sensing instruments. Furthermore, the cost of design and operation for balloons is significantly less than that of aircraft.

Tethered balloon based atmospheric measurement techniques have been used widely for obtaining the turbulence structure as well as the mean vertical profiles of the ABL [75]. One of the main advantages of tethered balloon system is its ability to probe a significant portion of the planetary boundary layer, especially the surface layer, which is not possible or economical by ground-based or aircraft-based atmospheric measurement techniques [23].

Studies have shown that tethered balloon based probes could be used for continuous measurement of the important parameters in the ABL without disturbing the flow compared to a stationary tower-mounted instruments, which perturb the flow measurement by the structure of the tower [31]. The tethered balloon system does not have the limitations of surface-based atmospheric turbulence measurements such as the influence of local topography, nearby structures, and buildings on the wind [65].

Tethered balloon-borne atmospheric turbulence instrumentation have been used for a num-

ber of years over the land [63] and sea [74] to measure fluxes of heat and moisture at heights up to a few hundred meters. The most notable tethered balloon system-based data collection campaigns in the late 1960s and 1970s include Barbados Oceanographic and Meteorological Experiment (BOMEX) [21, 26, 27], the Joint Air-Sea Interaction (JASIN) Experiment [59] and The Global Atmospheric Research Program (GARP) Atlantic Tropical Experiment (GATE) [13]. In BOMEX a tethered balloon system was operated from the deck which measured temperature, wind, and humidity, continuously, at different levels in the range of 0 to 600 m in the ocean area north and east of the Island of Barbados. In JASIN tethered balloons were used to measure the structure of ABL to understand the air-sea interaction in the North Atlantic.

In the recent past tethered balloon systems have been used in Boundary-Layer Late Afternoon and Sunset Turbulence (BLLAST) field campaign that was conducted in southern France [48]. [16] used an ultrasonic anemometer mounted on a tethered balloon system for turbulent flux and variance measurement. [23] used the BELUGA (Balloon-borne modular Utility for profiling the lower Atmosphere) tethered balloon system for turbulence and radiation measurements in the Arctic.

1.4 Review of Numerical Weather Prediction (NWP) Modelling

A Numerical Weather Prediction (NWP) model is a computer code that uses one particular set of dynamical equations, numerical approximations, and physical parameterizations to predict weather phenomena. The different weather models have different dynamics, numerics, and physics parameterizations. Some examples include the Weather Research and Forecasting (WRF) model, the Global Environmental Multi-scale (GEM) model, or the Global Forecast System (GFS) [69].

The idea of NWP was first published by Vilhelm Bjerknes in 1904, in which he proposed to predict the atmospheric evolution in a future time using transport equations developed a decade earlier by Navier and Stokes. Two decades later, Lewis Fry Richardson used a mechanical desk calculator to solve the primitive equations accounting for six hours of surface pressure in the future. The calculations continued for six weeks and the final results were off by one order of magnitude compared to the observations [60].

In 1945, John von Neumann and Vladimir Zworykin at Princeton University's Institute

for Advanced Studies started the first attempt to use the electronic computers to initiate the NWP models. Shortly, they realized in order to meet the limits of their computing power, they have to simplify the equations of fluid motion to a simple barotropic model that only accounts for the conservation of vorticity. The first forecast was made in March-April 1950 addressing three case studies over North America [69].

Mesoscale NWP atmospheric models are largely limited by their grid resolutions. For instance, European Center for Medium-Range Weather Forecasting (ECWMF) incorporates a 40-km horizontal grid resolution for its global model, while GFS uses a 35-70-km horizontal grid resolution for its global model [67]. Even regional scale models, such as the regional GEM model, are run on a horizontal grid resolution in the order of 10 km [9]. The horizontal grid resolutions greater than a kilometre cannot observe the microscale spatial changes of meteorological variables, hence, microscale atmospheric simulations are limited in operational modelling. At the same time, such microscale meteorological effects should be incorporated to predict the near-surface flow and surface fluxes for various applications with complex topography, land use, and non-homogeneous conditions [73].

In order to execute a high horizontal resolution simulation, a nested atmospheric simulation is necessary. The largest domain of the nested simulation is driven by reanalysis or forecast data fields from a global or regional operational simulation, while the smaller domains resolving the microscale features are simulated offline from the operational model. This approach can combine the strengths of the different models at different scales [73].

The Weather Research and Forecasting (WRF) model is developed as a next-generation NWP and atmospheric simulation system to place new and existing research and operational models under a common software architecture. WRF made it possible to combine and match the dynamical cores and physics packages of various models to optimize performance, and this feature is particularly advantageous for intermodal comparisons and sensitivity studies [53].

WRF offers the multi-scale nesting simulation approach. The nesting technique in mesoscale simulation helps alleviating the model efficiency in predicting 1) the dynamics of convection and convective clouds and rainfall in ABL, 2) the influence of urban buildt-up areas on the microclimate and thunderstorm dynamics over built terrain [56], 3) the impact of sudden changes in local land use on atmospheric flows and land atmosphere interactions, 4) and their impact on the pollutant transport [14, 73].

WRF is designed for both atmospheric research and operational forecasting applications. The model can be applied over a wide spectrum of spatial scales, from tens of meters to thou-

sands of kilometres. The WRF development began in the late 1990s and was a collaborative partnership of the National Center for Atmospheric Research (NCAR), the National Oceanic and Atmospheric Administration (represented by the National Centers for Environmental Prediction (NCEP) and the (then) Forecast Systems Laboratory (FSL)), the (then) Air Force Weather Agency (AFWA), the Naval Research Laboratory, the University of Oklahoma, and the Federal Aviation Administration (FAA) [5].

Static and dynamic information of the domain of interest including land surface, surface layer, and Planetary Boundary Layer (PBL) are essential to initialize the model and calculate the exchange of heat, moisture, and momentum between the surface and atmosphere.

The choice of land use classification in atmospheric models is of high importance as it determines the exchanges of heat, moisture, and momentum between the surface and the air that in return impacts the temperature, humidity, and wind near the surface. Also, the topography is important when conducting the simulation over a complex terrain [41].

The land use specifies the information about the region of the interest. For instance, land use separates built-up, forest, wetland, cropland, and water classifications. This classification affects the thermodynamic and aerodynamic parameters of the land such as albedo α , surface emissivity ϵ , roughness length scale z_0 , land surface heat capacity c , thermal inertia λ_t , and soil moisture availability M , which can further affect the prediction of the meteorological variables [25]. Several studies have shown the importance of land use classification in meteorological simulations. For example, the effects of modifying land use classification on wind speed, wind direction, temperature, heat flux, and relative humidity predictions have been reported [19, 51, 53, 58, 61].

In one study, WRF predictions were compared against the ground based measurements and it was found that the model predicts the wind direction with less error over the flat terrain. The accuracy decreases in low-velocity flows [40]. Improvement in model's predictions of temperature and precipitation was achieved by modifications in surface elevation, land use index, vegetation fraction, and soil type datasets [32]. Many studies have suggested that incorporating high-resolution topography and land use datasets increase the accuracy of the forecasts [43].

The topographic properties affect the regional circulation and change the predictions of precipitation, wind speed, and heat-related properties [38, 77]. It was found that reducing the topographic resolution changed the WRF predictions of precipitation significantly and the model underestimated the predictions [55]. The updated land use change has improved the predictions of wind fields and precipitation [18, 18, 44, 45].

The resolution of the computational grid is important when performing a simulation over a complex terrain. The grid spacing should be fine enough to capture the steep slopes, so that the model can predict the actual surface parameters such as temperature, humidity, wind speed, and wind direction. The default topography included in WRF is the GEOTOPO dataset with the horizontal resolution of 30'' which is approximately 1 km on the surface of earth. Refining the horizontal grid spacing while using this database will not provide the necessary accuracy for microscale predictions. An alternative high horizontal resolution terrain dataset is the Shuttle Radar Topography Mission (SRTM) with the horizontal resolution of 1'' which is approximately 30 m. SRTM is available for most of the earth surface in the northern hemisphere. Another alternative approach is use of custom LiDAR data collected over a complex terrain, which can be ingested into WRF manually. Incorporation of high resolution terrain data has made it possible to downscale the grid spacing of WRF in the horizontal direction down to below hundred meters for microscale meteorological investigations [53].

1.5 Objectives

In support of high resolution numerical modelling of atmospheric transport over open-pit mining facilities, this thesis develops and executes two approaches to understand ABLs over open-pit mining facilities better. In the first approach a novel airborne sensing instrument, titled the Tethered And Navigated Air Blimp (TANAB), capable of measuring vertical profiles of atmospheric boundary layer variables, such as temperature, wind velocity components, pressure, and relative humidity, is designed, tested, and calibrated in a wind tunnel. The instrument is then successfully operated in an environmental field campaign measuring meteorological dynamics over a mining facility in May 2018. The records are then transformed to provide vertical profiles of atmospheric parameters.

In the second approach, a numerical weather prediction system, Weather and Research Forecasting (WRF) model, is adapted with topographical and land use changes over the mining facility to simulate meteorological dynamics over the mining facility more realistically. The model predictions are compared against the ground based measurements and the air soundings. The adaptation of the WRF model for this application is novel and has resulted in better numerical predictions of meteorological dynamics over the mining facility in agreement with field observations.

1.6 Mining Project, Area Fugitive Emission Measurements and Collaboration Details

The work documented in this thesis is one part of a very large multi-institution research project that attempts to quantify the amount of area fugitive emissions from an open-pit mining facility in northern Canada. The specific information about the project, such as the type of mine, location, and client information, cannot be disclosed due to non-disclosure agreement with the client. However, the generic information is provided to help advance research in the field of area fugitive emissions. The large research project also employs numerous graduate students and research staff members at the University of Guelph, the specific roles of whom are detailed below.

The Tethered And Navigated Air Blimp (TANAB) is one of the experimental platforms used in this project to measure atmospheric profiles of meteorological variables. TANAB is a collaboration between two undergraduate fourth year design teams (Team 1: Reed Stock, Denis Clement, and Jason Dorssers, and Team 2: Darian Vyriotes, Amanda Pinto, Katharine McNair, and Phillip Labarge) and two M.A.Sc. students (Amir Nazem and Ryan Byerlay) at the University of Guelph. The undergraduate design teams developed the gondola and integrated a thermal camera for earth surface temperature mapping. The author exclusively integrated the TriSonicaTM Mini weather station into the system and provided the calibration factors through a series of wind tunnel tests. Ryan Byerlay has developed the methodology for earth surface temperature mapping.

TANAB was operated in the open-pit mining facility in May 2018 by Amir Nazem, Rafsan Nahian, Ryan Byerlay, Manoj K. Nambiar, and Amir A. Aliabadi. The deployments were planned to cover the full diurnal cycle as well as different locations in the mining facility. The recorded data were then post processed by Amir Nazem with the help of Manoj K. Nambiar and Amir A. Aliabadi. The results include profiles of atmospheric meteorological variables such as wind velocity vectors, potential temperature, and turbulence statistics.

In the modelling approach, the author exclusively updated the Weather Research and Forecasting (WRF) software with the latest topography, land use classification, and lakes at the mining facility. The author completed WRF simulations for three days in May, 2018. The simulation periods were planned to be concurrent with the field measurements. The author exclusively developed the model modification and the setup of initialization methodology. The author compared the model's predictions against the air soundings and analyzed the effects of the land classification modifications on some selected static parameters including

surface albedo, surface emissivity, and aerodynamic roughness length scale.

Another M.A.Sc. student, Rafsan Nahian, conducted a series of sensitivity analyses in WRF to quantitatively investigate the model's performance with respect to: 1) grid resolutions, 2) land classification modifications, 3) Planetary Boundary Layer (PBL) physics, 4) initialization datasets, and 5) seasonal comparisons. Rafsan Nahian also rigorously compared WRF output results with field observations of meteorological variables.

Rafsan Nahian and Amir A. Aliabadi developed a series of Python programs to post process and interpret the WRF model's output results and compared them with experimental observations statistically. In a parallel effort, Ph.D. student Seyedahmad Kia is developing a Computational Fluid Dynamics (CFD) code to simulate the area fugitive emissions dispersion and flux over the mining facility. He acquires the initial and boundary conditions from WRF predictions and runs the simulations, using the Open Fields Operation And Manipulation (FOAM) software, at higher spatial and temporal resolutions at different atmospheric stability conditions.

1.7 Thesis Structure

Chapter 2 features a new airborne sensing platform for meteorological measurements in the surface layer of ABL. A procedure to calibrate the instrument in a wind tunnel is also discussed. Chapter 3 presents the numerical weather model (WRF) and the steps to update the model with the latest land use classifications and topography changes of the mining facility. Chapter 4 first presents the results of the airborne sensor platform development, calibration, and field observations. This chapter then presents the results of the numerical mesoscale model. Chapter 5 summarizes and concludes the study followed by providing recommendations for future work.

1.8 Summary

In this chapter, the experimental methodologies in ABL studies including: ultrasonic anemometry, SODAR, LiDAR, RADAR, and airborne sensing were presented followed up by the strengths and shortcomings of each approach. Development of a novel airborne in-situ technique in ABL research studies is advantageous to overcome the existing shortcomings and to better understand the structure of ABL above a complex topography. In this chapter, also a general overview of numerical weather models were introduced followed up by the

introduction of a new generation of Numerical Weather Prediction (NWP) models known as Weather Research and Forecasting (WRF) model capable of forecasting the meteorology across multiple scales from microscale to mesoscale. The model's performance in predicting the meteorology over complex terrains and the importance of the choice of the land use classification on the model's predictions are discussed based on previous studies.

Chapter 2

Meteorological Measurements from a Tethered and Navigated Air Blimp (TANAB) System

A technique has been developed for meteorological measurements of the surface layer within the ABL using a Tethered And Navigated Air Blimp (TANAB) system. TANAB is the third generation of the air monitoring balloon designs at the University of Guelph. TANAB is a collaboration between multiple undergraduate fourth year design teams and graduate students at the University of Guelph.

The first generation of TANAB was developed by undergraduate students Jacob Ludlow, Cole Merrill, Sean Ratcliffe, and Galen Woods in 2017. The first generation TANAB was capable of accurately measuring and recording environmental data for analysis and air quality characterization of the indoor environment. It was capable of sensing temperature, humidity, carbon dioxide concentration, and three-dimensional location indoors [49].

The third generation of TANAB is designed to measure wind velocity vector components, temperature, relative humidity, pressure, and three-dimensional translational and rotational position at high frequency. Exclusive to the third generation of TANAB is the capability to take thermal images of the earth surface through the use of an onboard thermal camera which is used to create thermal maps of a given site [66].

The TANAB system was launched at the mining facility in northern Canada in May 2018. The system measured meteorological conditions including the wind velocity vector components, temperature, relative humidity, and pressure up to 200 m above ground at a sampling frequency of 10 Hz. TANAB measured the dynamics of the atmosphere at different

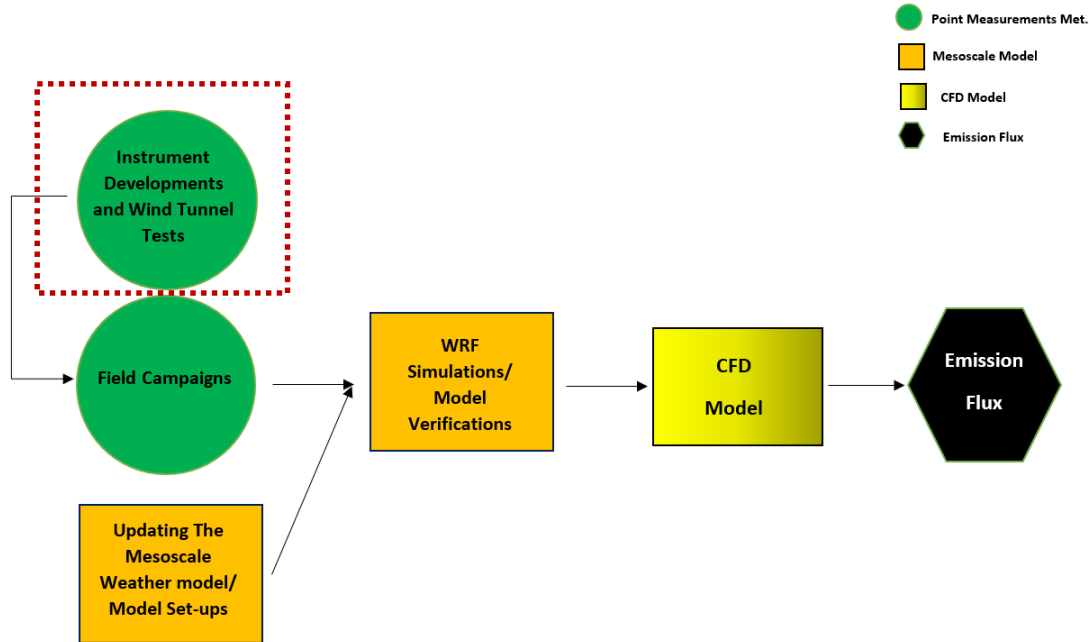


Figure 2.1: The instrument development outlined in the overall project.

diurnal times (e.g. day versus night) and various locations (near a tailings pond and inside an open-pit mine). Such dynamics include mean and turbulence statistics pertaining to flow momentum and energy, and they are crucial in the understanding of emissions fluxes from the facility in other studies. This chapter first briefly presents the TANAB’s specifications. It then presents the procedure to calibrate the TriSonicaTM Mini weather station. Figure 2.1 helps better demonstrate the contribution of the following chapter in the overall project.

2.1 Tethered and Navigated Air Blimp (TANAB) Specification

TANAB consists of fixed and variable payloads. The fixed payload is comprised of a helium balloon, the navigation tether, a tether reel, and a gondola platform housing the sensors. The variable payload is comprised of microclimate sensors, such as a mini weather station (TriSonicaTM Mini), a thermal camera, and a flight controller. While the fixed payload is the same for every mission, the variable payload can be altered to use different sensors suitable for a particular application. Figure 2.2 shows the TANAB system during field sampling and a detailed schematic of the gondola assembly with all the sensors onboard.

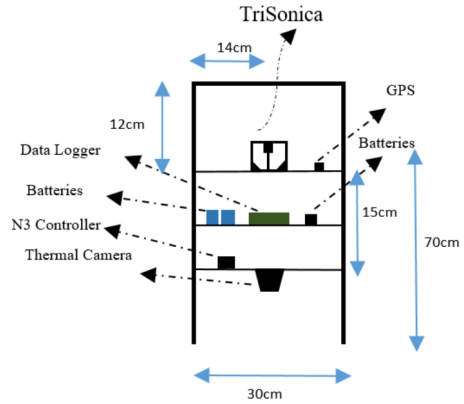


Figure 2.2: Left: TANAB system in operation, right: schematic of gondola assembly with all the sensors onboard.

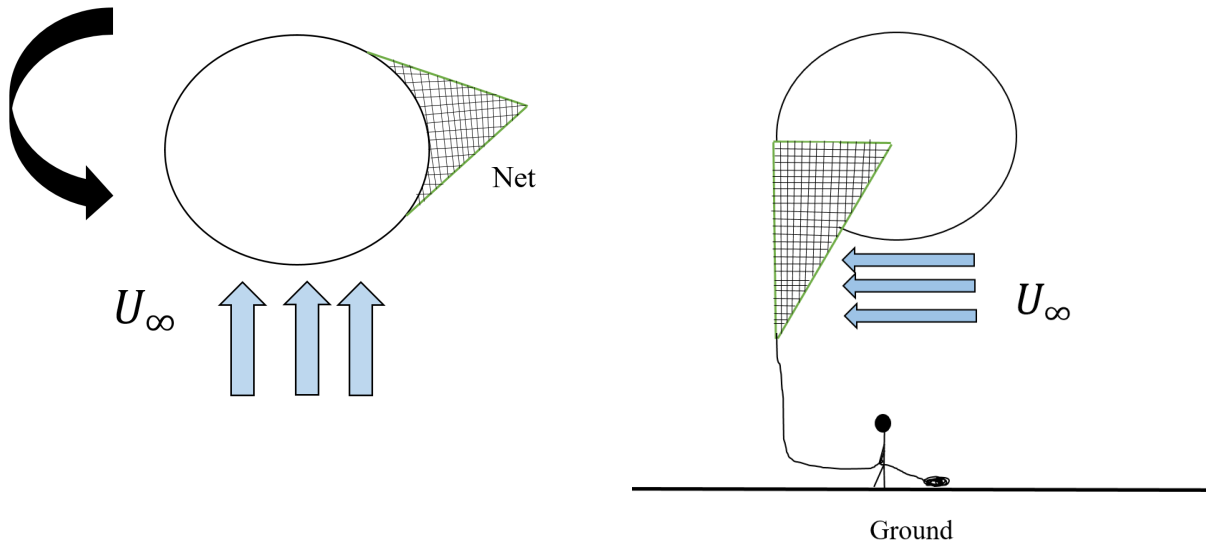
2.2 Gondola Motion

The gondola is a part of the tethered balloon system controlled by multiple ropes on the ground. The acting forces on the system are 1) the lift force due to the helium-filled balloon, 2) the force of gravity, 3) the tension forces due to the ropes, and 4) the drag forces due to the wind. In the absence of the drag force the remaining forces are acting in the vertical direction and the system ascends up and down, but, the presence of the drag force displaces the system in the horizontal direction. At all times these forces are balanced so that the TANAB is in a quasi-stationary position.

The balloon is equipped with a net that helps facing the balloon toward the main wind direction at any moment. The net guides the air on one side, and the pressure force stops the balloon from rotating. In case of wind direction changing, the pressure force builds up on the net creating a torque around the centre of rotation that repositions the balloon facing the main wind.

Figure 2.3 schematically shows the net's yaw correction when the main wind direction changes. Up to three ropes are used to tether the balloon to help stabilizing the system, especially during high winds associated with convective boundary layers. The ropes, however, impose extra weight on the system so that the vertical range of the system reduces when three ropes are used as opposed to one.

The evidence that the net mechanism succeeds in aligning the balloon against the main wind direction can be found in Fig. 2.4. The wind-rose shows the wind direction records by TriSonica™ Mini (at TriSonica™ Mini's coordinate) for over 56 hours of flight. According



(a) Top view of the balloon and the net.

(b) Side view of the balloon and the net.

Figure 2.3: Positioning of the balloon against the dominant wind direction.

to the wind-rose the gondola mostly faces against the main wind direction because wind direction is recoded from the local north direction most of the time. Note that TriSonicaTM Mini's north axis is the sensor local coordinate. If desired, this reading can be converted into the fixed inertial body of reference. For this to occur, the sensor yaw, pitch, and roll angles need to be used.

Figure 2.5 shows the balloon operation in an unstable atmosphere with high winds when three ropes are used to stabilize it. A sudden drag force on the gondola may drive the system out of its stable position momentarily. Hence it may affect the quality of measurements by creating instabilities. Such phenomenon can be prevented by deploying extra ropes connecting the gondola directly to ground operators. The tension in these ropes cancels out the sudden drag force exerted on the system. This arrangement places the gondola in a quasi-stationary position in the air that indeed helps the stability of measurement in gusty conditions. Figure 2.6 shows the balloon operation in a stable atmosphere with low winds when only two ropes are used to stabilize it.

A T-connector connects the balloon to the gondola using ropes allowing the gondola to hang freely while minimizing the pitch and roll angles to result in better measurements. Figure 2.7 shows the distributions for pitch and roll angles recorded by TriSonicaTM Mini's compass over 56 flight hours. According to the bar charts the T-connector successfully maintained the horizontal stability of the sensor during the measurement. The gondola is

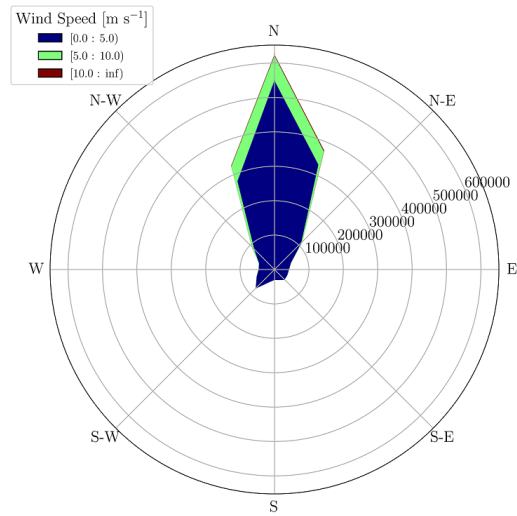


Figure 2.4: The wind-rose corresponding to 56 hours of flight, reported in the local coordinate system of the sensor. The numbers on the plot indicates the number records collected at 10 Hz.

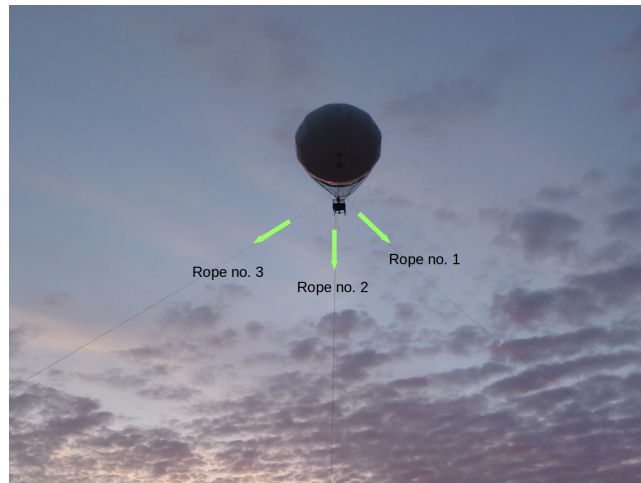


Figure 2.5: TANAB and three stabilizing ropes deployed at the mining facility. The system measures in the unstable atmospheric boundary layer.

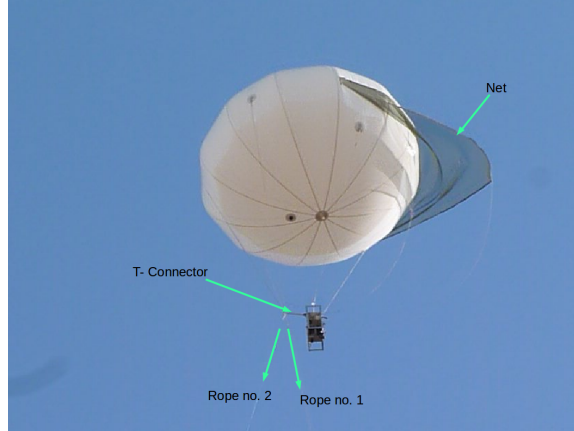


Figure 2.6: TANAB and two stabilizing ropes deployed at the mining facility. The system measures in the stable atmospheric boundary layer.

positioned 2 m below the balloon, so the effects of the balloon motion on the gondola are reduced.

2.3 Mini Weather Station

A conventional ultrasonic anemometer generates a small magnitude pressure disturbance in the fluid at the speed of sound relative to the fluid. The absolute velocity of pressure disturbance propagation would be the algebraic sum of the fluid velocity and the pressure-disturbance velocity within the fluid at rest. Knowing the velocity of the pressure disturbance, the fluid velocity could be calculated. This technique requires acoustic transmitters and receivers.

The TriSonicaTM Mini weather station is an ultrasonic anemometer manufactured by Anemoment¹ and is mounted onto the gondola of TANAB. This mini weather station is ideal for applications that require a miniature, lightweight, and low velocity anemometer, and is suitable particularly for airborne systems. It has a measurement path length of 35 mm and a weight of 50g. The light weight makes it an ideal candidate to be used with the TANAB system. It can measure the three-dimensional wind velocity vector, air temperature, relative humidity, and the barometric pressure at a sampling rate up to 10 Hz. The open path provides the least possible distortion of the wind field. Its design with four measurement pathways provides a redundant measurement and the path with the most distortion is

¹<https://www.anemoment.com/>

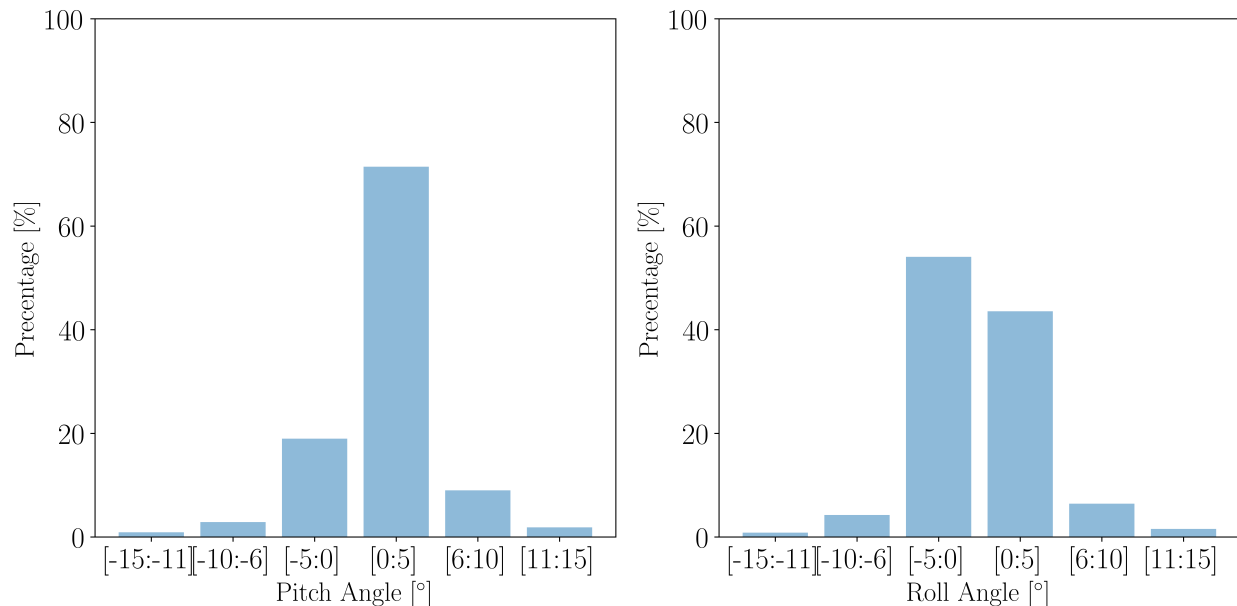


Figure 2.7: Left: the distribution of pitch angles recorded by TriSonicaTM Mini’s compass; right: the distribution of roll angles recorded by TriSonicaTM Mini’s compass.

removed from the calculations to provide accurate wind measurements. It is also equipped with a compass and a tilt sensor. Because of its low power consumption (only 30 mA at 12 V), it is highly power efficient and can record data for hours. Table 2.1 summarizes the TriSonicaTM Mini’s specifications.

Variable	Range	Resolution	Accuracy
Wind Speed	0 - 30 m s ⁻¹	0.1 m s ⁻¹	± 0.1 m s ⁻¹ at 0-15 m s ⁻¹ and ±2 m s ⁻¹ at 15-30 m s ⁻¹
Wind Direction	0-360°	1°	±1°
Temperature	-25°C to +80°C	0.1°C	±2°C
Pressure	50 - 115 kPa	0.01 kPa	±0.01 kPa

Table 2.1: TriSonicaTM Mini’s specifications summary [4].

The tilt sensor measures the pitch and roll with an accuracy of ±0.5°. The compass measures the magnetic heading with an accuracy of ±5°. The TriSonicaTM Mini is shown in Fig. 2.8.

TriSonicaTM Mini is made up of four facing transducer. Each pair of transducers are placed 35 mm apart. The two facing transmitters and receivers at the bottom point east-to-west that measure the east-to-west component of wind velocity, and the two on top point north-to-south that measure the north-to-south component of wind velocity. The other two



Figure 2.8: The TriSonicaTM Mini; figure extracted from [4]

ultrasonic pathways (transmitter on top and receiver at the bottom, and vice versa) plus the acoustic reflective surfaces built in the instrument, calculate the vertical component of wind velocity. The absolute air velocity along each ultrasonic pathway would be calculated by means of measuring the transmission time of an acoustic signal along that fixed path. The only limitation on the spatial averaging would be the frequency response time [15].

Figure 2.9 shows a schematic of a single-axis ultrasonic anemometer. The component of air velocity parallel to the ultrasonic path is V_d and normal to the path is V_n . Transmitter/receiver number one (TR_1) periodically receives and emits pressure pulses toward transmitter/receiver number two (TR_2) and vice versa. In the case when $V = 0$, the pulse would travel the ultrasonic pathway in time $t = d/C$ where d is the separation distance and C is the speed of the pressure wave in still air.

When there is a component of air velocity parallel to the path, the pulse traveling time is affected as the pulse is carried along by the airflow. For instance, if wind blows from TR_1 to TR_2 then the traveling time would be reduced as the apparent speed of the pulse will be $C + V_d$, while the apparent speed of the pulse from TR_2 to TR_1 would be $C - V_d$.

The wind's normal component has a minor effect on the travel time. It increases the apparent travel distance or decreases the speed of the pulse from C to $C \times \cos \alpha$, where $\alpha = \arcsin(V_n/C)$. As an example, when $V_n = 20 \text{ m s}^{-1}$ the apparent speed of the pulse would be dropped by 0.17%. Considering the effects of both parallel and normal components of air velocity, the travel times are

$$t_1 = \frac{d}{C \cos \alpha + V_d}, t_2 = \frac{d}{C \cos \alpha - V_d}. \quad (2.1)$$

Taking the difference between the inverse of transit time leads to

$$\frac{1}{t_1} + \frac{1}{t_2} = \frac{C \cos \alpha + V_d}{d} - \frac{C \cos \alpha - V_d}{d}. \quad (2.2)$$

Hence, the component of air velocity parallel to the path is determined as

$$V_d = \frac{d}{2(1/t_1 - 1/t_2)} \quad (2.3)$$

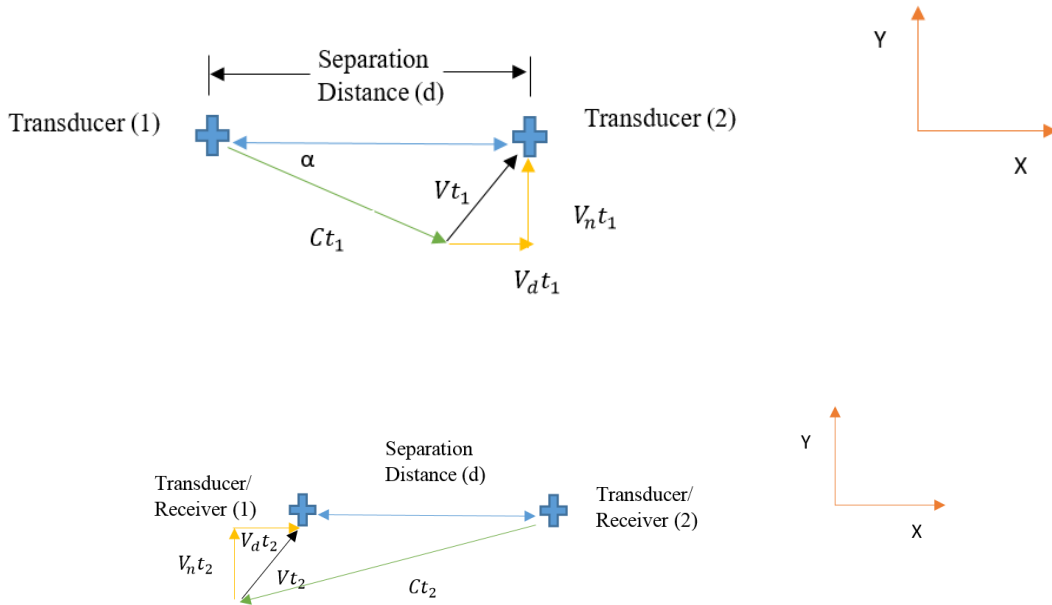


Figure 2.9: Ultrasonic anemometer vector relation; the anemometer measures the time required to transmit a signal to calculate the wind speed; top: transducer/receiver 1 sends the pulse; bottom: Transducer/receiver 2 sends the pulse.

2.4 TriSonica™ Mini Calibration

The objective of this section is to explain the methodology to characterize and calibrate wind velocity components measured by the TriSonica™ Mini. The objectives are achieved by comparing TriSonica™ Mini's measurements to measurements performed by the Setra model 264 low differential pressure transducer Pitot tube² and the R. M. YOUNG 81000

²www.setra.com

Instrument	Size [cm]	Weight [g]	Range	Resolution
TriSonica™ Mini	9.1×9.1×5.2	50	0-50 [m s ⁻¹]	0.1 [m s ⁻¹]
R. M. YOUNG 81000	10 height×10 di- ameter	1700	0-50 [m s ⁻¹]	0.01 [m s ⁻¹]
Setra Model 264 Low Differential Pressure Trans- ducer	14×7.6	280	-1 to +1 [IN WC (Inches of Water Column)]	± 0.25 [% FS (Full Span)]

Table 2.2: A summary of specifications for wind sensors used in the wind tunnel calibration experiment.

ultrasonic anemometer.³ Table 2.2 summarizes the important technical specifications of wind sensing instruments used. Series of experiments are designed and executed to characterize the performance of TriSonica™ Mini with respect to mean and turbulence statistics.

2.4.1 Wind Tunnel Test Summary

All the experiments were conducted in the University of Guelph’s wind tunnel. Figure 2.10 shows the wind tunnel, which is an open circuit tunnel designed for the turbulent boundary layer research. The cross sectional area is 1.2 m × 1.2 m. The tunnel is 10 m long. The tunnel’s air speed is controlled by a gage that sets the fan speed. The tunnel achieves wind speeds up to 10 m s⁻¹. The turbulence intensity is typically less than 2 % if no roughness blocks are placed upstream of the flow. The Reynolds number characterizes the turbulence level of the fluid flow and is defined as the ratio of the inertial to viscous forces given by $Re = \frac{\rho \times U \times L}{\mu}$, where U is the flow velocity, L is the characteristic length scale of the system (commonly, the hydraulic diameter of the wind tunnel), and μ and ρ are the dynamic viscosity and density of the fluid, respectively. Considering the characteristic lengths and wind speeds in the ABL, almost all boundary-layer atmospheric flows are turbulent. In the present study, wind tunnel’s Re number varies between 150,000 and 1,100,000. Considering the size of the wind tunnel, it is capable to generate eddies as large as its physical dimensions. Figure 2.11 shows the flowchart of the wind tunnel test.

The consistency and spatial distribution of wind levels across the test section were determined by plotting the contours of wind velocity at the test section. The Pitot tube was positioned at nine locations of the test section facing the wind. The measurements were repeated at each location for five minutes continuously at four wind levels. Imposing a no-

³www.youngusa.com

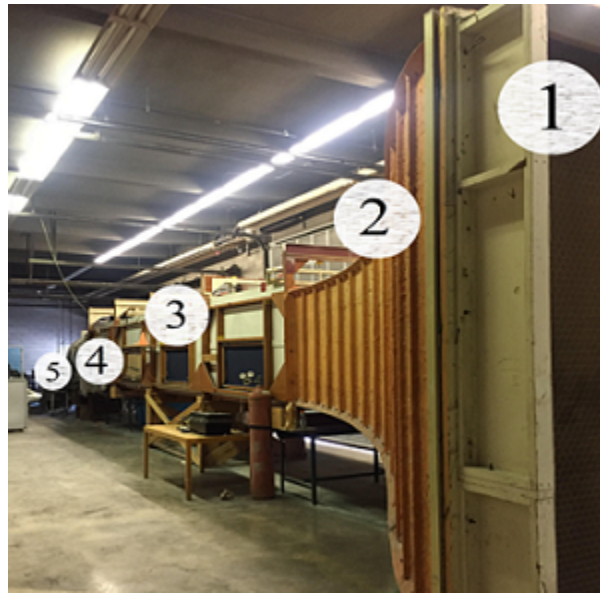


Figure 2.10: Wind tunnel at the University of Guelph: 1=honeycomb, 2=contraction, 3=test section, 4=diffuser, and 5=fan.

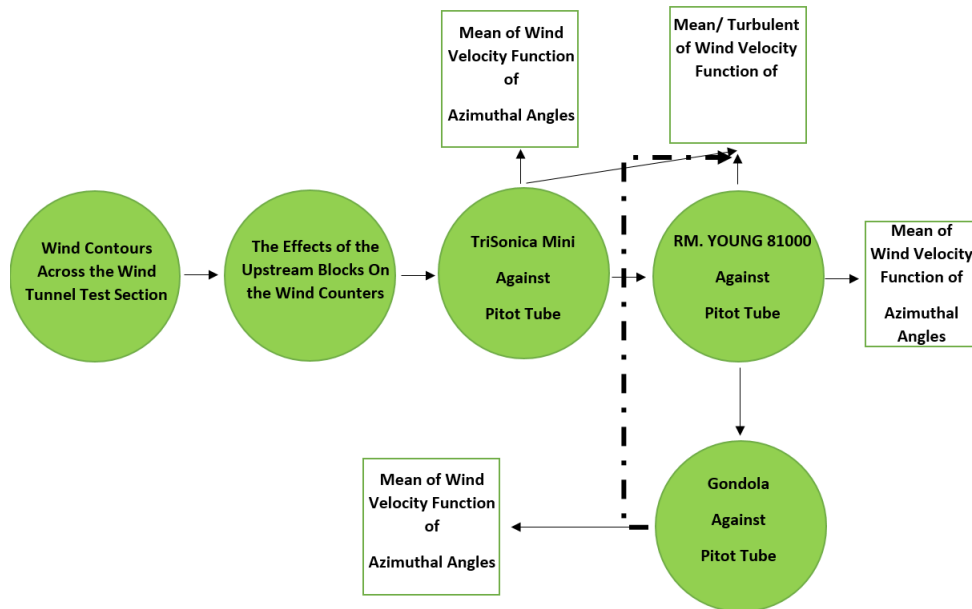


Figure 2.11: The flow chart representing the wind tunnel test.

Variable \ Wind Level	Wind Level N. 1	Wind Level N. 2	Wind Level N. 3	Wind Level N. 4
Variance [$\text{m}^2 \text{s}^{-2}$]	0.004	0.011	0.011	0.018
Turbulence Intensity [%]	0.109	0.211	0.155	0.199

Table 2.3: Change in variances and turbulence intensities as a function of the wind tunnel’s wind speed.

slip boundary condition at the tunnel walls and time averaging of the records at each test point, the contours of average wind speeds were calculated and analyzed at four wind levels. Figure 2.12 shows the contours of air velocity at four wind levels on the cross-sectional area of the test section.⁴ Figure 2.13 shows the time series of wind speed at each wind level. The variance of wind speed and the corresponding turbulence intensities are calculated in Table 2.3.

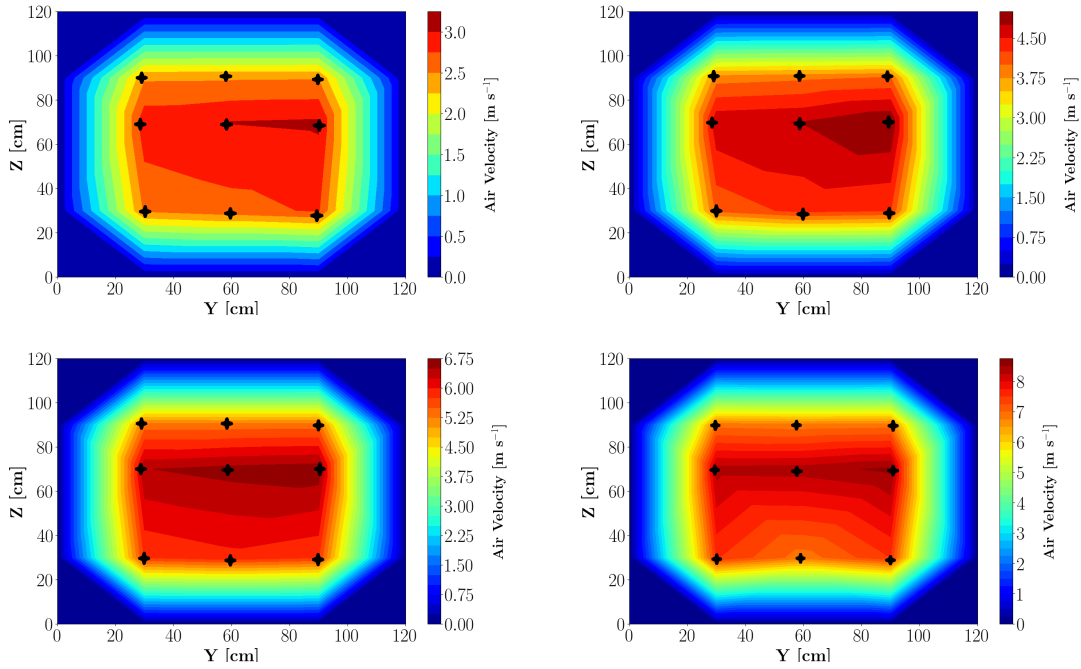


Figure 2.12: Contours of air velocity at four wind levels (2, 4, 6, and 8 m s^{-1}); the measurement locations are marked on the plots.

Pitot

⁴The number and distribution of the measuring points were limited by timing of this project, the height of the Pitot tube’s stand, and the importance of the flow field at middle of the tunnel

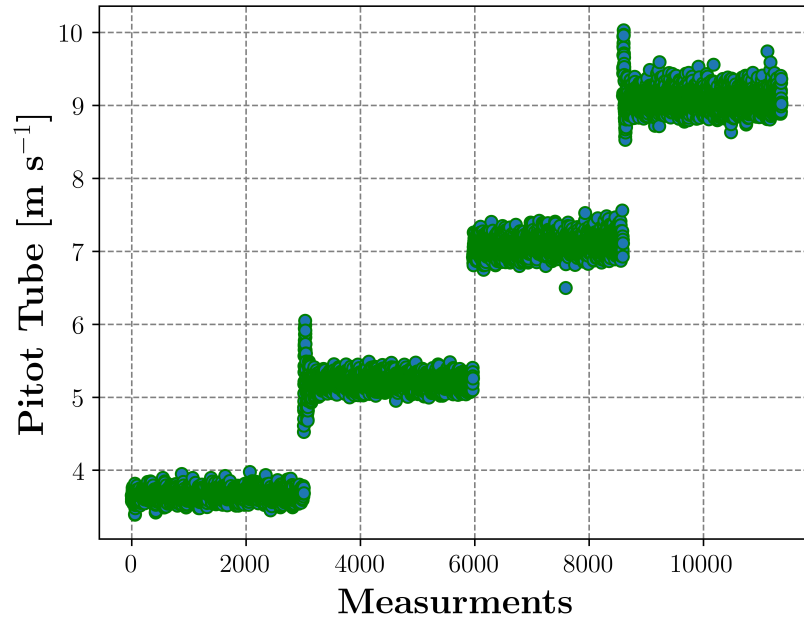


Figure 2.13: Variation in wind speed at each wind level.

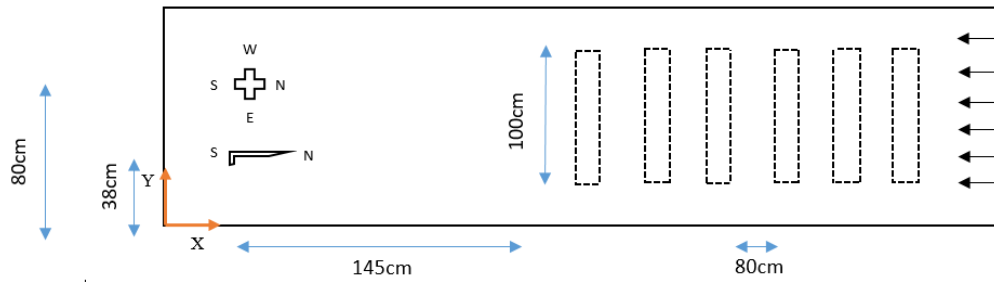


Figure 2.14: Schematic of the experimental setup at wind tunnel. On the right: arrays of same size blocks to introduce turbulence to the flow and on the left: the instrument (shown with plus sign) tested against the Pitot tube (shown as a probe). Considering the contours of wind speed at tunnel's test section area, both the instrument and the Pitot tube were positioned 60 cm from the bottom wall.

The experiments were conducted at four wind levels (2, 4, 6, and 8 m s⁻¹). At each wind level continuous measurements for five minutes were performed. The data for each wind level was then averaged for both TriSonica™ Mini and the Pitot tube to derive the mean wind velocity components. The setup of the experiment is shown in Fig. 2.15.

The blockage ratio, defined as the projected area of the structure in flow direction over the cross sectional area of the domain around the structure, is calculated by means of splitting the instruments into multiple projected surfaces then calculating and finding the summation of the surface areas. The most concerning setup (gondola against Pitot tube) is found to have a blockage ratio of 4.2 % while other setups exhibit a lower blockage ratio.

An array of six blocks was placed upstream; the block height, width, and spacing are 14 cm, 4 cm, and 50 cm, respectively. The effect of the blocks on the contours of wind velocity at the test section area is determined in the same manner explained before. Figure 2.16 shows the contours of wind velocity at the test section area at the four wind levels. Comparing the contours of wind speed across the test section presented in Fig. 2.16 and Fig.2.12, one could conclude that introducing the upstream blocks created a more homogeneous velocity pattern in the tunnel cross section.



Figure 2.15: The view of TriSonica™ Mini (left) and the Pitot tube (right) in wind tunnel.

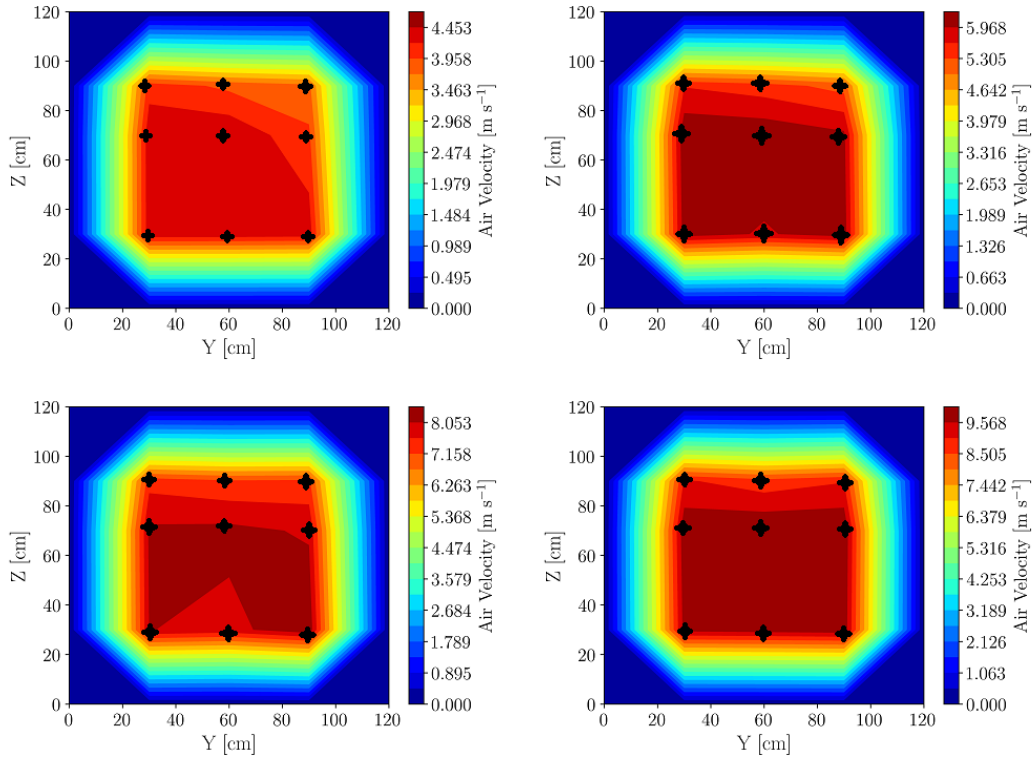


Figure 2.16: Contours of wind velocity at four wind levels (2, 4, 6, and 8 m s⁻¹) with array of blocks upstream. The measurement locations are marked on the plots. Note, introducing the upstream blocks slightly increases the wind speed at each level compared with the Fig.2.12.



Figure 2.17: The view of R.M. YOUNG 81000 (left) and Pitot tube (right) at wind tunnel.

2.4.2 Procedure for Assessing TriSonica™ Mini Performance in Measuring Turbulence Statistics

To assess TriSonica™ Mini's performance in measuring the turbulence statistics of a flow field, the turbulence variables were compared to the results of the same experiment using the R.M. YOUNG 81000 and Pitot tube measurements. The R.M. YOUNG 81000 wind tunnel experiments were conducted at the same conditions as those of TriSonica™ Mini. Figure 2.17 shows the setup of the experiment. The turbulence statistics of wind velocity, including the variances and covariances, that were measured by TriSonica™ Mini and R.M. YOUNG 81000, were compared with one another.

2.5 Procedure for Gondola Calibration

In the next step, TriSonica™ Mini was mounted onto the gondola, while the performance of the gondola (or the effects of the frame on TriSonica™ Mini) on the measurements were assessed in comparison to Pitot tube and R.M. YOUNG 81000 measurements. By adding multiple degrees of freedom, the setup for this test was designed to simulate the gondola's motion in the ABL. The gondola is attached to the top ceiling of the tunnel with two ropes (resembling the ropes to the balloon) and a single rope to the bottom floor (resembling the rope to the ground operator). The gondola faces against the main wind flow direction as it does in the ABL. Figure 2.18 shows the gondola's setup in the tunnel alongside with the Pitot tube.



Figure 2.18: The view of gondola and Pitot tube at the wind tunnel.

The calibration for the horizontal wind velocity vector is conducted at five azimuth angles 0° , 45° , 90° , 135° , and 180° . Each test continued for a period of five minutes at three wind levels including 2, 4, and 6 m s^{-1} . In order to better quantify the performance of gondola in measuring the turbulence statistics, the experimental setup and test configurations were set in accordance with the previous R.M. YOUNG 81000 wind tunnel tests against the Pitot tube.

2.6 TANAB Field Observation

The first environmental monitoring field campaign of the TANAB system was conducted in an open-pit mining facility in northern Canada in May 2018. TANAB measured the dynamics of the atmosphere at different diurnal times (e.g. day versus night) and locations (near tailings pond versus inside the mine).

The system measured meteorological conditions including wind speed in three directions, temperature, relative humidity, and pressure over the first few tens of meters of the atmospheric boundary layer. The TANAB measurements of mean and turbulence statistics were then post processed and corrected by introducing the findings of the wind tunnel tests.

2.7 Summary

In this chapter, the methodology for the development of the Tethered And Navigated Air Blimp (TANAB) system was fully described. The dynamic motion of the system alongside with the stabilizing mechanisms were fully explained. In order to investigate the performance of the system, a series of wind tunnel experiments were conducted. The experiments assessed the performance of the onboard TriSonicaTM Mini sensor under different scenarios against other reference sensors. The effect of the mounted platform on TriSonicaTM Mini's measurements was investigated.

Chapter 3

Description of the Weather Research and Forecasting (WRF) Model

This chapter presents an approach in understanding the physics of the Atmospheric Boundary Layer (ABL) from the mesoscale modelling point of view. The Weather and Research Forecasting (WRF) model is the new generation of the mesoscale numerical weather prediction system that is designed for both research and operational forecasting applications. WRF was developed in the late 1990s in a joint partnership of the National Center for Atmospheric Research (NCAR), the National Oceanic and Atmospheric Administration (NOAA, represented by the National Centers for Environmental Prediction (NCEP) and the (then) Forecast Systems Laboratory (FSL)), the (then) Air Force Weather Agency (AFWA), the Naval Research Laboratory, the University of Oklahoma, and the Federal Aviation Administration (FAA). The WRF system works with two dynamical solvers, Advanced Research WRF (ARW) core and the Nonhydrostatic Mesoscale Model (NMM) cores.¹ In this chapter, a review of the model's dynamics is provided followed up by a methodology to adapt the model to the recent land use and topographical changes associated with the open pit mining facility. The importance of this chapter is outlined into the flow chart presented in fig. 3.1.

3.1 Introduction to WRF

The WRF model solves the fully compressible Eqs. 3.2 to 3.7 and non-hydrostatic² form of the Euler equations in flux form. The set of equations resolve the vertical momentum profiles

¹<https://www.mmm.ucar.edu/weather-research-and-forecasting-model>.

²A complete set of Navier-Stokes equation combined with heat conduction for inviscid flow.

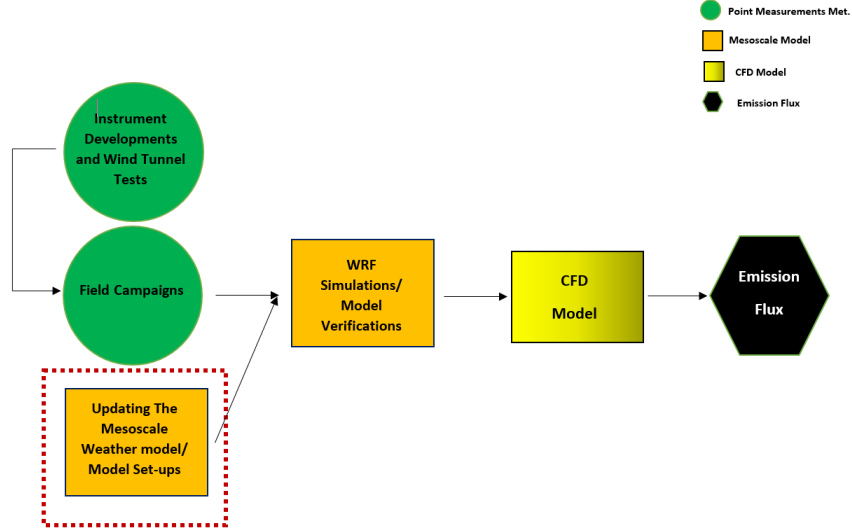


Figure 3.1: Mesoscale modelling as it is outlined in the flow chart of the overall project.

in order to better quantify the synoptic phenomena where the horizontal and vertical length scales are of the same order of magnitude. The equations are in a conservative form suitable for finite volume discretization methods. The equations further account for humidity and temperature in the atmosphere, while neglecting viscosity above ABL because air can be treated as an inviscid fluid in that region of the atmosphere [67]. However, within ABL, viscosity and hence turbulence is accounted for using a Planetary Boundary Layer (PBL) scheme or a Large-Eddy Simulation (LES) scheme.

3.1.1 Vertical Coordinate

WRF ARW builds the vertical coordinate by integrating the isobaric and terrain following approaches. Equation 3.1 generates the dry hydrostatic pressure corresponding to each vertical level. The first two terms on the right hand side represent the terrain following approach and the last term accounts for the isobaric (constant pressure) methodology. $B(\eta)$ could be programmed to turn into zero at any vertical point in which the vertical coordinates will be built upon the isobaric concept above that point. The hybrid terrain-following vertical coordinate system stops the computational grids to pass through the terrain near the surface while capturing the details of the topography and at the same time simplifies the vertical coordinate system at the top of the domain where the effect of the surface is negligible. Figure 3.2 schematically shows the concept of the hybrid terrain-following vertical coordinate

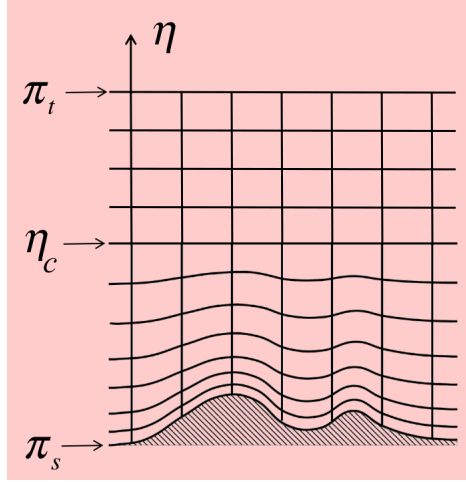


Figure 3.2: Schematic of hybrid-terrain following vertical coordinate system; figure extracted from [62].

system.

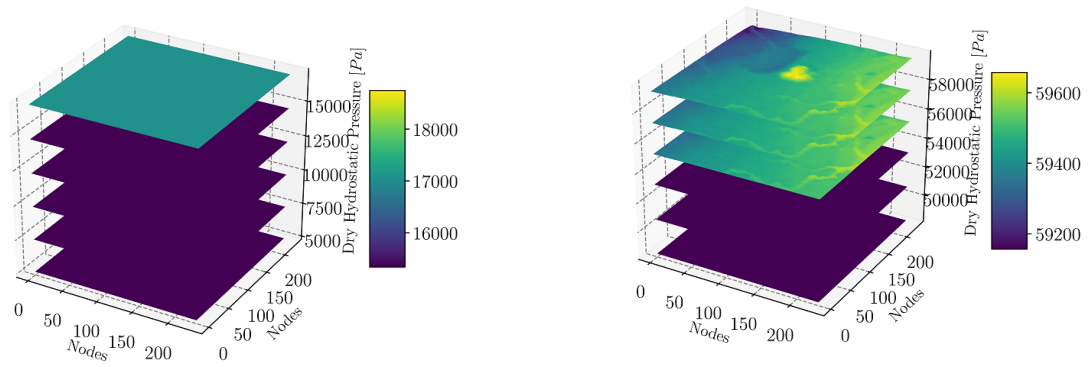
$$\Pi_{dryair}(\eta) = B(\eta) \times \mu_{dryair} + \Pi_{top} + (\eta - B(\eta)) \times (\Pi_0 - \Pi_{top}), \quad (3.1)$$

where Π_{dryair} is the dry hydrostatic pressure, $B(\eta)$ is the function that changes between isobaric and terrain-following coordinate, η assigns to the vertical level and it varies from a value of 1 at the surface to 0 at the upper boundary of the model domain, μ_{dryair} is the column mass (per unit area), Π_{top} is the dry hydrostatic pressure at top of the domain, and Π_0 is the dry hydrostatic pressure at the surface.

Figure 3.3 presents the hybrid terrain-following vertical coordinate system generated in accordance to Eq. 3.1. The base pressure is set from one case study over the mining site of interest. $B(\eta)$ turns into zero at $\eta = 0.5$. Figure 3.3a shows the first five vertical grid levels close to the surface of the mining facility. Figure 3.3b shows the transition between the terrain-following coordinate system and the isobaric coordinate system. Figure 3.3c shows the last five levels of the vertical coordinate system on top of the computational domain that follow only the isobaric assumption.

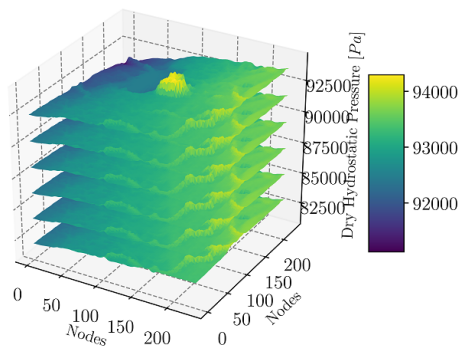
The mass of the dry air can then be considered as the gradient of the dry pressure (as generated by Eq. 3.1). The WRF ARW dynamic solver then solves the conservative non-hydrostatic form of the Euler equation to resolve the following prognostic conserved variables

- μ



(a) Top five layers close to the model's top.

(b) Transition between terrain-following and isobaric layers.



(c) First five layers near surface.

Figure 3.3: Hybrid terrain-following vertical coordinate system.

- $\mathbf{U} = \mu\mathbf{u}$,
- $\mathbf{V} = \mu\mathbf{v}$,
- $\mathbf{W} = \mu\mathbf{w}$,
- $\Theta = \mu\theta$,

where μ represents the normalized mass per unit area within the column in the model domain at horizontal coordinates (x, y) . \mathbf{U} , \mathbf{V} , and \mathbf{W} are the flux form of the covariant velocities in the two horizontal and vertical directions, respectively. Θ represents the flux form of the potential temperature. The only non-conserved variable is Geopotential, which is defined as the work performed against gravity to lift 1 kg of mass from sea level up to height H . It has units of $\text{m}^2 \text{s}^{-2}$ [69] and can be written as $\Phi = gZ$, where g is the gravitational acceleration and Z is height above the ground.

WRF uses the C-grid staggering method to store the variables within each computational domain. U , V , W , and Φ are stored at the grid boundaries and μ , θ , q (mixing ratio for the water vapor, cloud, and rain) are stored at the grid's center. Figure 3.4 shows the distribution of the variables within each computational cell.

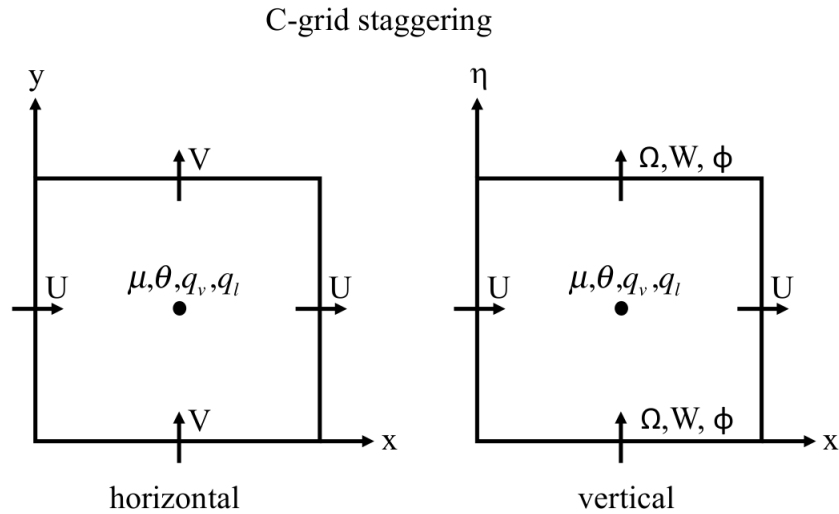


Figure 3.4: C-grid staggering; figure extracted from [62]. Ω is the contravariant of the vertical velocity.

3.2 Governing Equations

The flux form of Euler equations using the variables defined in the previous section can be written as³:

$$\partial_t U + (\nabla \cdot \mathbf{V}u) - \partial_x(p\phi_\eta) + \partial_\eta(p\phi_x) = F_U, \quad (3.2)$$

$$\partial_t V + (\nabla \cdot \mathbf{V}v) - \partial_y(p\phi_\eta) + \partial_\eta(p\phi_y) = F_V, \quad (3.3)$$

$$\partial_t W + (\nabla \cdot \mathbf{V}w) - g(\partial_\eta P - \mu) = F_W, \quad (3.4)$$

$$\partial_t \Theta + (\nabla \cdot \mathbf{V}\theta) = F_\Theta, \quad (3.5)$$

$$\partial_t \mu + (\nabla \cdot \mathbf{V}) = 0, \quad (3.6)$$

$$\partial_t \phi + \mu^{-1}[(\mathbf{V} \cdot \nabla \phi) - gW] = 0, \quad (3.7)$$

where F_U , F_V , F_W , and F_Θ represent forcing terms arising from the model physics, turbulent mixing, spherical projections, and earth's rotation. The inverse density (α) can then be determined using

$$\partial_\eta \phi = -\alpha \mu. \quad (3.8)$$

The equation of state can be written as

$$p = \left(\frac{R_d \theta}{p_0 \alpha} \right)^\gamma, \quad (3.9)$$

where $\gamma = \frac{c_p}{c_v} = 1.4$ is the ratio of air specific heats, and R_d is the gas constant for dry air. Note the pressure p is normalized by a reference pressure p_0 (typically 100,000 Pa). The terms on the right hand side of the Eqs. 3.2 to 3.5 are the forcing terms that result from the model's physics, PBL parameterization, spherical projections, and the earth rotation.

The first term in Eqs. 3.2 to 3.7 shows the rate of change of variables in time or the storage term. The second term accounts for the advection or transport of the variable of interest across the flow (u , v , w , and θ). The other two terms on the left-hand-side of Eqs. 3.2 to 3.4 account for pressure gradient that drives the transport.

³The effect of moisture is not considered in these equations; the set of flux form of Euler equations including the moisture can be found at [62].

3.3 Road Map for Adapting the WRF Model to the Mining Facility

The WRF system is made up of multiple independent components including the initialization data generator (WPS), the solver (including the dynamic cores, physics schemes, numerics, dynamics options, initialization routines, and a data assimilation package), and the post processing package. Each dynamic core (WRF-ARW and WRF-NMM) corresponds to a set of dynamic solvers that operate on a particular grid projection, grid staggering, and vertical coordinate system. The WRF model also contains a multitude of physical parameterizations, many of which can be used with both dynamic cores. The current study utilizes the Unified Environmental Modeling System (UEMS) distribution of WRF which is a complete, full-physics, state-of-the-science Numerical Weather Prediction (NWP) package that incorporates the NOAA (NEMS) and WRF systems into a single user-friendly, end-to-end forecasting system. Nearly every element of an operational NWP system has been integrated into the UEMS, including the acquisition and processing of initialization data, model execution, output data processing, and file migration and archiving.⁴

The first step of a WRF simulation is to define and generate the computational domain into the model. This includes 1) identifying the map projection, 2) locating the boundaries of the domains, and 3) setting horizontal grid spacings. The computational domain can be comprised of either one or multiple nests with an option to enable the feedback between the nests. The preprocessing software further localizes the computational domain by extracting the terrestrial data from the global dataset and assigning them into the computational grid. This includes topography, land use, land mask, Coriolis parameters, soil temperature, and albedo.

The computational domain in the present study is comprised of five nested domains centered around the mining site of interest. Figure 3.5 shows the five nested domains and surface elevation. The five nested domains approach has demonstrated its success in previous research [73]. The grid spacing at each nested domain is 1/3 of grid spacing in its parent domain. A separate study has investigated the effect of varying the grid resolution on simulation results [53]. Table 3.2 summarizes the grid horizontal spacing options for the WRF simulations in this study. The projection system is set to be the Lambert conformal conic projection system.

Next, the initial and boundary conditions are identified, acquired, and processed to be used

⁴<http://strc.comet.ucar.edu/software/uems/>

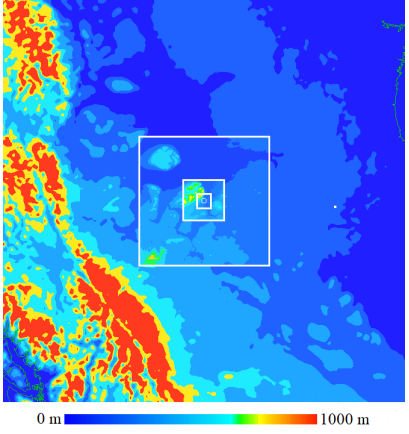


Figure 3.5: Five nested domains and surface elevation.

Domain ID	Resolution [m]
Domain 01	7000
Domain 02	2333
Domain 03	777
Domain 04	256
Domain 05	86

Table 3.1: The choice of horizontal grid spacing.

by the simulation. This data is available from global models that run over the entire globe round the clock. The global models are run on coarse grid resolutions, hence, in order to use them as an initial or boundary condition for the refined simulations, the information needs to be interpolated horizontally and vertically into the computational domain of interest, which is most likely set up at higher horizontal and vertical resolutions.⁵ For the present study, the models are initialized using the Global Forecast System (GFS) 0.5 °-resolution dataset.⁶

At the simulation step, the solver first interpolates the previously processed information horizontally and vertically to generate three dimensional initial and boundary conditions, and then the dynamic core starts running the simulation.

3.3.1 PBL Schemes and Physics Models in WRF

The PBL schemes are used to distribute surface fluxes via boundary layer eddy fluxes and allow for PBL growth by entrainment. Enabling the PBL scheme means the model does not resolve the eddies but instead parametrizes their effect in the vertical transport of variables of interest. In cases when horizontal spacing is smaller than 500-1000 m, alternatively, enabling the Large Eddy Simulation (LES) mode can account for three dimensional structures of the eddies and thus transport. WRF ARW offers both local and non-local PBL schemes. The PBL physics on the other hand, models the subgrid-scale vertical interaction of surface heat, moisture, and air constituent fluxes such as nonlocal transport, entrainment near PBL top, transitions between Stable Boundary Layer (SBL), and the Convective Boundary Layer (CBL) [62].

The present study uses the non-local Yonsei University (YSU) PBL scheme [73]. This work does not study the effect of various PBL physics schemes, hence, those options are left unchanged. Table 3.2 summarizes the physics parameterizations used in the present work.

3.4 Updating the Terrestrial Information

The preprocessing software acquires the static information (including topography and land use) from the global dataset. Sometimes the terrestrial data are not updated with the latest land use or topographical changes such as fast pace industrial activities that completely

⁵The setups for multiple cases were prepared by the author and run on the AIR Lab server.

⁶WPS acquires the GFS data from two FTP sources (NCEP and TGFTP), two HTTP sources (STRC and TOC), and two NFS sources (DATA1 and the local system). The order of these servers are semi randomized, so WPS starts from one and moves on to the other one if it is not successful in acquiring the data.

Physics	Micro physics model
Micro physics	Lin et al. scheme [47]
Long wave radiation	Dudhia scheme [22]
Short wave radiation	Dudhia scheme [22]
Surface layer physics	MYJ Monin-Obukhov
Cumulus physics	Multi-scale Kain-Fritsch scheme [78]

Table 3.2: The micro physics parameterizations used in the WRF simulations.

changes a region (e.g. a rapidly changing open-pit mine). Studying the local meteorology over such modified regions based on old terrestrial data is highly questionable. In addition, the local meteorology is highly dependent on local microscale phenomena, while the default global datasets are provided at relatively low resolution. A procedure to acquire and incorporate high resolution static information including topography and land use changes and incorporating them into the global terrestrial data was needed to ensure accurate simulation of a rapidly changing open-pit mine environment.

The following section presents the applicable methodologies to integrate land use and topographical modifications into the Unified Environmental Modelling System (UEMS) distribution of WRF model. The flowchart presented in Fig. 3.6 and Fig. 3.7 shows the road map to update the data structure of the model.

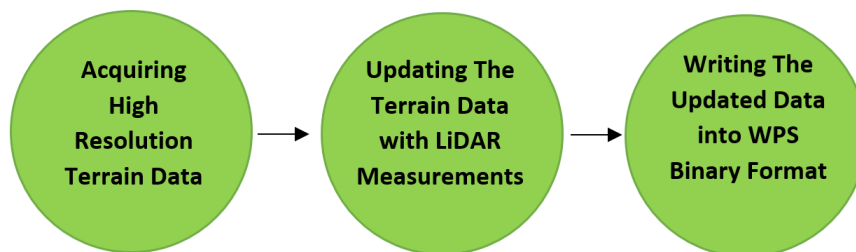


Figure 3.6: The road map to update the topography dataset.

3.4.1 The Choice of Static Dataset

The UEMS distribution of the Weather Research and Forecasting (WRF) model currently builds up the computational domain based on USGS GTOPO30 terrain data at 10', 5', 2', and 30'' horizontal resolutions (or approximately the highest horizontal resolution of 1 km at the equator). Generating horizontal grid resolutions smaller than 1 km introduces

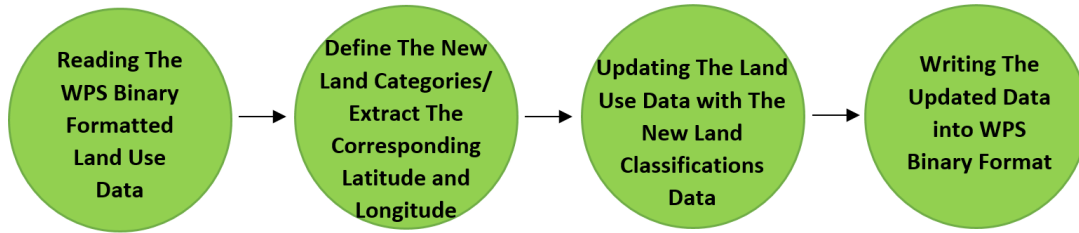


Figure 3.7: The road map to update the land use data set.

errors into the calculations as the model attempts to interpolate the terrain data from the neighbouring points that are non-existing. Alternatively, introducing the Shuttle Radar Topography Mission (SRTM) terrain dataset at 1" horizontal resolution (or approximately 30 m at the equator) will result in creating higher horizontal resolutions.

For land use classification, the default UEMS offers different varieties of land use classification datasets. These include

- MODIS modified-IGBP land use - 500 m (updated in Feb., 2014),
- 24-category USGS land use (updated in Jan., 2013) .

Neither the SRTM terrain dataset nor the default land use data in UEMS are recent enough to include the latest state of the mining operations under study in northern Canada. Hence, an attempt to incorporate a recent dataset from Light Detection And Ranging (LiDAR) and a recent satellite observation of land use classification would be of high value in modelling of transport phenomena in the ABL for the facility under study. This section covers the following contents, all of which were original contributions by the author to the overall research project:

- Adding high resolution terrain data in UEMS,
- Updating the high resolution data with the latest LiDAR data in UEMS,
- Updating the MODIS land use classification in UEMS.

3.4.2 Adding the SRTM Terrain Data

SRTM terrain data has been open for public access since 2015. The terrain data is at 1" horizontal resolution (or approximately 30 m at the equator). The data covers most of the land surfaces that lay between 60° north and 54° south latitudes. That is about 80 % of all

the land on Earth. The data can be downloaded in ASCII format available in hundreds of tiles that cover the surface of the earth.⁷ The tiles are available for download at different resolutions, but, the minimum resolution (maximum tile size) is set to be $2^\circ \times 2^\circ$.

The ASCII file contains numbers of columns and rows filled with an integer representing the elevation of the terrain. An overall description is presented on the first six lines of each file that contain the following information

- Number of the rows,
- Number of the columns,
- A single grid spacing at latitude and longitude directions in degrees,
- The latitude with respect to the lower left corner of the tile,
- The longitude with respect to the lower left corner of the tile,
- Missing values.⁸

The ASCII files cannot be fed into UEMS directly as it uses a specially formatted terrain data called WPS geogrid binary. The author adapted a Fortran code in Appendix A.1 in conjunction with a C subroutine in Appendix A.2 to read the ASCII files and then convert them to WPS geogrid binary. To compile and run the Fortran program, a series of command lines were executed in a Linux terminal as listed in Appendix A.3.

The WPS geogrid binary formatted file is named by the number of rows followed by the number of columns. The UEMS model is able to import the geogrid binary formatted file alone or in a group of same-size tiles. Using either of these two approaches, an index file representing the configuration of the original ASCII file, similar to the overall description, is needed and mandatory to use to be placed at the WPS binary folder. In fact, the index file locates the latitude and longitude corresponding to the lower left corner of the lowest (south) left (west) tile, the size of each tile (in the x and y directions), the grid spacing (0.000277777785° for both the x and y directions in this study), and the missing values.

Since adding multiple SRTM WPS geogrid binary files may generate inhomogeneity or discontinuity at the borders of the tiles when processed by the geogrid program (prior to being fed into the WRF dynamic core), a $2^\circ \times 2^\circ$ SRTM $1''$ tile around the mining area was

⁷<https://gdex.cr.usgs.gov/gdex/>

⁸The data alongside the borders of the tiles are recorded as -32768 that reads as a missing value.

downloaded from USGS in the present study.⁹ This tile extends 100 km in longitude and 222 km in latitude. The contents of the index file is presented in Appendix A.6. Figure 3.8 shows the inhomogeneity and discontinuity resulted by adding multiple tiles. At the border of the tiles, patches develop where the terrain height drops 200 m unexpectedly.

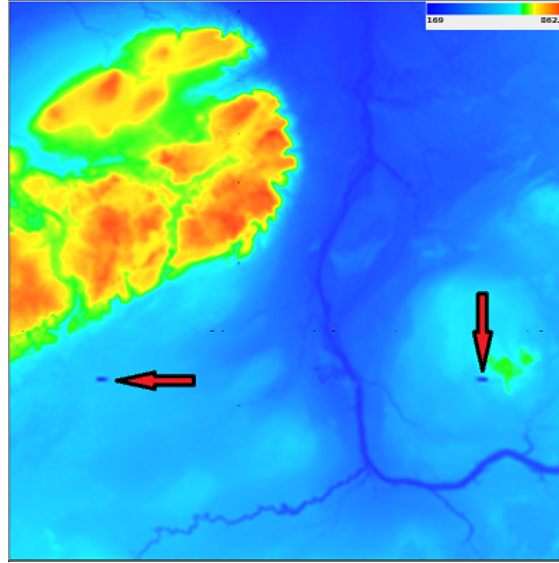


Figure 3.8: Inhomogeneity and discontinuity resulted by adding multiple SRTM tiles; at the border of each tile, series of terrain height inconsistencies appear that are up to 200 m. Note, the source of Inhomogeneity goes back to the SRTM data set.

3.4.3 Updating The SRTM Terrain Data with Mining Facility LiDAR Data from 2018

The mining facility LiDAR data from 2018 was provided by a third party consultant. The data exhibits a horizontal accuracy of approximately 10 cm, a vertical accuracy of approximately 1 m, and an areal coverage of 300 km². The data is available in a series of three-column text files including x , y and z (terrain height) in an unspecified order. By listing the name of the files in an order into a table, the path of the plane that carried the LiDAR measurement are identified and presented in Fig. 3.9. This understanding is a key step to relate the LiDAR data to the corresponding latitudes and longitudes.

The map of the LiDAR data (processed using the ParaView software) was imported into and adjusted within the Google Earth software, as shown in Fig. 3.10. In the next step, the

⁹<https://gdex.cr.usgs.gov/gdex/>

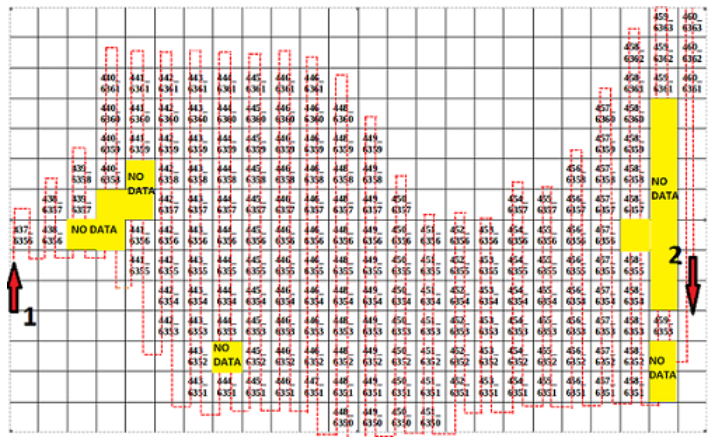


Figure 3.9: Aircraft’s pathway (red dashed line) over the mining facility as mapped by the ordered LiDAR filenames; note that the LiDAR data is missed in yellow squares. The aircraft started measurements at point 1 and finished at point 2. The numbers in the blocks indicate the LiDAR data filenames.

latitude and longitude with respect to the left most (west) and right most (east) locations of the data were identified. Using a Python program developed by the author, all the LiDAR data were assigned to their corresponding latitudes and longitudes. This code is provided in Appendix A.5. The generated latitudes and longitudes are then assigned to the data by sorting first the x (longitude) and then y (latitude) of a five-column matrix using Excel.



Figure 3.10: LiDAR map (processed in ParaView) on top of the mining facility. The extreme top, bottom, left, and right are pin pointed and their corresponding latitude and longitude are identified.

In the next step, the LiDAR data (corresponding to latitudes and longitudes) substituted into SRTM data. The algorithm simultaneously compares SRTM data’s latitude and longitude at each point with the LiDAR data’s latitude and longitude and where the difference for both the latitude and longitude is less than 0.001° , it substitutes the SRTM elevation with the LiDAR elevation data. The code developed by the author for this operation is provided

in Appendix A.4. To make the algorithm faster, the “numba” library (an optimized compiler for Python that works best on codes that use functions) was considered.

In the last step, the modified SRTM data was converted into standard ASCII format (rows and columns of elevation data) including the explained description on the header. The ASCII file is then converted into WPS geogrid binary format using the same algorithm described earlier. The new WPS geogrid binary file is then placed into a new folder together with an index file representing the tile under `uems/data/geog`.

As stated earlier, UEMS retrieves the topography information from GEOTOPO 30'' dataset. In order to use the new dataset, the content of GEOGRID.TBL.ARW needs to be modified by updating the pathway to the new folder.

3.4.4 Modifying Land Use Classification

The procedure to update the land use classification with the current mining facility activities starts differently from the terrain modification in the sense that in the latter we had the ASCII form of the data, but in the former we have access to the WPS geogrid binary form of the data. The WPS geogrid binary could be converted to text format using Python, but the result is not correct. Figure 3.11 shows the result of this attempt, by converting one of the MODerate resolution Imaging Spectroradiometer (MODIS) 15'' land use data into the ASCII format using Python and then converting the ASCII into WPS geogrid binary format using the algorithm described earlier.

Alternatively, QGIS version 3.4 is used to convert the MODIS WPS geogrid binary data into ASCII format. As with the terrain data, the MODIS WPS geogrid binary dataset includes tiles covering the earth. The dataset modified most recently in April 2014 was not recent enough for our analysis of the mining facility in 2018. Figure 3.12 shows the original MODIS land use tile covering the area of interest. The WPS geogrid binary dataset could be imported as a layer into QGIS and then under the “raster→translate” tool the WPS geogrid binary is converted into ASCII format. Note that the converted ASCII format is up-side-down, hence before using the data the matrix was corrected into the normal form by reordering the rows.

The ASCII format contains rows and columns filled with integers ranging from 0 to 20 representing a land category. In order to modify the matrix with the latest land use changes in the region, the land classes with respect to each area of the mining facility were classified and assigned to the corresponding latitude and longitude.

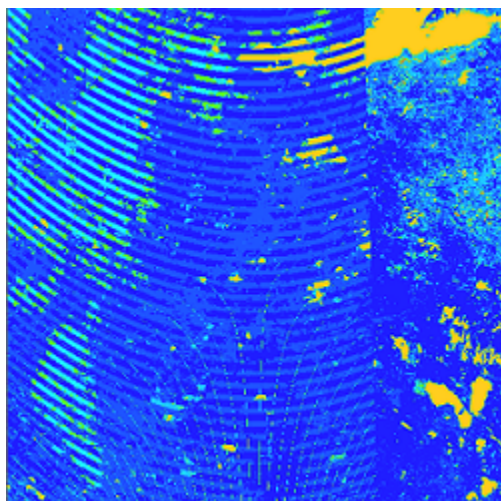


Figure 3.11: Noise in the data when MODIS Land Use 20-class 15'' WPS geogrid binary format is read by Python and is converted to WPS geogrid binary format. The selected tile covers the land between 50° to 60° latitude and -120° to -108° longitude including the mining facility. Note that the re-generated tile is presented adjacent to the original tile. (left: the re-generated tile and right: the original tile)

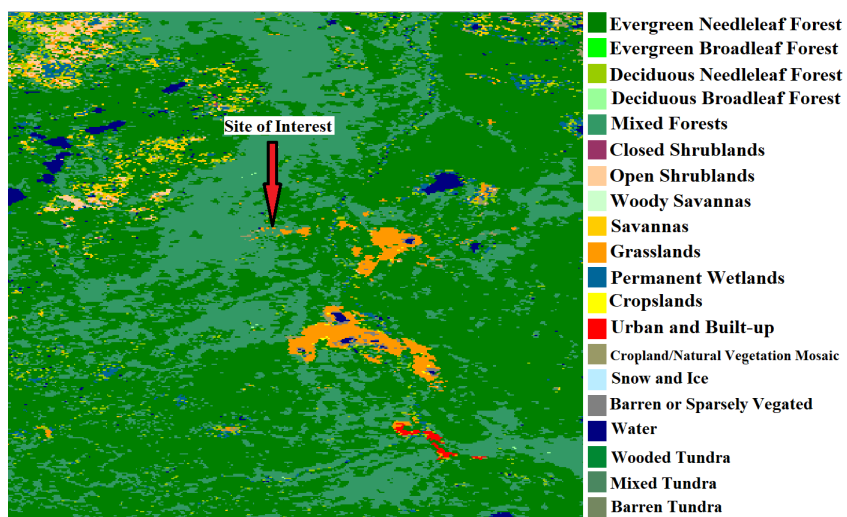


Figure 3.12: Original MODIS 15'', 20-class product at the mining facility area of interest colour-coded per classifications of Friedl et al. [25], modified in April 2014.

Google Earth was used to generate these classifications. As shown in Fig. 3.13, using the most recent Google Earth aerial pictures of the facility, dated June 2018, land use classifications were derived for the whole facility. Figure 3.14 shows the colour-coded land use classifications overlaid on the mining facility map with respect to the standard MODIS land classes.



Figure 3.13: Most recent satellite picture of the mining facility; Google Earth, June 2018.

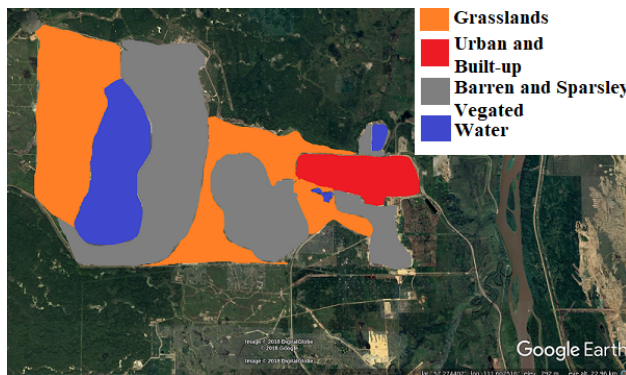


Figure 3.14: Colour-coded land use classifications overlaid on the mining facility map with respect to the standard MODIS land classes: Grasslands = 10 (orange), Urban and Built-up = 13 (red), Barren and Sparsely Vegetated = 16 (gray), and Water = 17 (blue) colour-coded per classifications of Friedl et al. [25].

The latitude and longitude with respect to the group of points for each area extracted from Google Earth using a mesh of paths. Then three-column text files (latitude, longitude, and land use classification) with respect to each area were generated. Using the same substitution algorithm described earlier (the difference set to be 0.01° this time), the new land use classifications were fed into the MODIS 15'' 20-class product. In the last step, the updated land use classifications in ASCII format were converted to WPS geogrid binary format and

replaced the old WPS geogrid file under the `uems/data/geog/modis_landuse_20class_15s` directory.

3.4.5 Updated High Resolution Topography and Land Use Classification

This section presents the results of both the terrain and land use classification modification after they were successfully made and implemented in UEMS. The new domains were built on top of these newly-modified topography and land use class. The smallest horizontal grid spacing was set to be 86 m for the inner domain around the mining facility.

Geogrid is a pre-processing program for the WRF model. It provides values for static (time-invariant) fields at each model grid point. Terrain data and land use classification are among the statics that make the structure of the computational domain. The updated SRTM terrain dataset and the updated MODIS land use classification data replaced by the default Geogrid data, and the computational domain built on top of the new data. For the purpose of this study the grid spacing for the inner domain, that extended over the mining facility, is refined down to 86 m.

Figures 3.15 and 3.16 show the topography and land use respectively for the inner domain processed by the Geogrid program. The horizontal grid spacing is 86 m with 232 cells extended in x and y directions. Geogrid produces the static files in the netCDF format, and the Integrated Data Viewer (IDV) or Python can be used to visualize this dataset.

3.5 Incorporation of a Lake Model

The mining facility includes multiple water bodies such as a fresh water reservoir and a tailings pond. A one dimensional physically-based lake model was coupled to the UEMS. The model simulates physical processes such as the lake thermal condition as well as the lake atmosphere interaction to capture the local and regional meteorological effects of a lake. The lake model includes a scheme to balance mass and energy. There are 20-25 model layers, including up to 5 layers of snow on top of the lake ice, 10 water layers, and 10 soil layers on the lake bottom.

According to Subin et al. [71] and Gu et al. [30] the lake scheme is independent of a land surface scheme and therefore can be used with any land surface scheme embedded in WRF. The lake scheme was retrieved from the Community Land Model version 4.5 [57] with some

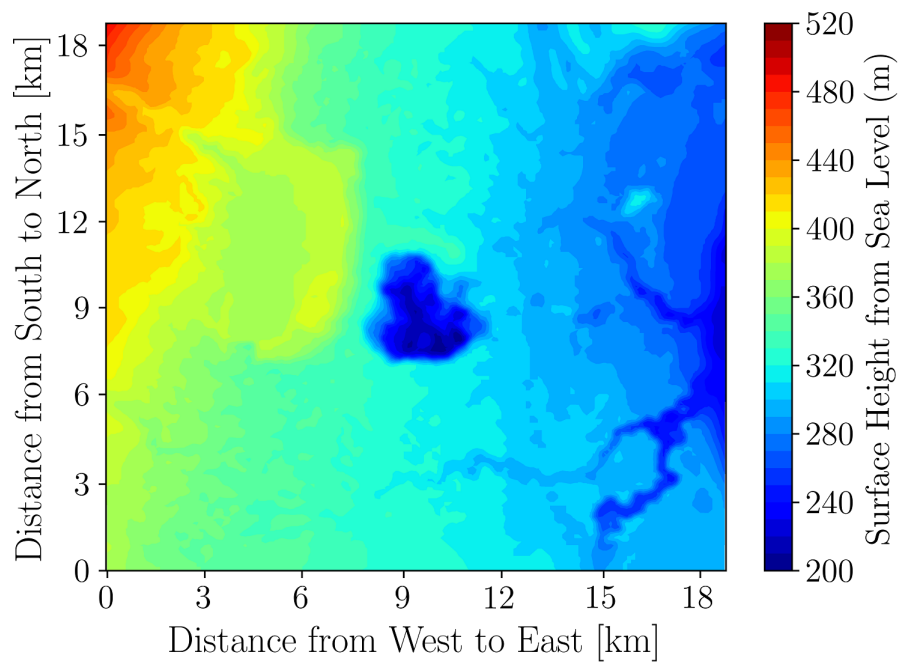


Figure 3.15: The updated topography, over the mining facility, with the latest LiDAR dataset; figure extracted from [53].

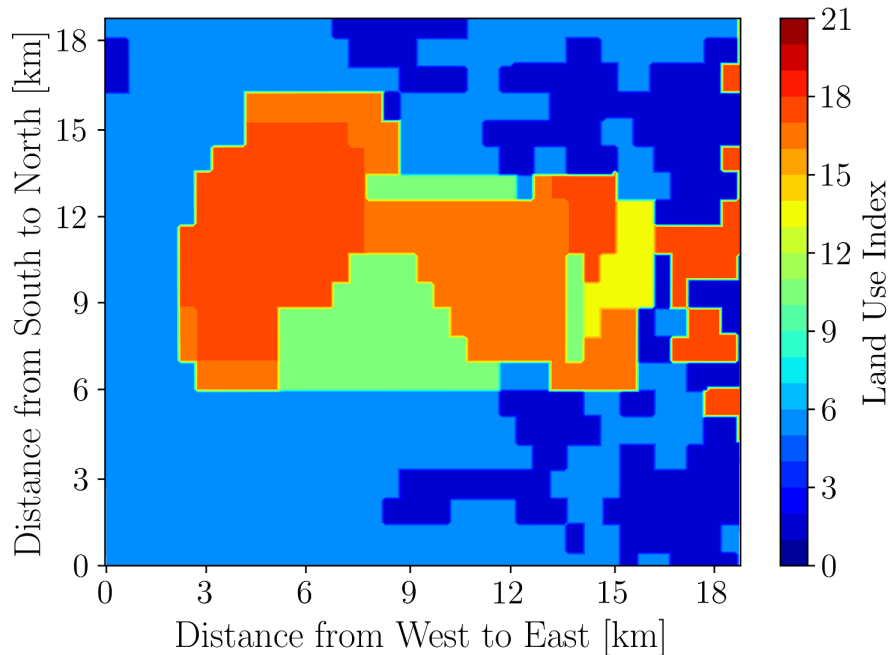


Figure 3.16: The updated land use classifications; figure extracted from [53].

other modifications [30].

The choice of the land use becomes limited upon introduction of lakes into the model as only a few datasets include the lake category. For the present study MODIS land use 21 class 30" resolution was incorporated. The lake counts as class 21 and in that case is differentiated from the rest of the bodies of water in the model. The latter counts as sea and this study showed the surface temperature of the body of water remain unchanged during the whole simulation period when it is assigned as a sea.

Prior to the dynamical simulation, the static information of a designated lake including lake depth needs to be integrated into the model. For the present study the depth of 50 m was assigned to the lakes in the model and that includes the pond and other smaller water reservoirs within the facility. The size and boundaries of the lakes are determined from the recent satellite and aerial images. Enthusiastic readers are highly encouraged to read the Technical Description of version 4.5 of the Community Land Model (CLM) because the purpose of this study is not to explore the lake model rigorously, but to demonstrate how an introduction of a body of water affects the meteorological predictions.

3.5.1 UEMS Predictions Compared with Air Soundings

For the purpose of the present study, data from two radiosonde stations including 1) Fort Smith observation and 2) Edmonton Stony Plain observations was retrieved.¹⁰ The data covers the whole simulation period. The sounding data are available at 00Z and 12Z for each day for both stations. The measurements include pressure, temperature, potential temperature, virtual temperature, relative humidity, water vapor mixing ratio, horizontal wind speed (by means of a tracker that measures the balloon drift), wind direction, and the height above the ground.

3.6 Conclusions

In this chapter, the Weather Research and Forecasting (WRF) model was introduced, which is capable of predicting mesoscale and microscale meteorological phenomena. A particular distribution of WRF called the Unified Environmental Modelling System (UEMS) was introduced. A description of the UEMS model and the governing equations as well as the computational grid structure were explained in detail. A new approach was also discussed to adapt the UEMS model to the mining facility by incorporating the most recent topographical and land use classification changes in the mining site. This will enable the UEMS model to predict the local meteorology more successfully.

¹⁰The sounding data is open to the public and can be downloaded from <http://weather.uwyo.edu/upperair/sounding.html>.

Chapter 4

Results and Discussion

The results are presented in two parts. The first part discusses the results of experimental methods established to calibrate the TriSonicaTM Mini. This part also shows the field observations of the sensor as launched using the Tethered And Navigated Air Blimp (TANAB) system. The second part discusses the results of the UEMS model that was adapted to the mining facility topography and land use classifications. This part also provides limited model-observation comparisons using sounding data and the TANAB. The full study for model-observation comparison is performed by Nahian et al. [53].

4.1 Part 1: Meteorological Sensing

4.1.1 TriSonicaTM Mini Performance against Pitot Tube

This section presents the results of TriSonicaTM Mini's performance against Pitot tube in measuring the mean wind components. For these tests data was sampled at 10 Hz by both sensors and time averaged for 5 min. Figure 4.1 shows TriSonicaTM Mini's mean horizontal wind speed measurements against the Pitot tube with change in the TriSonicaTM Mini's azimuth angle. With increase in wind speed, TriSonicaTM Mini slightly underestimates the Pitot tube measurement. The underestimation is slightly higher when the azimuth angle is equal to 0° and 180°, but, the accuracy improves when it is 90° or 270°.

Table 4.1 presents the quantitative comparisons for measuring mean wind speed between TriSonicaTM Mini and the Pitot tube based on the bias, Root Mean Square Error (RMSE), and Mean Percentage Error (MPE) defined by

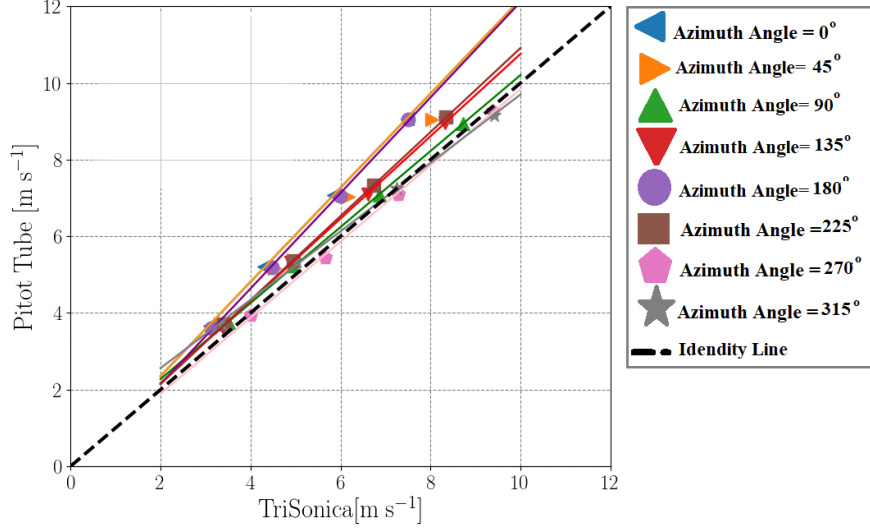


Figure 4.1: TriSonicaTM Mini's performance in measuring mean wind speed against Pitot tube at different azimuth angles.

Error \ Azimuth Angle	0°	45°	90°	135°	180°	225°	270°	315°
Bias [m s ⁻¹]	-1.080	-0.728	-0.241	-0.449	-0.950	-0.515	0.138	-0.102
RMSE [m s ⁻¹]	1.143	0.765	0.244	0.470	1.034	0.546	0.149	0.271
MPE [%]	-17.073	-11.614	-4.351	-7.203	-14.771	-8.021	2.234	-3.151

Table 4.1: Effects of the change in azimuthal angle on TriSonicaTM Mini's performance in measuring mean wind speed calculated in terms of bias, RMSE, and MPE.

$$\text{Bias} = \frac{1}{n} \sum_{i=1}^n (I_i - R_i), \quad (4.1)$$

$$\text{RMSE} = \sqrt{\frac{\sum_{i=1}^n (I_i - R_i)^2}{n}}, \quad (4.2)$$

$$\text{MPE} = \frac{100\%}{n} \sum_{i=1}^n (I_i - R_i)/R_i, \quad (4.3)$$

where n is the number of measurements (here equal to four), I_i is the i^{th} sample by TriSonicaTM Mini, and R_i is the i^{th} reference measurement.

4.1.2 R.M. YOUNG 81000 Performance against Pitot Tube

This section describes the results of R.M. YOUNG 81000 measurements against the Pitot tube. For these tests data was sampled at 10 Hz by both sensors and time averaged for 5 min. Figure 4.2 shows the mean wind speed measured by R.M. YOUNG 81000 against the Pitot tube at different azimuth angles. The trend lines show that R. M. YOUNG 81000 performance is in good agreement with the Pitot tube and independent of the azimuthal angle.

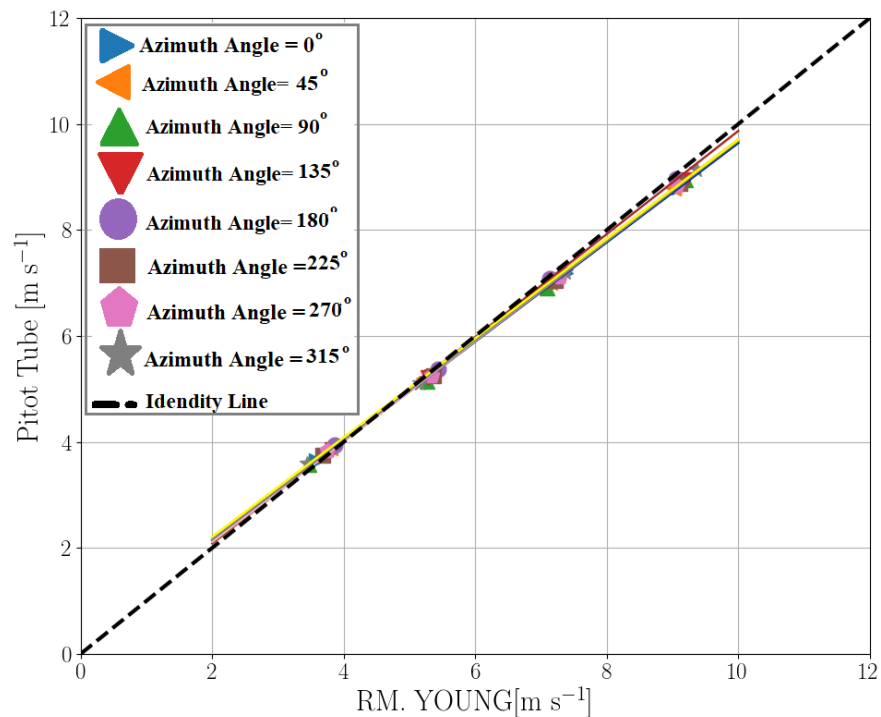


Figure 4.2: R.M. YOUNG 81000 performance in measuring mean wind speed against Pitot tube at different azimuth angles.

The quantitative comparison between R.M. YOUNG 8100 and Pitot tube is presented in Tables 4.2.

4.1.3 TriSonicaTM Mini Performance against R.M. YOUNG 81000

The results of TriSonicaTM Mini's performance in measuring turbulence statistics of the flow field against the R.M. YOUNG 81000 measurements are shown in this section. Figure 4.3 shows the TriSonicaTM Mini's performance in measuring U variance of the flow field versus

Error \ Azimuthal Angle	0°	45°	90°	135°	180°	225°	270°	315°
Bias [m s ⁻¹]	0.061	0.129	0.117	0.112	0.033	0.114	0.101	0.066
RMSE [m s ⁻¹]	0.137	0.185	0.176	0.158	0.069	0.161	0.160	0.161
MPE [%]	0.425	1.511	0.117	1.375	0.279	1.367	1.093	0.239

Table 4.2: Effects of the change in azimuthal angle on R.M. YOUNG 81000 performance in measuring mean wind speed calculated in terms of bias, RMSE, and MPE.

Error \ Variances	$\overline{u^2}$	$\overline{v^2}$	$\overline{w^2}$
Bias [m ² s ⁻²]	0.006	0.013	0.026
RMSE [m ² s ⁻²]	0.006	0.014	0.001

Table 4.3: Performance of TriSonicaTM Mini in measuring turbulence statistics of wind velocity component compared against R.M. YOUNG 81000 calculated in terms of bias and RMSE.

R.M. YOUNG 81000. According to the plot, TriSonicaTM Mini measures higher $\overline{u^2}$ with respect to R.M. YOUNG 81000.

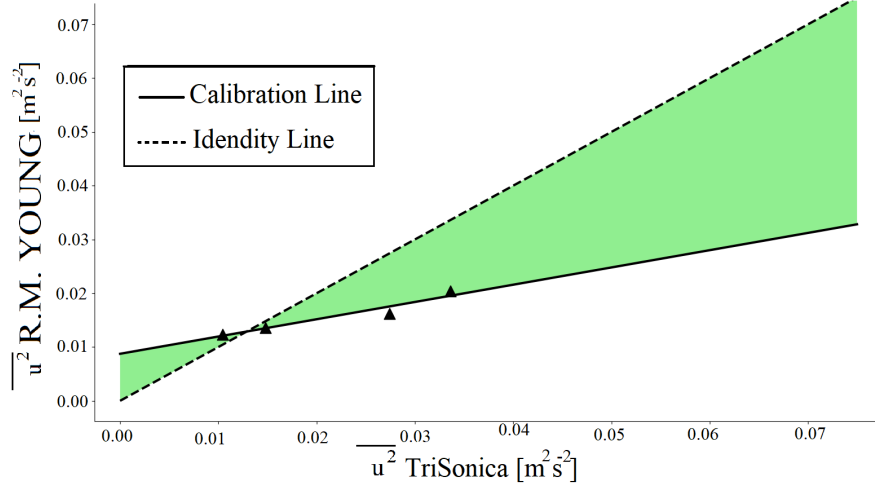


Figure 4.3: TriSonicaTM Mini's performance in measuring $\overline{u^2}$ against R.M. YOUNG 81000.

Figure 4.4 shows the TriSonicaTM Mini's performance in measuring V variance of the flow field versus R.M. YOUNG 81000. The trend shows that $\overline{v^2}$ is, too, overestimated by TriSonicaTM Mini.

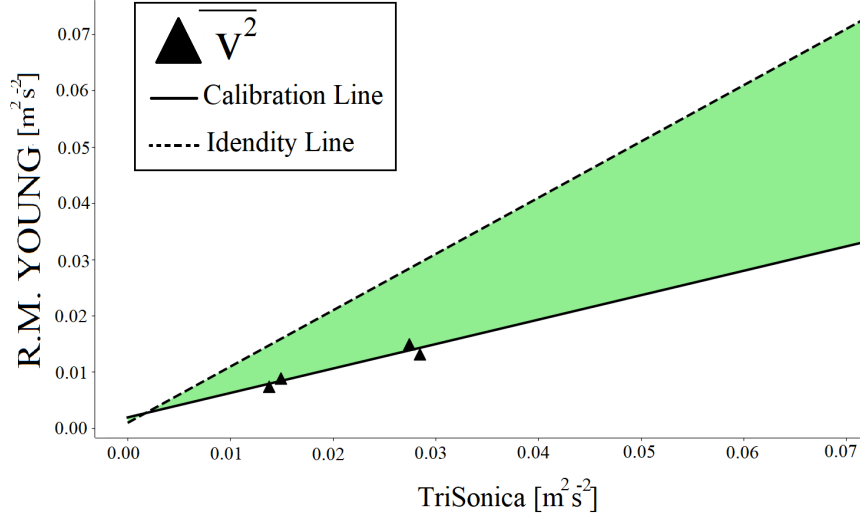


Figure 4.4: TriSonicaTM Mini’s performance in measuring $\overline{v^2}$ against R.M. YOUNG 81000.

4.1.4 TriSonicaTM Mini Performance when Mounted on Gondola

For these tests data was sampled at 10 Hz by all sensors and time averaged for 5 min. Figure 4.5 shows the effect of the gondola on TriSonicaTM Mini’s performance in measuring the \overline{U} and \overline{V} components of the flow field in the wind tunnel. According to Fig. 4.5 the presence of gondola leads to an over estimation in both \overline{U} and \overline{V} components of wind velocity. For reference, the measurements without the gondola are also shown in this plot for comparison.

Azimuth Angle	0°	45°	90°	135°
Error				
Bias [m s ⁻¹]	1.293	0.540	0.455	-0.017
RMSE [m s ⁻¹]	1.461	0.621	0.485	0.350

Table 4.4: Effects of the change in azimuthal angle on mounted TriSonicaTM Mini performance in measuring mean wind speed calculated in terms of bias and RMSE.

The calibration is further continued to determine the gondola’s effect on measuring the turbulence statistics of a flow field against the R.M. YOUNG 81000. Figure 4.6 compares the $\overline{u^2}$ measured by TriSonicaTM Mini both when mounted and unmounted on the gondola against the R.M. YOUNG 81000. The graph shows that the platform adds fluctuations, hence, it further increases the $\overline{u^2}$. The coloured areas show the deviation from the identity line. The blue coloured area shows the gondola’s deviation while the grey one corresponds to the TriSonicaTM Mini. Comparing the area coverage of these coloured areas, the gondola

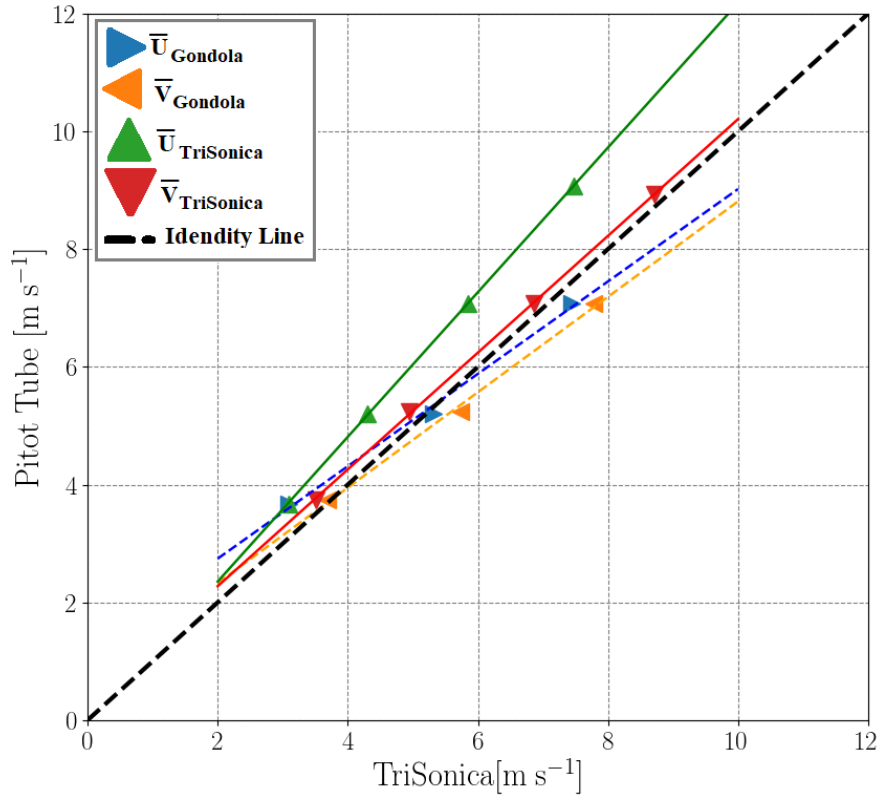


Figure 4.5: TriSonicaTM Mini's performance in measuring \bar{U} and \bar{V} against Pitot tube when mounted on gondola.

Variances		$\overline{u^2}$
Error		
Bias [m ² s ⁻²]		0.642
RMSE [m ² s ⁻²]		0.688

Table 4.5: Performance of mounted TriSonicaTM Mini in measuring turbulence statistics of wind velocity component compared against R.M. YOUNG 81000 calculated in terms of bias and RMSE.

shows higher deviation.

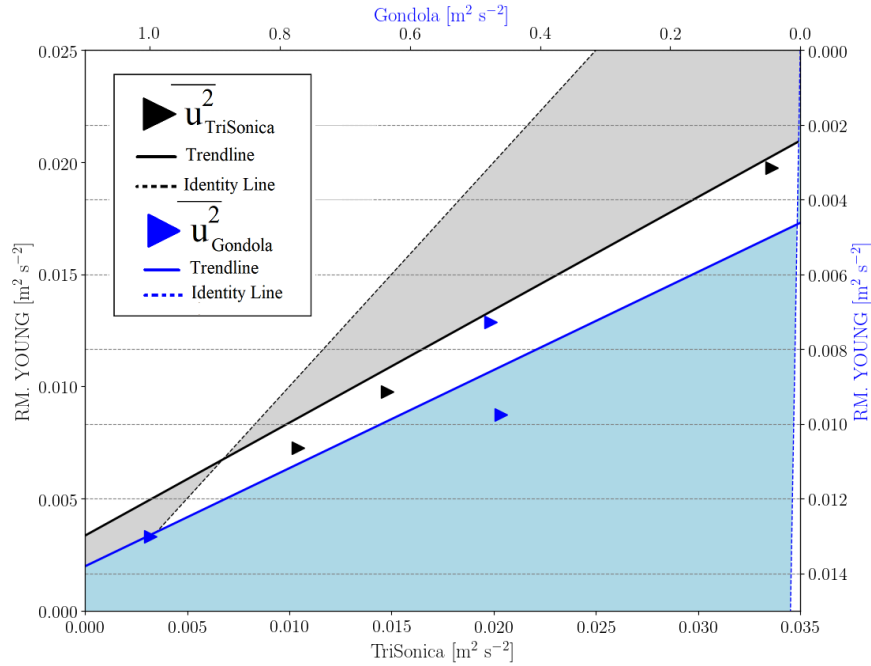


Figure 4.6: TriSonicaTM Mini’s performance in measuring $\overline{u^2}$ against R.M. YOUNG 81000 when unmounted and mounted on gondola.

Overall the TriSonicaTM Mini has shown errors in measuring mean wind velocity components and turbulence statistics in comparison to the reference measurements. These errors are larger than those reported by the manufacturer.

4.1.5 Calibration Factors

The calibration equations, polynomials to relate the raw sensor output to a reference measurement (Pitot tube or R.M. YOUNG 81000) for both the TriSonicaTM Mini and gondola

(when the sensor is mounted on the platform) are derived from the plots presented previously. The first order polynomial is used in this study that can be defined as $Y = aX + b$ where a and b are the calibration coefficients. X is defined as either the TriSonicaTM Mini or the gondola measurement while Y refers to the equivalent Pitot tube or R.M. YOUNG 81000 measurement. Tables 4.6 and 4.7 summarize the calibration factors.

Table 4.6: TriSonicaTM Mini’s calibration factors for mean velocity measurements.

Calibrated Var. → Reference Var. ↓	TriSonica TM Mini	
	a	b
$\bar{U}_{PitotTube}$	$U_{TriSonica}$	
	1.228	-0.103
$\bar{V}_{PitotTube}$	$V_{TriSonica}$	
	1.182	+0.134
$\bar{U}_{PitotTube}$	$\bar{U}_{TriSonica}$ at 40°	
	9.985	+0.054
$\bar{U}_{PitotTube}$	$\bar{U}_{TriSonica}$ at 30°	
	4.535	-0.091
$\bar{U}_{PitotTube}$	$\bar{U}_{TriSonica}$ at 20°	
	2.120	+0.110

Table 4.7: TriSonicaTM Mini’s calibration factors for turbulence statistics measurements.

Calibrated Var. → Reference Var. ↓	TriSonica TM Mini	
	a	b
$\overline{u^2}_{R.M.YOUNG}$	$\overline{u^2}_{TriSonica}$	
	1.229	-0.103
$\overline{v^2}_{R.M.YOUNG}$	$\overline{v^2}_{TriSonica}$	
	1.181	+0.134

For the mounted TriSonicaTM Mini, the calibration factors are derived based on the wind tunnel experiment that mimic field conditions as much as possible. Tables 4.8 and 4.9 summarize the results. The first set of factors consider the change in the azimuth angle and the corresponding calibration for the mean horizontal wind speed. The next set of factors corresponds to the individual velocity vector variances.

Overall the TriSonicaTM Mini has shown errors in measuring mean wind velocity components and turbulence statistics in comparison to the reference measurements. These errors

Table 4.8: TriSonica™ Mini’s calibration factors when mounted on gondola for mean velocity measurements.

Calibrated Var. → Reference Var. ↓	TriSonica™ Mini	
	a	b
$\bar{U}_{PitotTube}$	$\bar{U}_{Gondola(0^\circ)}$ 0.677	+0.847
$\bar{U}_{PitotTube}$	$\bar{U}_{Gondola(45^\circ)}$ 0.823	+0.475
$\bar{U}_{PitotTube}$	$\bar{U}_{Gondola(90^\circ)}$ 1.111	-1.088
$\bar{U}_{PitotTube}$	$\bar{U}_{Gondola(135^\circ)}$ 1.295	-1.480
$\bar{U}_{PitotTube}$	$\bar{U}_{Gondola(180^\circ)}$ 0.610	+0.934

Table 4.9: TriSonica™ Mini’s calibration factors when mounted on gondola for turbulence statistics measurements.

Calibrated Var. → Reference Var. ↓	TriSonica™ Mini	
	a	b
$\overline{u^2}_{R.M.YOUNG}$	$\overline{u^2}_{Gondola}$ 0.008	+0.004
$\overline{v^2}_{R.M.YOUNG}$	$\overline{v^2}_{Gondola}$ 0.017	+0.003

are larger than those reported by the manufacturer. Even though this rigorous calibration exercise attempts to reduce the errors in the measurement, the TriSonica™ Mini should be redesigned by the manufacturer to show better performance against industry standard sensors. In addition, the calibrations are limited because they only correct for wind measurements against wind tunnel conditions. The sensor should be further tested in real atmospheric conditions against other reference instruments.

4.1.6 TANAB Field Observation

The TANAB system was successfully tested in May 2018 in northern Canada at a mining facility. A series of 56 flight hours were conducted to capture the diurnal and nocturnal properties of the ABL. Each balloon launch lasted approximately 15 to 30 minutes while the tether was carefully controlled to obtain a profile with constant ascend and descent rates. In addition, several tests were dedicated to resolve the ABL's transition in the sunrise and sunset. This section highlights a few observations, while the full set of results are presented by Nambiar et al. [54]. In this analysis, all 56 flight hours were combined and the data are statistically sampled based on diurnal time or altitude to be able to report meaningful statistics. It is noted that the author of this thesis developed the post processing codes with the help of Manoj K. Nambiar and Amir A. Aliabadi.

The horizontal wind speed and turbulence kinetic energy follow the same diurnal trend as they increase in the mid-afternoon resembling a gusty condition followed by a calm condition in the night and the early morning hours when the atmosphere is thermally stable. Figures 4.7 and 4.8 show the diurnal change of the horizontal wind speed and turbulence kinetic energy, respectively. When calculating hourly statistical percentiles, the data is combined over all altitudes and aggregated for all the launches in multiple days.

The other turbulence statistics including the along-wind and cross-wind vertical momentum fluxes, \overline{uw} and \overline{vw} , respectively, turbulent kinematic vertical heat flux $\overline{\theta w}$, potential temperature variance $\overline{\theta^2}$, and the vertical velocity variances $\overline{w^2}$, too, exhibit diurnal variations as presented in Fig. 4.9. Analyzing the fluxes of heat and momentum shows that the system successfully measures the transition from thermally stable to a convective ABL qualitatively. During late afternoon hours around 1600 and 1700 Local Daylight Time (LDT) the flux of momentum reaches its peak negative value, while the heat flux is at its peak positive value.

Figure 4.10 shows the profile of turbulence statistics for different diurnal periods (4-hr

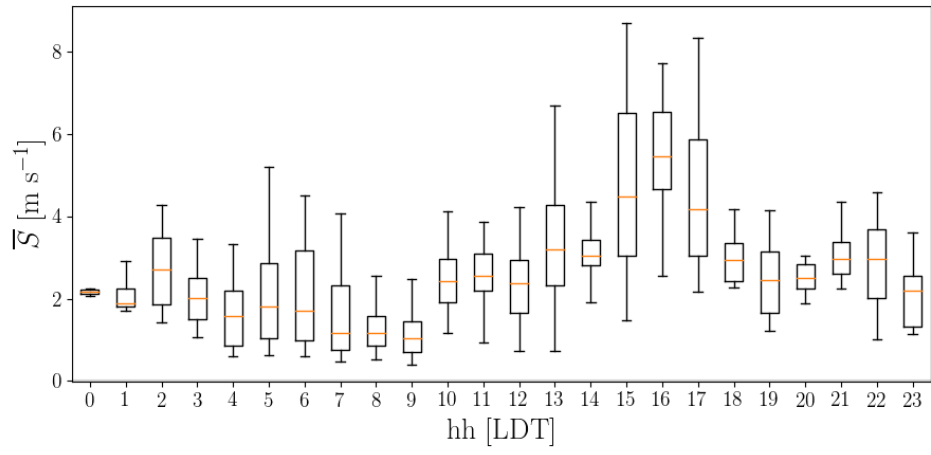


Figure 4.7: Diurnal variation of the horizontal wind speed; figures extracted from [54].

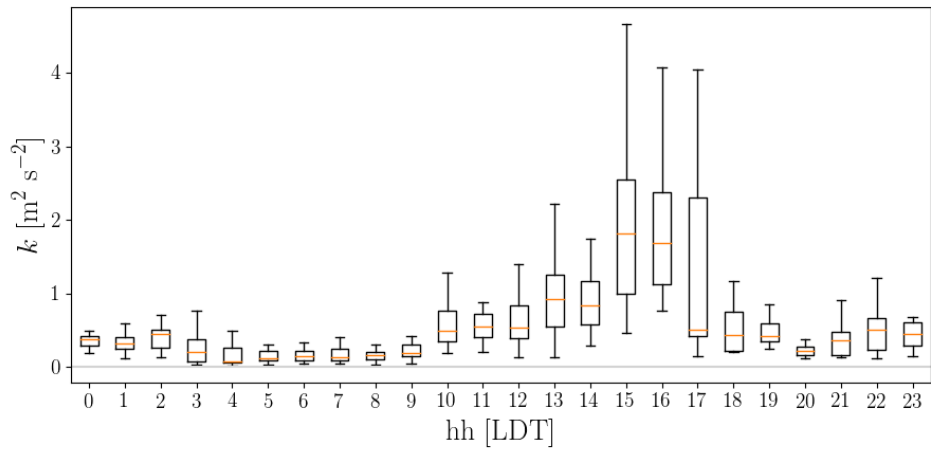
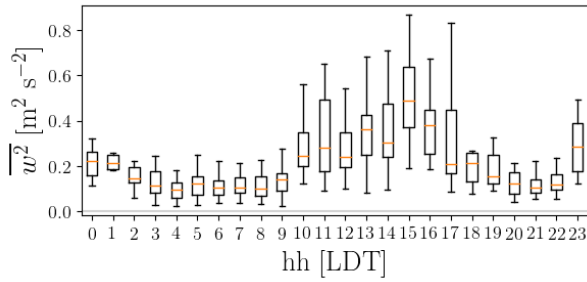
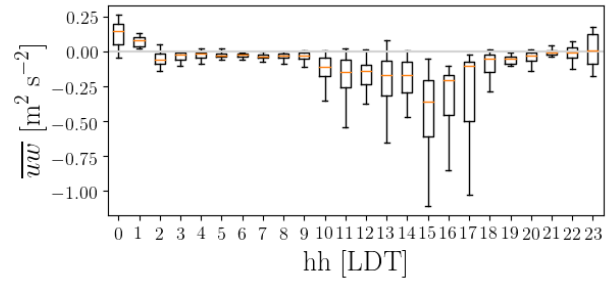


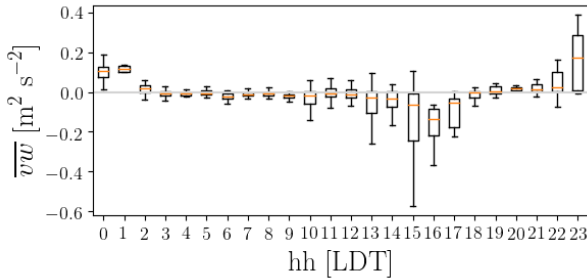
Figure 4.8: Diurnal variation of the turbulence kinetic energy; figures extracted from [54].



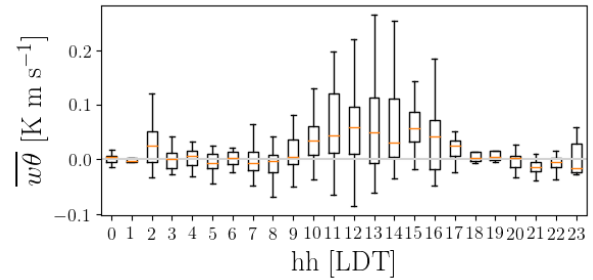
(a) Variance of vertical wind velocity



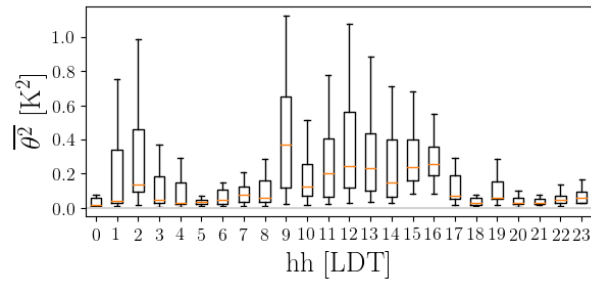
(b) Momentum flux in x direction



(c) Momentum flux in y direction



(d) Vertical sensible kinematic heat flux



(e) Variance of potential temperature

Figure 4.9: Diurnal variation of turbulence statistics; figures extracted from [54]

time intervals) of the day. Medians are shown for all observations. Data is binned in 20-m height intervals. The vertical structure of the atmosphere near the surface can be understood while analyzing the turbulence kinetic energy k , along-wind and cross-wind vertical momentum fluxes, \overline{uw} and \overline{vw} , respectively, sensible kinematic vertical heat flux $\overline{w\theta}$, variance of potential temperature $\overline{\theta^2}$, and variance of vertical wind velocity $\overline{w^2}$. Analyzing the profile of the momentum flux shows that the system successfully observes the thermal stability and instability of the ABL qualitatively.

4.1.7 Part 1: Conclusions

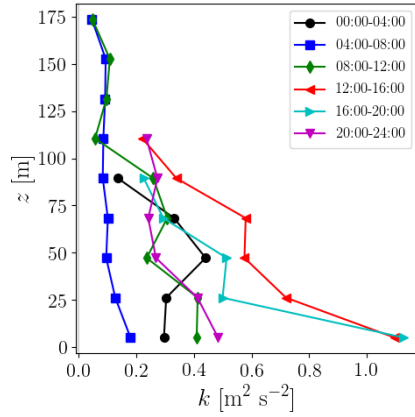
The results of the wind tunnel calibration tests shows that TriSonicaTM Mini's performance depends on the azimuth angles. The measurements show deviations from the Pitot tube and R.M. YOUNG 81000 measurements significantly. The effect of the mounted platform (gondola) on the TriSonicaTM Mini measurements are also important.

TriSonicaTM Mini shows an inconsistent behaviour in face of different azimuthal angles. The bias ranges from -1.080 m s^{-1} to 0.138 m s^{-1} when the azimuth angle varies from 0° to 270° . R.M. YOUNG 81000 shows relatively consistent measurements with respect to Pitot tube at different elevation and azimuthal angles. The bias varies from 0.033 m s^{-1} to 0.129 m s^{-1} for different azimuth angles.

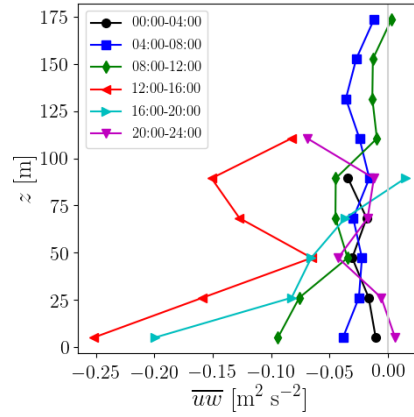
These tests resulted in calibration factors that were further used in measurements during the field observation. The system was successfully deployed in northern Canada in May 2018 measuring meteorological conditions over the open-pit mining facility. The measurements show that the system captures the expected changes of ABL variables as a function of diurnal time and height.

4.2 Part 2: Mesoscale Meteorological Modelling

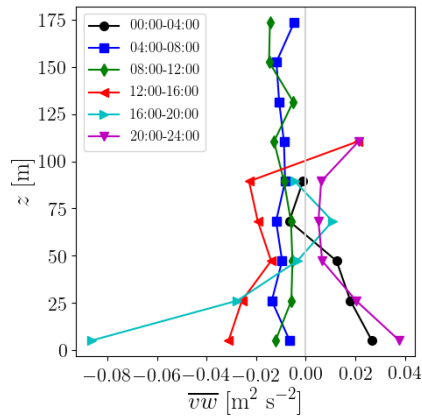
The author ran the UEMS model for May 18, 24, and 30, 2018. The model was spun up for 12 hours and then run for an additional 24 hours for each day. The horizontal grid resolutions used are given in Table 3.2 while 90 vertical levels were used. The non-local Yonsei University (YSU) PBL scheme was used. In this study, selected model outputs presented that show whether the WRF model is sensitive to local changes in topography and land use, while complementary results are reported by Nahian et al. [53], where full comparisons of the model against meteorological observations are made.



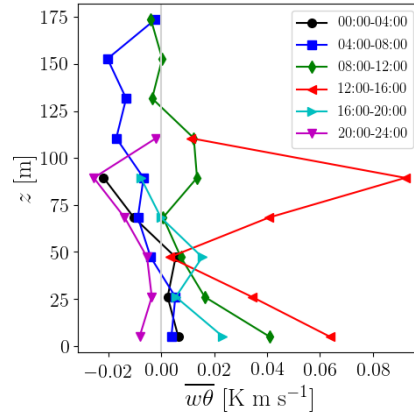
(a) Turbulence kinetic energy



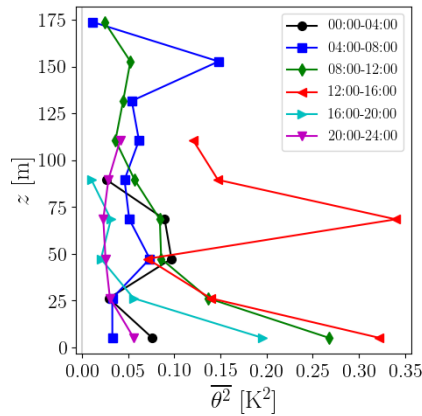
(b) Vertical momentum flux



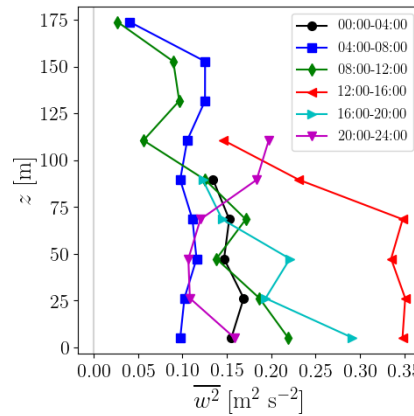
(c) Vertical momentum flux



(d) Vertical sensible kinematic heat flux



(e) Variance of potential temperature



(f) Variance of vertical wind velocity

Figure 4.10: Profiles of turbulence statistics at 4-hr time intervals; figures extracted from [54].

4.2.1 Lake Model Analysis

The open-pit mine requires a large pond to discharge the wastes from the industrial process and a series of water reservoirs across the facility. The temperature gradient between these bodies of water and the surrounding land surfaces affects the local meteorology that needs to be considered. The thermal condition of the tailings pond (lake) in the mining facility was studied at different diurnal times in detail along a cross section that splits the pond north-south. Figure 4.11 shows the location of the cross section.

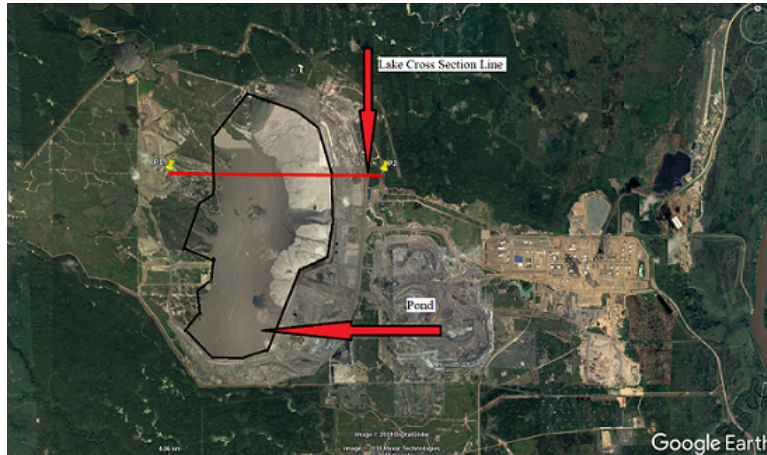


Figure 4.11: The cross section of the tailings pond used to study the contours of lake temperature.

Figure 4.12 shows the temperature distribution of the pond cross section at different diurnal times. The results show a highly thermally stratified structure at all times. The results show that the horizontal homogeneity of the temperature starts breaking at around 1500 Local Standard Time (LST). The instabilities are triggered by the first layer that directly interacts with the atmosphere (see Fig. 4.13). The instability is followed by an increase in lake surface temperature (about 4-5 K in the simulation period) at around 1500 LST. The temperature remains constant and unchanged for most of the bottom layers, while most of the temperature variations occur in the first few layers. It is worth mentioning that the simulation period occurred in late May 2018 when the relatively warm weather dominated the region, hence, the effect of the lake ice was not present in this study. Certainly, more considerations should be taken into account when applying this model in the cold season.

The results also show a very modest horizontal gradient of the temperature in the lake. Since the lake model is one-dimensional, this horizontal gradient can be explained by horizontal variation of boundary conditions at the lake surface, which is exposed to different

atmospheric conditions at different locations. This instability could be shown at the 3 dimensional plots of the lake temperature shown in Fig. 4.13. It is important to note that presence of a body of water affects the temperature gradients between the lake and surroundings that eventually can alter the local meteorology. This includes local changes in albedo, roughness length, surface emissivity, wind speed, wind direction, and surface temperature which will be described in the next sections.

4.2.2 Albedo

Albedo, a non-dimensional number representing how well a surface reflects shortwave radiation, is an important surface property that determines the energy balance at the earth surface. It is analyzed during the simulation period to investigate the effect of modifying land use classification on this property. Albedo changes between 0 and 1 with 0 for a perfect absorber and 1 for a perfect reflector of shortwave radiation. Figure 4.14 shows the contours of albedo over the inner domain at 0000 LST for three days of simulation. The results reflect the difference between albedos related to different land use classifications with lakes showing the lowest albedos. Studying the albedo over the inner domain shows that albedo changes during the simulation period, a behaviour that cannot be explained at the moment. The results further show that albedo changes inversely with the change in temperature. The first day with relatively higher temperature (by 2 K) experiences lower albedos over the grasslands although it remains unchanged for lakes.

4.2.3 Surface Emissivity

Emissivity, a non-dimensional number representing how well a surface exchanges longwave radiation, is an important surface property that determines the energy balance at the earth surface. It is analyzed during the simulation period to investigate the effect of modifying land use classification on this property. According to the Stephen-Boltzmann relationship, surface emissivity is equal to

$$e_{IR} = \frac{I \uparrow}{\sigma_{SB} \times T^4}, \quad (4.4)$$

where $I \uparrow$ represents the upward infrared radiation, σ_{SB} is the Stephen-Boltzmann constant ($= 5.67 \times 10^{-8} \text{ W m}^{-2} \text{ K}^{-4}$), and T is the absolute temperature in Kelvin. For most surfaces the emissivity changes between 0.9 and 0.99 [69].

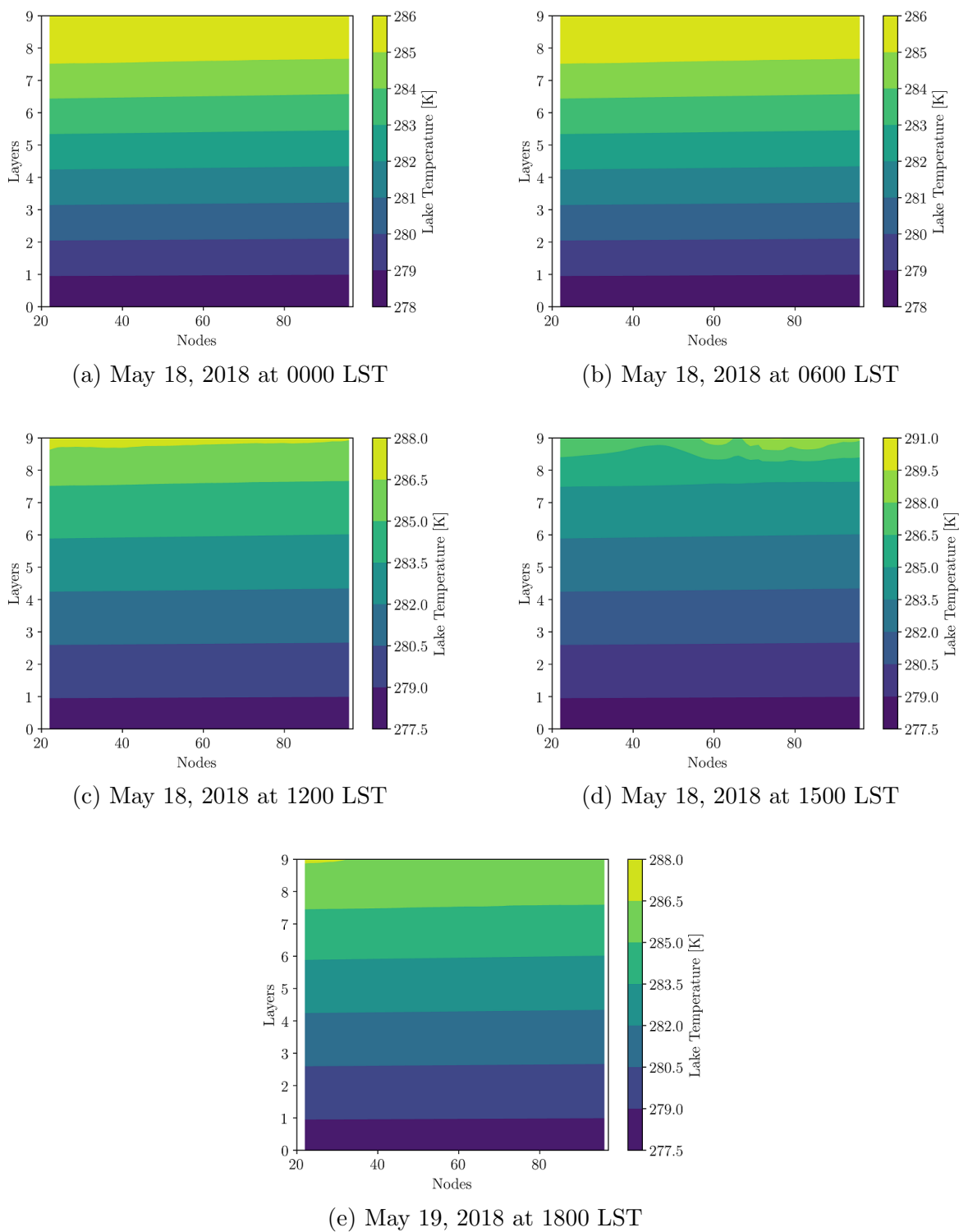


Figure 4.12: Contours of lake temperatures at different hours of a day on a cross section located at the middle of the pond; times in Local Standard Time (LST).

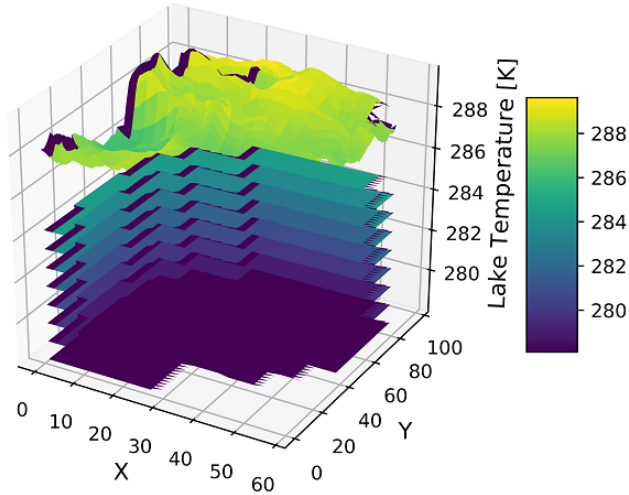


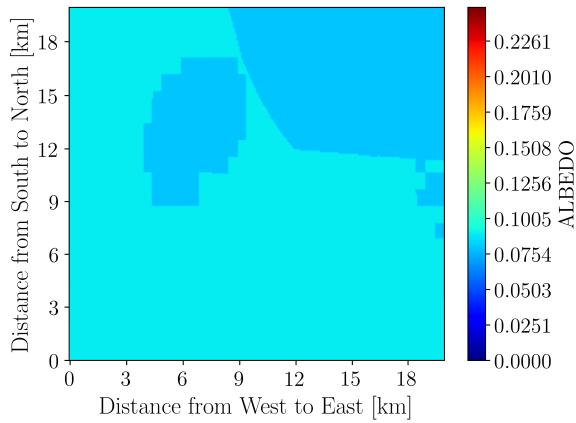
Figure 4.13: Temperature instability across the first lake layer; May 18, 2018 at 1500 LST.

Figure 4.15 shows the surface emissivity at 0600 LST over the simulation period. The emissivity is higher over the pond but drops to around 0.9 over the barren land. UEMS results of surface emissivity also demonstrate slight changes during the simulation periods, where the warmer days show less surface emissivity in the deciduous boreal forest, which is in accordance with Eq. 4.4.

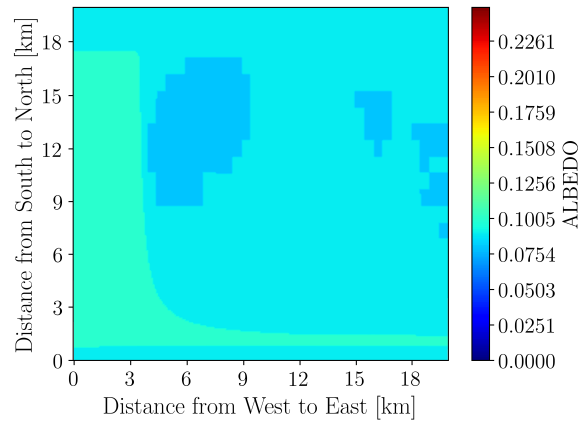
4.2.4 Roughness Length

Rough surfaces are likely to cause intense turbulence within the lower ABL, which increase the drag and turbulent transfer rates across the surface layer [68]. Surface roughness is an aerodynamic property of the earth, which is related to surface coverage, surrounding obstructions, and topographic relief [33]. Surface roughness can be best indexed by the aerodynamic roughness length scale, which is regarded as an empirical measure of retarding and disturbing effects that the surface has on near-ground winds [33]. Table 4.10 shows the Davenport classification of effective terrain roughness.

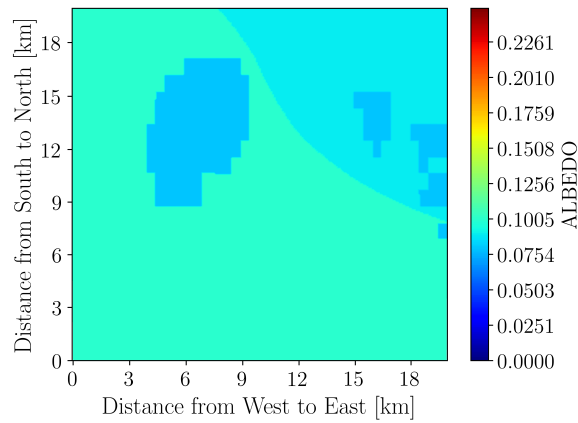
Figure 4.16 shows the background aerodynamic roughness lengthscale during the simulation period. Analyzing the roughness lengthscales from UEMS show that roughness lengthscale on the water bodies and barren areas is low, while it is higher in the boreal forest



(a) May 18, 2018 at 0000 LST

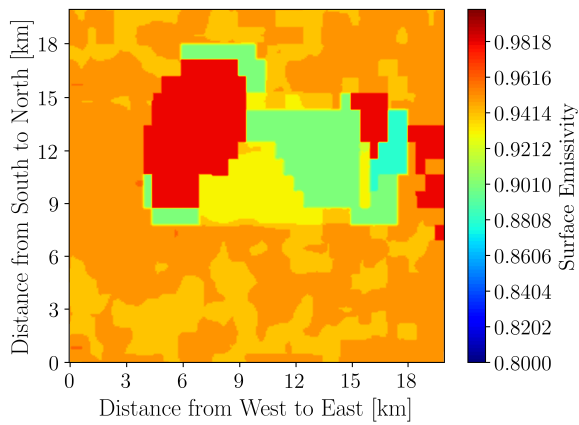


(b) May 24, 2018 at 0000 LST

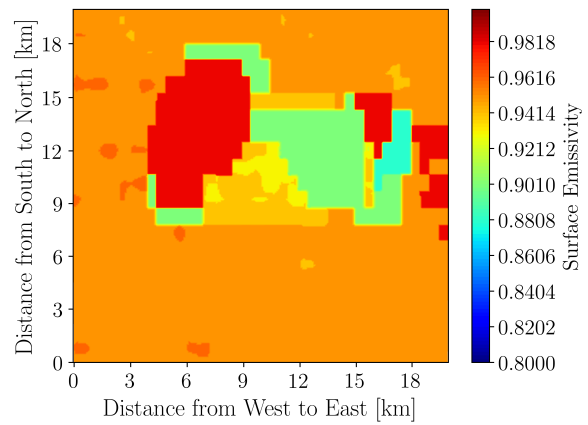


(c) May 30, 2018 at 0000 LST

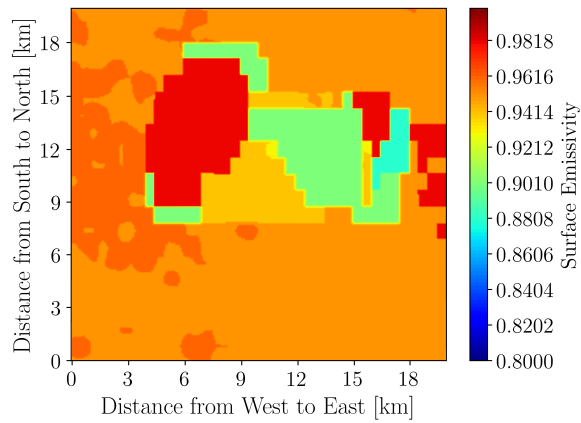
Figure 4.14: Contours of albedo over the inner domain during the simulation period; times in Local Standard Time (LST)



(a) May 18, 2018 at 0000 LST



(b) May 24, 2018 at 0000 LST



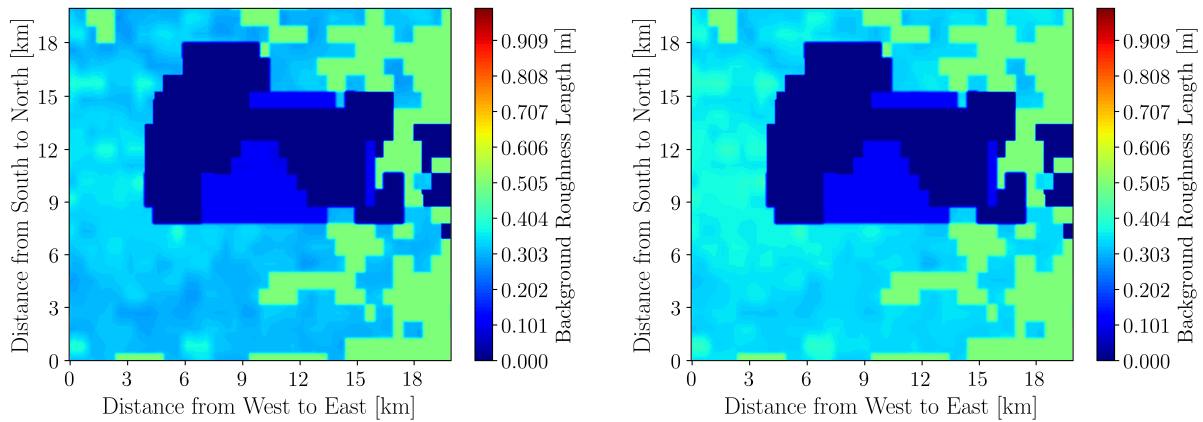
(c) May 30, 2018 at 0000 LST

Figure 4.15: Surface emissivity during the simulation period; times in Local Standard Time (LST).

Class	Landscape description	$z_0[m]$
1 Sea	Open sea or lake (irrespective of wave size), tidal flat, snow-covered flat plain, featureless desert, tarmac and concrete, with a free fetch of several kilometres	0.0002
2 Smooth	Featureless land surfaces without any noticeable obstacles and with negligible vegetation; e.g., beaches, pack ice without large ridges, marsh, and snow-covered or fallow open country.	0.005
3 Open	Level country with low vegetation (e.g., grass) and isolated obstacles with separations of at least 50 obstacle heights; e.g., grazing land without windbreaks, heather, moor and tundra, runway area of airport. Ice with ridges across-wind.	0.03
4 Roughly open	Cultivated or natural area with low crops or plant covers, or moderately open country with occasional obstacles (e.g., low hedges, isolated low buildings or trees) at relative horizontal distances of at least 20 obstacle heights.	0.1
5 Rough	Cultivated or natural area with high crops or crops of varying heights, and scattered obstacles at relative distances of 12 to 15 obstacle heights for porous objects (e.g., shelter belts) or 8 to 12 obstacle heights for low solid objects (e.g., buildings).	0.25
6 Very rough	Intensively cultivated landscape with many rather large obstacle groups (large farms, clumps of forest) separated by open spaces of about 8 obstacle heights. Low densely-planted major vegetation like bushland, orchards, young forest. Also, area moderately covered by low buildings with inter spaces of 3-7 building heights and no high trees .	0.5
7 Skimming	Landscape regularly covered with similar-size large obstacles, with open spaces of the same order of magnitude as obstacle height; e.g., mature regular forests, densely built-up area without much building height variation.	1.0
8 Chaotic	City centres with mixture of low-rise and high-rise buildings, or large forests of irregular height with many clearings (analysis by wind tunnel advised).	≥ 2

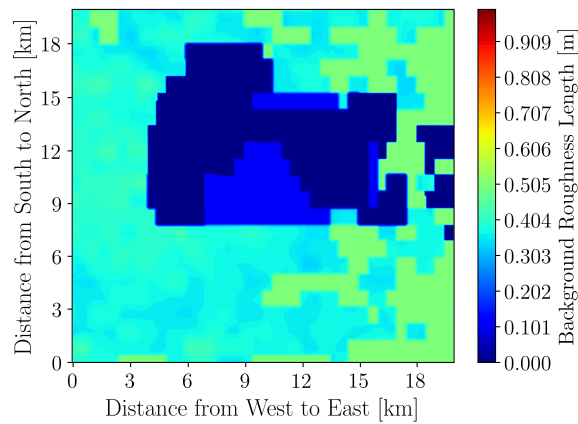
Table 4.10: Davenport classification of effective terrain aerodynamic roughness lengthscale; extracted from [33].

and developed areas of the mining facility. This variation indicates that modifying land use classification impacts the surface aerodynamic roughness lengthscale in the simulations. The results also show a slight change in roughness lengthscale during the simulation period with the slightly warmer day showing lower roughness length across the deciduous boreal forest while unchanged roughness length across lakes and barren lands. Diurnal variation of the roughness lengthscale cannot be explained by the author.



(a) May 18, 2018 at 1200 LST

(b) May 24, 2018 at 1200 LST



(c) May 30, 2018 at 1200 LST

Figure 4.16: Aerodynamic roughness lengthscale during the simulation period; times in Local Standard Time (LST).

4.2.5 The Effects of Updating the Topography and Land Use Classifications on Wind Vectors

In order to visualize the sensitivity of the model results to the change in topography and land use, vectors of wind velocity are plotted in Fig. 4.17 for both the default topography and the case with high resolution SRTM-LiDAR data and land use classification updated. The results demonstrate a notable difference in flow patterns as a result of changing topography and land use classification. Particularly, lower wind speeds and local circulation is predicted inside the mine-pit during night time. The model's forecasts of wind speed and wind direction in a convective atmosphere show less sensitivity to the local changes in terrain and land use. According to Fig. 4.18, the wind speed slightly slows down in the mine area while its magnitude and direction remains unchanged throughout the domain.

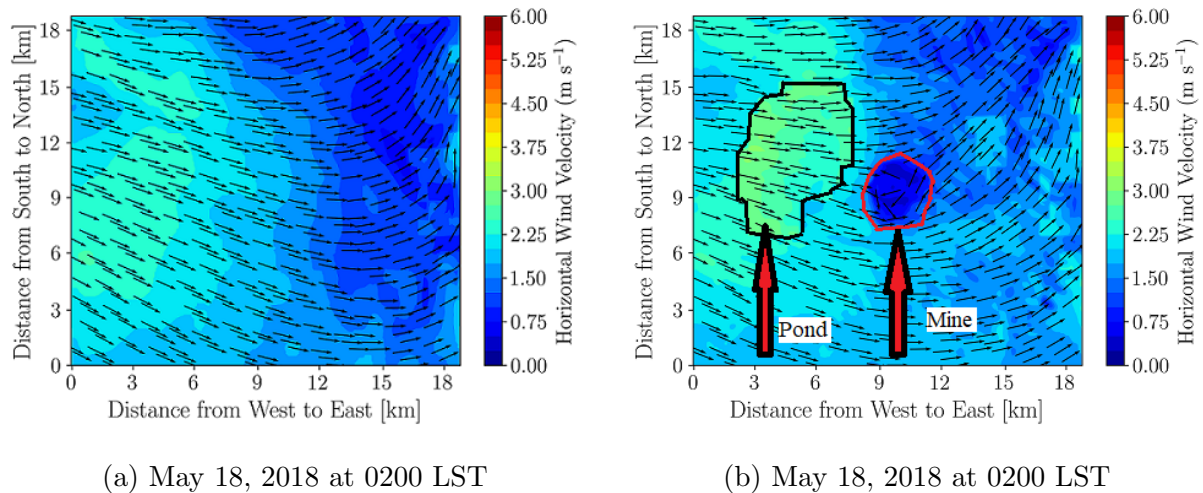


Figure 4.17: Effects of topography and land use classification changes on 10-m horizontal wind velocity magnitude and direction at 0200 LST; left: default topography and land use; right: modified topography and land use; figures are retrieved from [53].

4.2.6 The Effects of Updating the Topography and Land Use Classifications on Surface Potential Temperature at 2 m

Analyzing the contours of surface level potential temperature shows that the model's predictions in both the stable and convective atmosphere are sensitive to the change in terrain and land use data set. In general, adding the body of water tends to reduce the surface potential

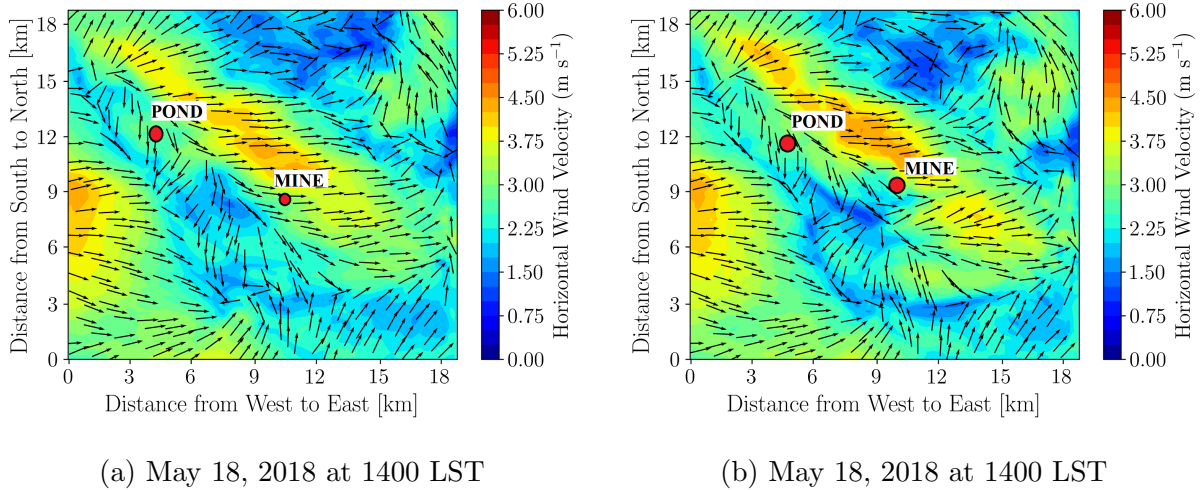


Figure 4.18: Effects of topography and land use classification changes on 10-m horizontal wind velocity magnitude and direction at 1400 LST; left: default topography and land use; right: modified topography and land use; figures are retrieved from [53].

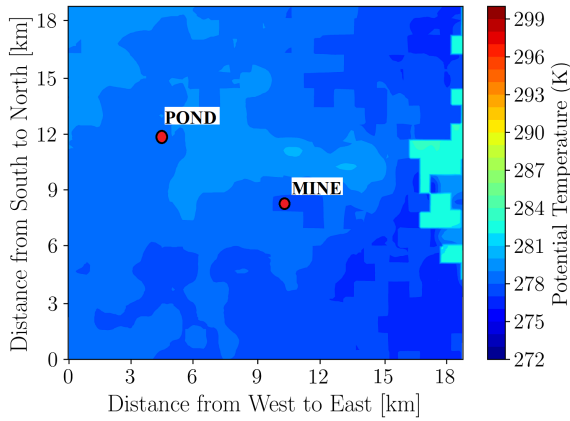
temperature during daytime and increase it during nighttime. Figures 4.19 and 4.20 show the contours of surface potential temperature corresponding to a stable and unstable atmosphere, respectively. Adaptation of the model with topography and land use has enhanced the accuracy of the results discussed in full detail by Nahian et al. [53].

4.2.7 The Effects of Updating the Topography and Land Use Classifications on Surface Relative Humidity at 2 m

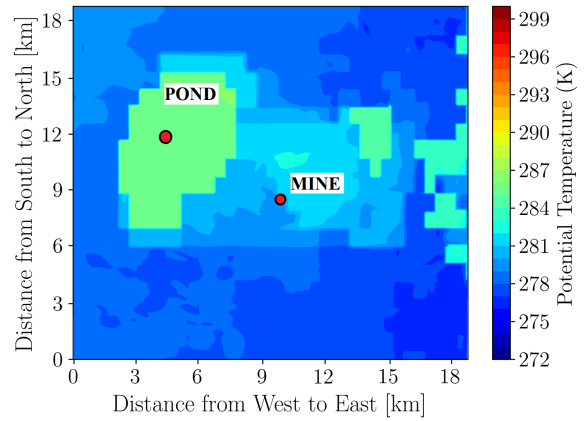
The effect of topography and land use modification on the WRF predictions of surface relative humidity is presented in Fig. 4.21 and Fig. 4.22. The implementation of the lake model and introducing the lake increases the surface level relative humidity in the area between the lake and the mine during the night. The surface level relative humidity increases over the pond during the day.

4.2.8 Model Comparison to Sounding Data

UEMS predictions are further compared to soundings profiles. Results are compared to radio soundings from Edmonton and Fort Smith. The largest domain of the simulation covers enough area to contain the sounding stations. The soundings record the horizontal

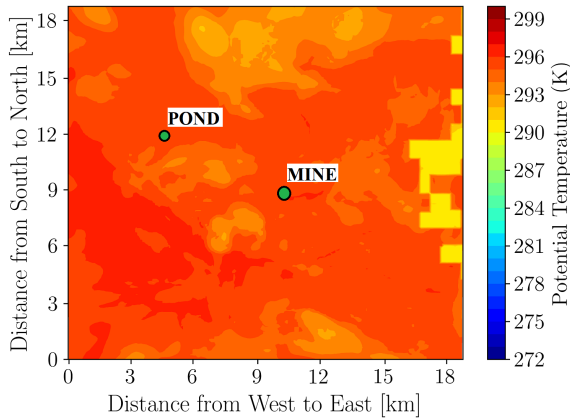


(a) May 18, 2018 at 0200 LST

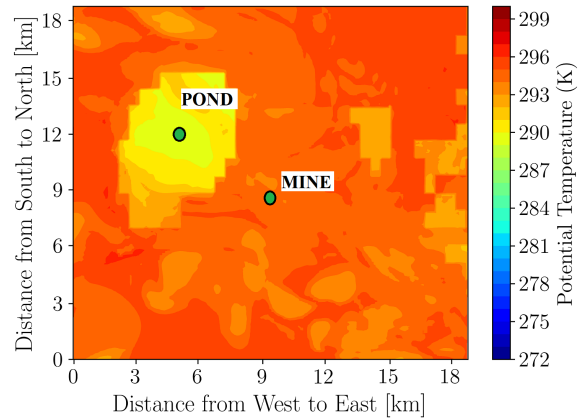


(b) May 18, 2018 at 0200 LST

Figure 4.19: Effects of topography and land use classification changes on surface potential temperature 2 m at 0200 LST; left: default topography and land use; right: modified topography and land use; figures are retrieved from [53].

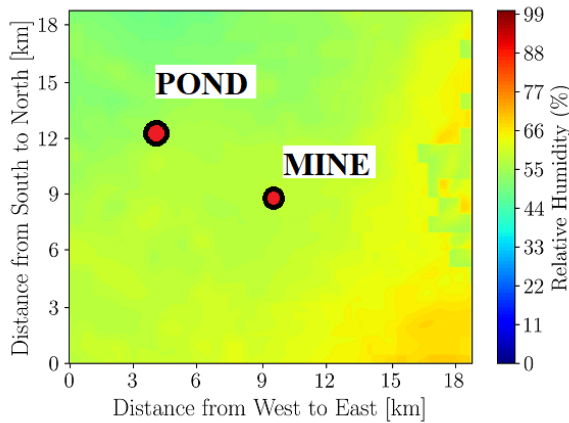


(a) May 18, 2018 at 1400 LST

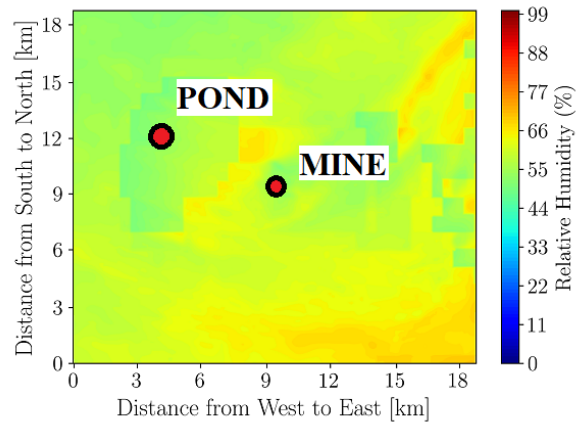


(b) May 18, 2018 at 1400 LST

Figure 4.20: Effects of topography and land use classification changes on surface potential temperature 2 m at 1400 LST; left: default topography and land use; right: modified topography and land use; figures are retrieved from [53].

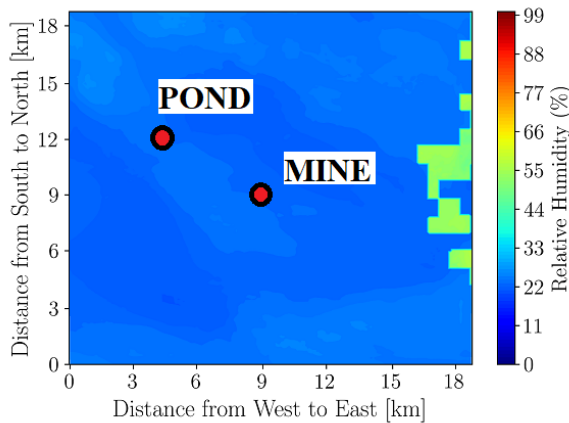


(a) May 18, 2018 at 0200 LST

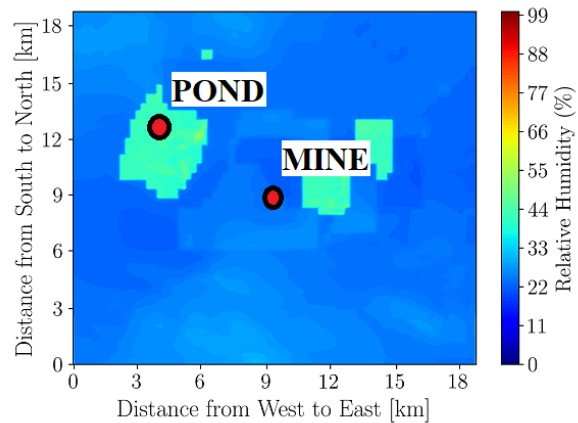


(b) May 18, 2018 at 0200 LST

Figure 4.21: Effects of topography and land use classification changes on surface relative humidity 2 m at 0200 LST; left: default topography and land use; right: modified topography and land use; figures are retrieved from [53].



(a) May 18, 2018 at 1400 LST



(b) May 18, 2018 at 1400 LST

Figure 4.22: Effects of topography and land use classification changes on surface relative humidity 2 m at 1400 LST; left: default topography and land use; right: modified topography and land use; figures are retrieved from [53].

wind speed, wind direction, water vapor mixing ratio, and potential temperature every 12 hours. Figure 4.23 indicates the location of the sounding stations.

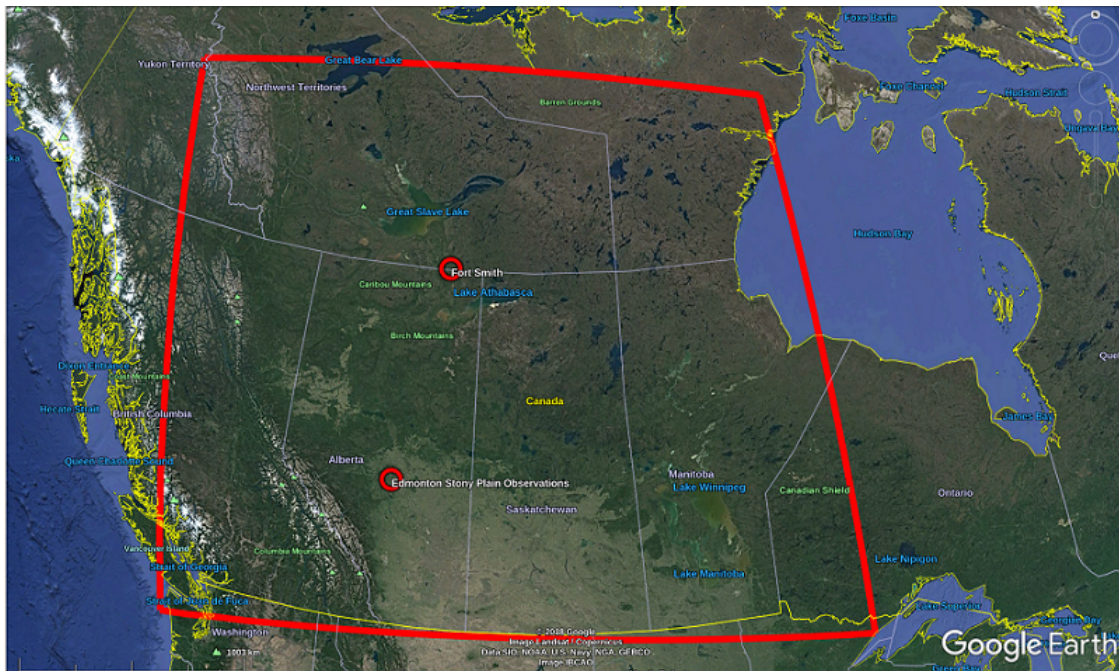
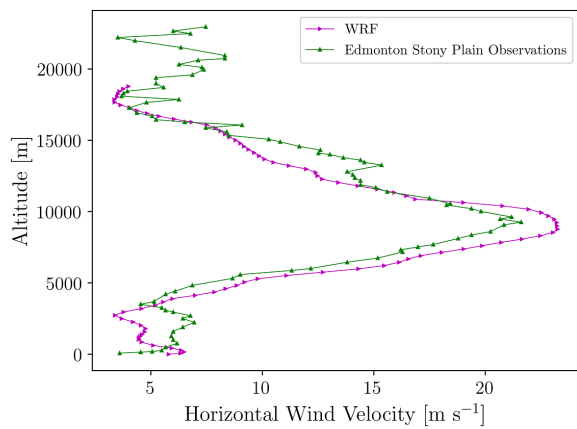


Figure 4.23: The location of sounding stations with respect to the largest model domain in UEMS.

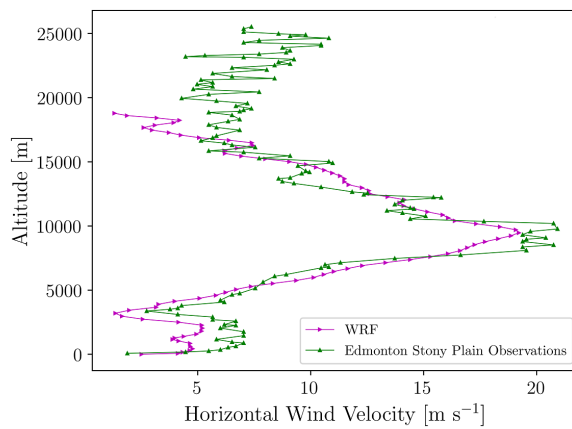
Vertical Profiles of Horizontal Wind Speed and Wind Direction

For the three simulation days, the model horizontal wind speed was averaged and compared to the three-day averaged sounding data at 00Z and 12Z. Figure 4.24 compares the UEMS results with the corresponding sounding data. UEMS predictions follow the sounding data trends at 00Z and 12Z. However, on average the UEMS underestimates the horizontal wind speed within the PBL at both times.

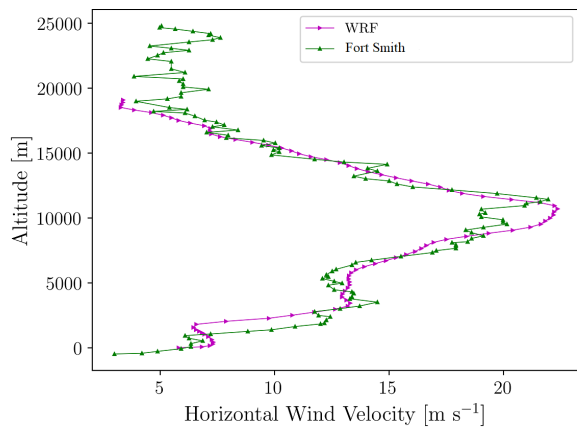
Wind direction on the other hand is compared on an hourly basis for each day rather than by averaging because wind direction is a circular variable. Figures 4.25 and 4.26 show the hourly wind direction comparison plots. The results show that UEMS predictions are in reasonable agreement with the observations.



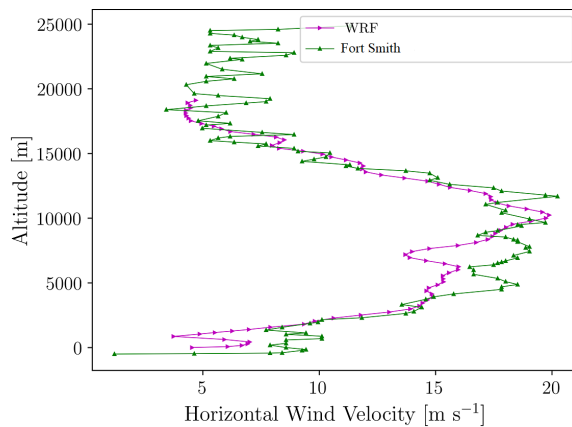
(a) May 18, 24, and 30 at 00Z



(b) May 18, 24, and 30 at 12Z

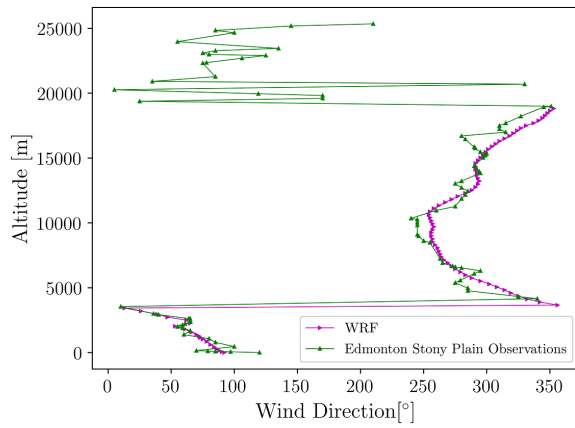


(c) May 18, 24, and 30 at 00Z

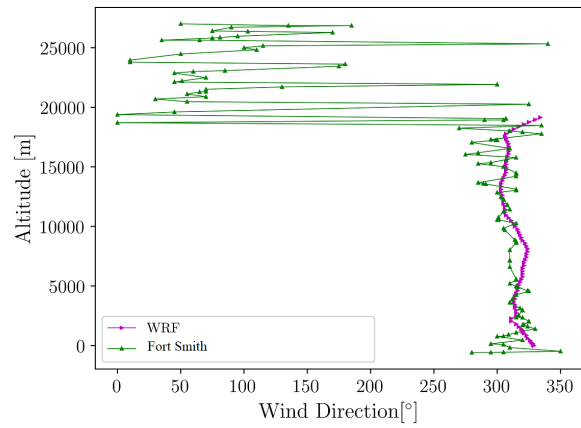


(d) May 18, 24, and 30 at 12Z

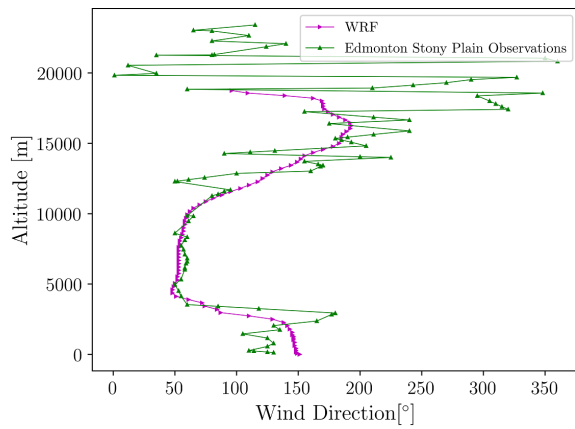
Figure 4.24: Horizontal wind speed for UEMS and sounding data averaged over three days.



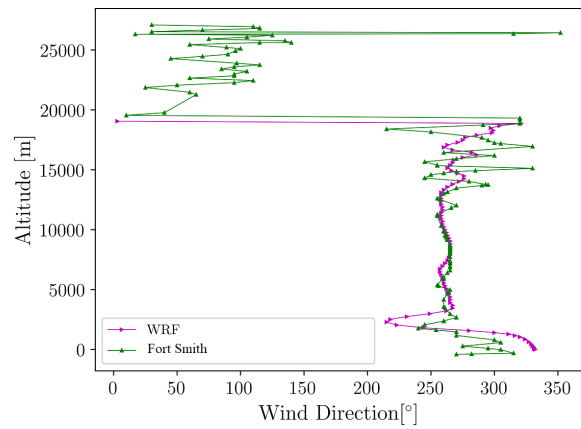
(a) May 18, 2018 at 00Z



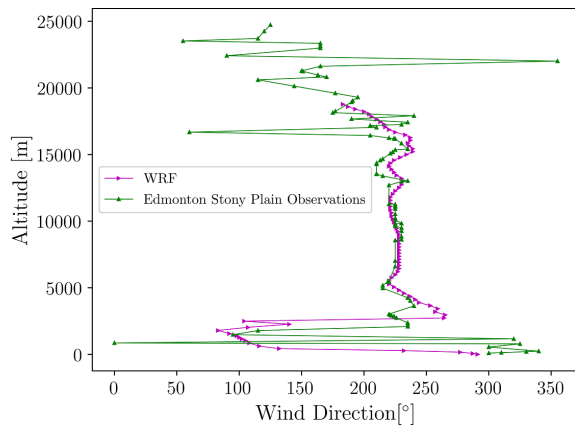
(b) May 18, 2018 at 00Z



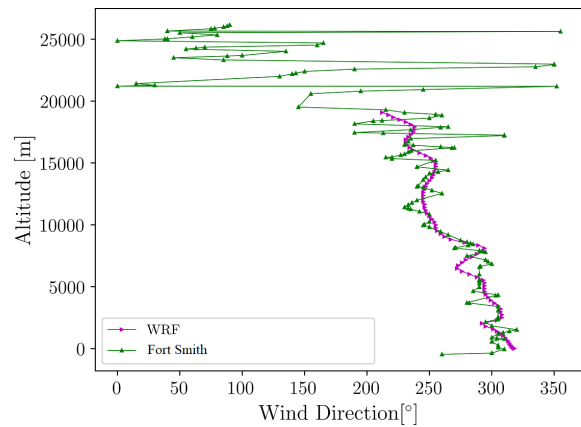
(c) May 24, 2018 at 00Z



(d) May 24, 2018 at 00Z

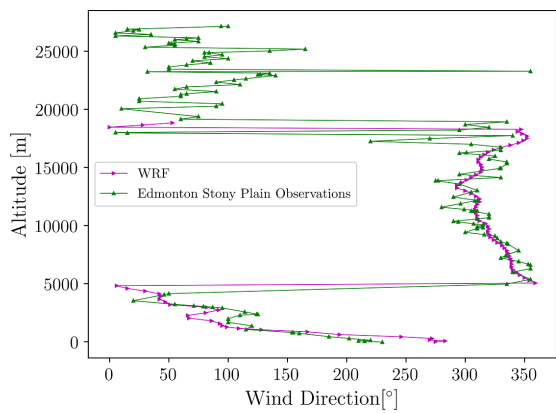


(e) May 30, 2018 at 00Z



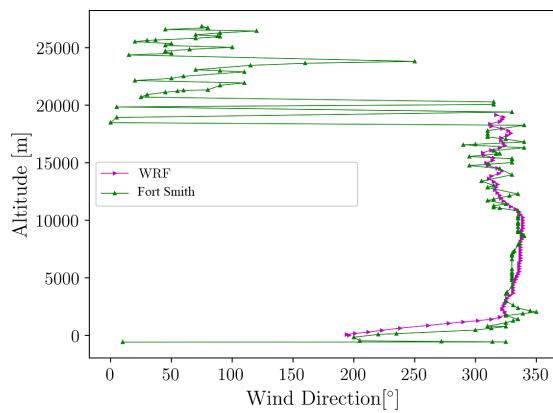
(f) May 30, 2018 at 00Z

Figure 4.25: Horizontal wind direction at 00Z; UEMS comparison against sounding data.

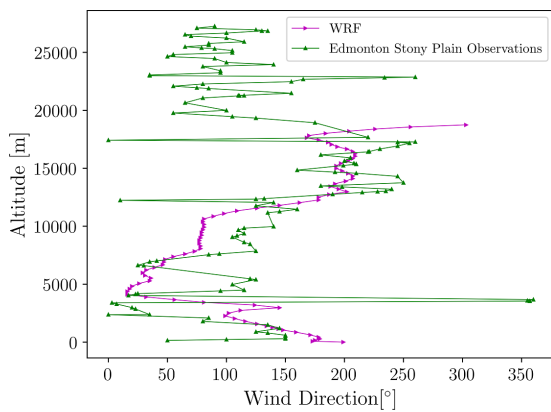


(a) May 18, 2018 at 12Z

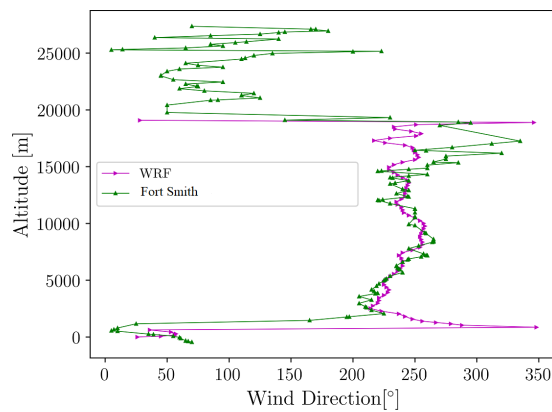
A



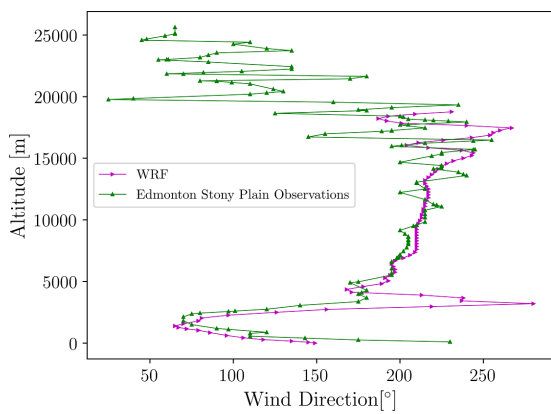
(b) May 18, 2018 at 12Z



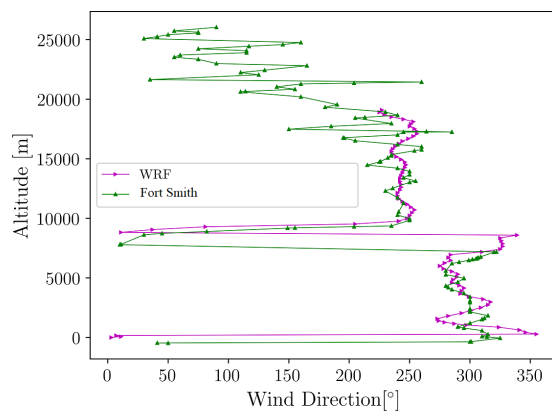
(c) May 24, 2018 at 12Z



(d) May 24, 2018 at 12Z



(e) May 30, 2018 at 12Z



(f) May 30, 2018 at 12Z

Figure 4.26: Horizontal wind direction at 12Z; UEMS comparison against sounding data.

Vertical Profiles of Water Vapor Mixing Ratio and Potential Temperature

One way of testing whether a mesoscale model produces enough vertical mixing in ABL is to compare the profiles of humidity and potential temperature against observations. This section compares the UEMS profiles of water vapor mixing ratio and the potential temperature with the corresponding sounding profiles. The data is averaged over three days and compared at 00Z and 12Z.

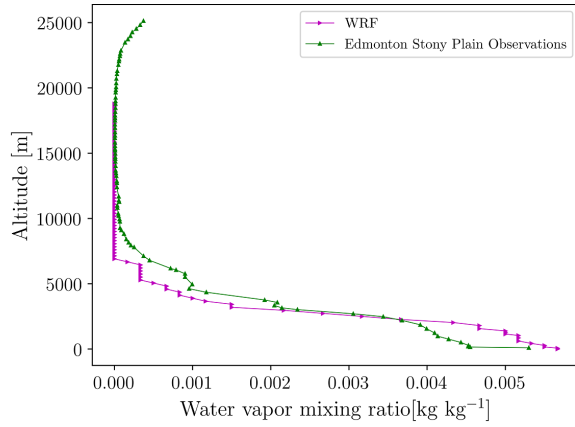
There is a reasonable agreement between the model results and the sounding data as shown in Figs. 4.27 and 4.28. On average, the results of the potential temperature show an underestimation compared to the soundings. The underestimation is greater at 12Z (0600 LST) than the 00Z (1800 LST), however, the water vapor mixing ratio does not follow any fixed pattern of deviation from observations. Overall, it can be concluded that vertical mixing in ABL is modelled reasonably over the simulation period and given the simulation configuration.

4.2.9 Model Comparison to TANAB Data

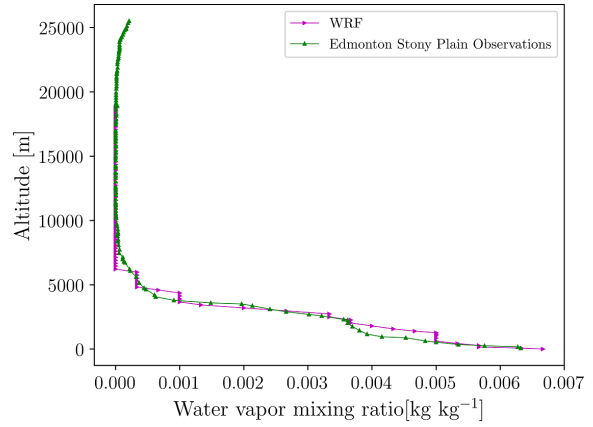
The measurements of TANAB are compared to UEMS predictions. For this purpose, wind speed measurements by TANAB are separated in different altitudes and hours and compared to UEMS predictions at the corresponding altitudes and times. Figure 4.29 shows the median wind speed for three days at each hour. The figure shows UEMS predictions associated with various options for topography and land use. The UEMS case with no account of topography and land use classification changes exhibits a bias of 0.98 m s^{-1} in wind speed with respect to measurements, while accounting for topography and land use classification changes reduces the bias to 0.60 m s^{-1} .

4.2.10 Part 2: Conclusions

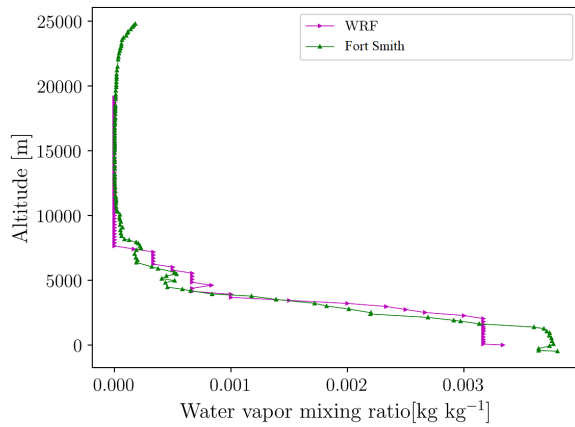
In this chapter, the Unified Environmental Modelling System (UEMS) predictions were analyzed to understand the effects of updating the terrestrial data on the results of the meteorological simulations over the open-pit mining facility. Land use classification changes affect the surface albedo, roughness length, and emissivity in the inner domain of simulation. The changes in topography also influence the flow patterns over the mining facility. In addition, a lake model was successfully implemented to simulate the thermodynamics of the pond. The structure of the water temperature in the pond was studied in detail to reveal the spatial



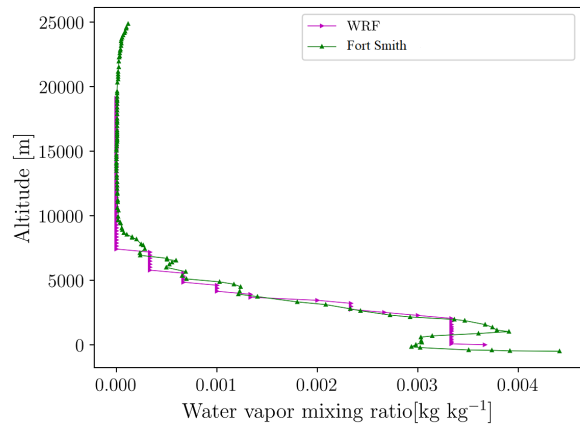
(a) May 18, 24, and 30 at 00Z.



(b) May 18, 24, and 30 at 12Z.

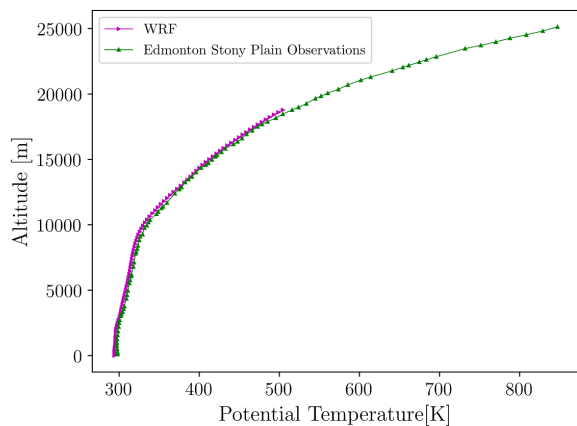


(c) A May 18, 24, and 30 at 00Z.

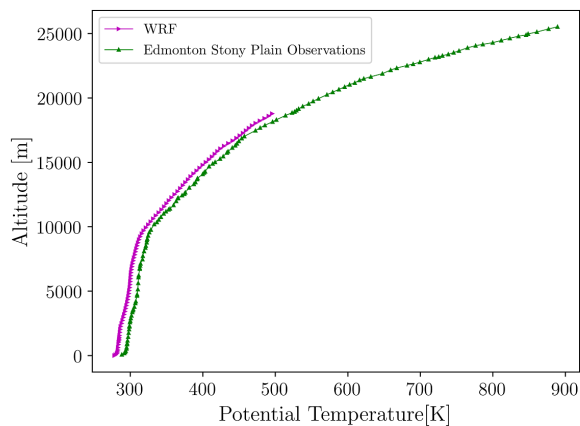


(d) May 18, 24, and 30 at 12Z.

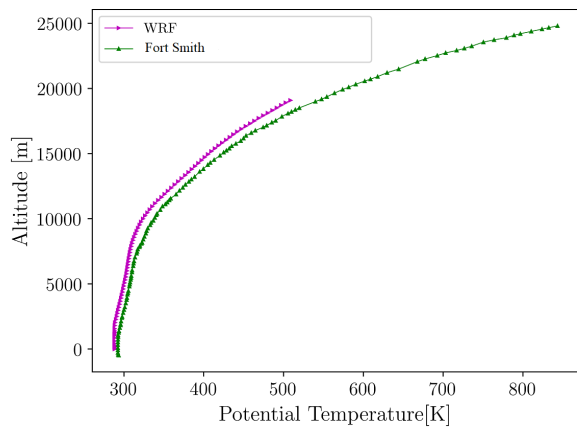
Figure 4.27: Water vapor mixing ratio for UEMS and sounding data averaged over three days.



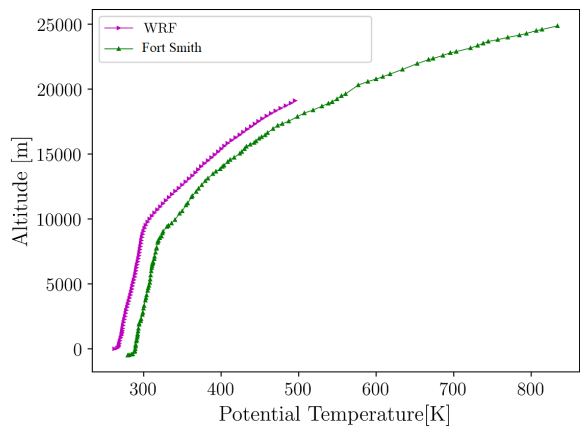
(a) May 18, 24, and 30 at 00Z



(b) May 18, 24, and 30 at 12Z



(c) May 18, 24, and 30 at 00Z



(d) May 18, 24, and 30 at 12Z

Figure 4.28: Potential temperature for UEMS and sounding data averaged over three days.

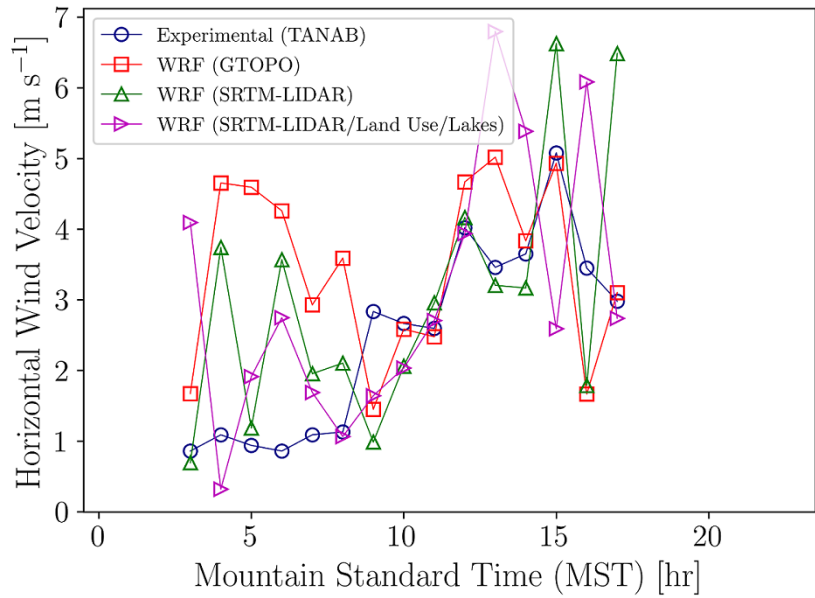


Figure 4.29: Wind speed comparison of UEMS predictions and TANAB measurements; figure extracted from [53].

and temporal variations of temperature in the pond.

The UEMS model outputs were compared to sounding profiles and the TANAB measurements. Profiles of wind direction and the horizontal wind speed show reasonable agreement with the result of the soundings. Profiles of water vapor mixing ratio and potential temperature, too, show reasonable agreement with sounding data. Comparison of wind speed measurements by TANAB and UEMS predictions shows that modifying topography and land use classification based on the most recent activities at the mining site results in more accurate simulations with reduced errors.

Chapter 5

Conclusions and Further Work

This thesis developed two novel methodologies for investigation of the meteorological properties of Atmospheric Boundary Layer (ABL) over an open-pit mining facility in northern Canada. The first approach was development of a meteorological sensing platform based on ultrasonic anemometry onboard of a tethered airborne balloon. The second approach was development of a methodology to adapt a Numerical Weather Prediction (NWP) model to topography and land use classification changes of the open pit mine for more accurate meteorological simulations of ABL. The following subsections summarize the conclusions for each development followed by future work recommendations.

5.1 Meteorological Sensing

A novel airborne sensing system, called the Tethered And Navigated Air Blimp (TANAB) was enabled for meteorological measurements. TANAB is designed to be flexible, easy to deploy, and capable of measuring the profiles of atmospheric meteorological parameters including three components of wind velocity vector, temperature, relative humidity, and pressure. The system is also equipped with a compass to measure pitch, roll, and yaw angles at a high frequency of 10 Hz. These measurements were made using a weather station onboard called the TriSonicaTM Mini.

The weather station's performance is evaluated against industry standard sensors through a matrix of experiments in a wind tunnel. Series of tests were conducted to evaluate both the performance of TriSonicaTM Mini and the effect of the mounting platform (gondola) on the sensor's measurement. The sensor's measurements were compared against a reference Pitot tube and an ultrasonic R.M. YOUNG 81000 anemometer. TriSonicaTM Mini's accuracy in

measuring the wind speed was found to be dependent on the azimuth angle. TriSonica™ Mini underestimates the mean horizontal components of wind velocity. It also underestimates the turbulence statistics. On the other hand, the gondola influenced the measurements such that both mean wind velocity components and turbulence statistics were overestimated in the tunnel. It is likely that the platform introduced flow fluctuations so that the measured turbulence statistics were higher. Overall, the accuracy of the measurements were found to be deviated from the accuracies reported by the manufacturer. As a remedy, calibration equations were developed in this thesis to help correct the sensor measurements.

The instrument’s performance was quantitatively analyzed against a reference Pitot tube and a R.M. YOUNG 81000 anemometer using bias and Root Mean Square Error (RMSE) calculations. The bias ranged from -1.080 m s^{-1} to 0.138 m s^{-1} when the azimuth angle varied from 0° to 270° .

The weather station onboard of TANAB was deployed for 56 hours in May, 2018 at the mining facility in northern Canada. The operation covered the entire diurnal cycle. The measurements were corrected using the calibration coefficients. The diurnal variation of the horizontal wind speed \bar{S} , turbulence kinetic energy, and turbulence statistics (vertical momentum fluxes \overline{uw} and \overline{vw} , vertical sensible kinematic heat flux $\overline{w\theta}$, potential temperature variance $\overline{\theta^2}$, and vertical velocity variance $\overline{w^2}$) were observed in qualitative agreement with known ABL behaviour. The vertical momentum flux measured negative all the time indicating momentum sink into the surface due to skin drag. The vertical sensible kinematic heat flux on the other hand was negative at night while positive during the day. The observations confirm calm conditions at nights and early mornings when the atmosphere is thermally stable and gusty conditions in the mid afternoons when the atmosphere is thermally unstable. In addition, the profiles of the turbulence statistics were analyzed at 4-hour time intervals and 20-m vertical resolution covering the entire diurnal cycle.

5.2 Mesoscale Modelling

The data structure of a distribution of the Weather Research and Forecasting (WRF) model titled the Unified Environmental Modelling System (UEMS) was adapted with the topography and land use classification changes of the mining site for more accurate meteorological simulations. The simulations were conducted for three days in May 18, 24, and 30, 2018, when observation data were available for comparison. This thesis is primarily concerned with implementing the modelling methodology with some limited model comparisons to ob-

servations. A rigorous model assessment and comparison to observations is performed by Nahian et al. [53].

Updating the model topography with recent observations required incorporation of the Shuttle Radar Topography Mission (SRTM) and Light Detection And Ranging (LiDAR) observation datasets. The SRTM dataset provided a horizontal resolution of approximately 30 m, while the LiDAR dataset provided a horizontal resolution of approximately 1 m. To account for land use classification changes, a MODerate resolution Imaging Spectroradiometer (MODIS) land use 21 class at 30'' resolution dataset was ingested into the model. In addition, a lake model was activated to account for the meteorological effects of water bodies on site.

The simulation results were further investigated to study the model's sensitivity to the modifications in topography and land use datasets. Contours of wind speed, wind direction, surface potential temperature, surface relative humidity, albedo, roughness length, surface emissivity, and the water surface temperature across the lake are plotted for both stable and unstable atmosphere to further study the sensitivity of the forecasts as a function of the atmospheric stability.

The model's predictions of wind speed and wind direction at nighttime show that the wind speed is reduced significantly over the mine while the model predicts a circulation inside the pit. The wind speed, during this time, increases over the lake. The model's predictions of wind speed and wind direction show less sensitivity to change in topography and land use during the afternoon hours when the atmosphere is unstable. The wind direction remains unchanged over the facility and the wind magnitude slightly reduces around the mine area.

The contours of surface potential temperature show significant change at both nighttime and daytime. Potential temperature over the pond are warmer at night and colder at day compared to the surroundings. The relative humidity increases in the area between the mine and the pond during the night while it increases over the pond during the day. Studying the lake water temperature shows that the model accounts for the change in the water temperature.

The model meteorological outputs were further compared to results from six radiosonde launches, twice daily, from two radiosonde stations within the model domain. The stations are located in Fort Smith and Edmonton Stony Plain. The model profile comparisons of wind speed, wind direction, water vapor mixing ratio, and potential temperature to those of the sounding datasets were in reasonable agreement. Model comparisons to TANAB wind speeds also indicated improved predictions when accounting for topography and land use

classification changes of the mining site. The changes resulted in a bias reduction of 0.38 m s^{-1} in wind speed for the model.

5.3 Future Work

The TriSonicaTM Mini should be more rigorously tested under field conditions to reveal its performance against other reference measurements. This sensor should be further developed by the manufacturer for improved performance. The TANAB system should be further updated to improve the gondola performance. A new gondola has already been designed and manufactured. The updates increase the system performance in cold and warm conditions while protecting the sensors and data loggers from rain, severe wind, and cold conditions. The new gondola is almost half the weight of the existing gondola enabling TANAB to reach higher altitudes for measurement. TANAB should be further deployed in other complex terrains such as the urban and agricultural environments. When more accurate positioning systems are integrated into the system, TANAB measurements of wind velocity vector components can be transformed to a fixed reference frame on the earth.

As far as mesoscale modelling is involved, future adaptation of the model to complex terrains should involve parameterization of anthropogenic heat release near the surface to better account for atmosphere and land surface exchanges of energy, momentum, and species. Future mesoscale models should be further adapted to predict dispersion of area fugitive emissions of greenhouse gases in the atmosphere. The mesoscale models should also be tested rigorously given various parameterization options and resolutions against observations.

Bibliography

- [1] LIDAR. <https://www.esrl.noaa.gov/csd/groups/csd3/instruments/lidar/>. Accessed: 2019-05-13.
- [2] RADAR. <https://www.ametsoc.org/ams/index.cfm/education-careers/education-program/k-12-teachers/project-atmosphere/training-opportunities/project-atmosphere-peer-led-training/project-atmosphere-peer-training-resources/radar-modules/>. Accessed: 2019-05-13.
- [3] Radiosonde. <http://glossary.ametsoc.org/wiki/Radiosonde>. Accessed: 2019-04-29.
- [4] TriSonica™ Mini. <https://www.anemoment.com/>. Accessed: 2019-04-29.
- [5] Weather Research and Forecasting Model. <https://www.mmm.ucar.edu/weather-research-and-forecasting-model>. Accessed: 2019-04-29.
- [6] Weather Research and Forecasting Model User's Forum. <http://forum.wrfforum.com/viewtopic.php?f=22&t=2266>. Accessed: 2019-05-23.
- [7] ALIABADI, A. A. *Theory and Applications of Turbulence: A Fundamental Approach for Scientists and Engineers*. Amir A. Aliabadi Publications, Guelph, 2018.
- [8] ALIABADI, A. A., MORADI, M., CLEMENT, D., LUBITZ, W. D., AND GHARABAGHI, B. Flow and temperature dynamics in an urban canyon under a comprehensive set of wind directions, wind speeds, and thermal stability conditions. *Environmental Fluid Mechanics* 19, 1 (2019), 81–109.
- [9] ALIABADI, A. A., STAEBLER, R. M., DE GRANDPRÉ, J., ZADRA, A., AND VAILLANCOURT, P. A. Comparison of estimated atmospheric boundary layer mixing height in the Arctic and southern Great Plains under statically stable conditions: experimental and numerical aspects. *Atmos.-Ocean* 54, 1 (2016), 60–74.
- [10] ALIABADI, A. A., STAEBLER, R. M., LIU, M., AND HERBER, A. Characterization and parametrization of Reynolds stress and turbulent heat flux in the stably-stratified lower Arctic troposphere using aircraft measurements. *Bound.-Lay. Meteorol.* 161, 1 (2016), 99–126.

- [11] AXFORD, D. N. Aircraft measurements in the boundary layer. probing the atmospheric boundary layer. *American Meteorological Society* (1968), 39–55.
- [12] AXFORD, D. N. On the accuracy of wind measurements using an inertial platform in an aircraft, and an example of a measurement of the vertical mesostructure of the atmosphere. *Journal of Applied Meteorology* 7 (1968), 645–666.
- [13] BERMAN, E. A. Measurements of temperature and downwind spectra in the ‘buoyant subrange’. *Journal of the Atmospheric Sciences* 33, 3 (1976), 495–498.
- [14] BOU-ZEID, E., MENEVEAU, C., AND PARLANGE, M. B. Large-eddy simulation of neutral atmospheric boundary layer flow over heterogeneous surfaces: Blending height and effective surface roughness. *Water Resources Research* 40 (2004), W02505.
- [15] BROCK, F. V. *Meteorological measurement systems*. Oxford University Press, Oxford, 2001.
- [16] CANUT, G., COUVREUX, F., LOTHON, M., LEGAIN, D., PIGUET, B., LAMPERT, A., MAUREL, W., AND MOULIN, E. Turbulence fluxes and variances measured with a sonic anemometer mounted on a tethered balloon. *Atmospheric Measurement Techniques* 9, 9 (2016), 4375–4386.
- [17] CASSANO, J. J. Observations of atmospheric boundary layer temperature profiles with a small unmanned aerial vehicle. *Antarctic Science* 26 (2014), 205–213.
- [18] CHENG, F.-Y., AND BYUN, D. Investigation of the effects of different land use and land cover patterns on mesoscale meteorological simulations in the Taiwan area. *Journal of Applied Meteorology and Climatology* 52 (2013), 570–587.
- [19] CHENG, F.-Y., AND BYUN, D. W. Application of high resolution land use and land cover data for atmospheric modelling in the Houston-Galveston metropolitan area, Part I: meteorological simulation results. *Atmospheric Environment* 42 (2008), 7795–7811.
- [20] COOK, D. E., STRONG, P. A., GARRETT, S. A., AND MARSHALL, R. E. A small Unmanned Aerial System (UAS) for coastal atmospheric research: preliminary results from New Zealand. *Journal of the Royal Society of New Zealand* 43 (2012), 108–115.
- [21] DAVIDSON, B. The Barbados oceanographic and meteorological experiment. *Bulletin of the American Meteorological Society* 49, 9 (1968), 928–935.
- [22] DUDHIA, J. Numerical study of convection observed during the winter monsoon experiment using a mesoscale two-dimensional model. *Journal of the Atmospheric Sciences* 46, 20 (1989), 3077–3107.

- [23] EGERER, U., GOTTSCHALK, M., SIEBERT, H., EHRLICH, A., AND WENDISCH, M. The new BELUGA setup for collocated turbulence and radiation measurements using a tethered balloon: first applications in the cloudy arctic boundary layer. *Atmospheric Measurement Techniques* 12, 7 (2019), 4019–4038.
- [24] ELIASSON, I., OFFERLE, B., GRIMMOND, C. S. B., AND LINDQVIST, S. Wind fields and turbulence statistics in an urban street canyon. *Atmospheric Environment* 40 (2006), 1–16.
- [25] FRIEDL, M. A., SULLA-MENASHE, D., TAN, B., SCHNEIDER, A., RAMANKUTTY, N., SIBLEY, A., AND HUANGA, X. MODIS Collection 5 global land cover: Algorithm refinements and characterization of new datasets. *Proc. SPIE* 114, 1 (2010), 168–182.
- [26] FRIEDMAN, H. A., AND CALLAHAN, W. S. The ESSA research flight facility’s support of environmental research in 1969. *Weatherwise* 23, 4 (1970), 174–185.
- [27] GARSTANG, M., AND LA SEUR, N. E. the 1968 Barbados experiment. *Bulletin of the American Meteorological Society* 49, 6 (1968), 627–635.
- [28] GHAEMI-NASAB, M., FRANCHINI, S., DAVARI, A. R., AND SORRIBES-PALMER, F. A procedure for calibrating the spinning ultrasonic wind sensors. *Measurement* 114 (2018), 365–371.
- [29] GORDON, M., LI, S.-M., STAEBLER, R., DARLINGTON, A., HAYDEN, K., O’BRIEN, J., AND WOLDE, M. Determining air pollutant emission rates based on mass balance using airborne measurement data over the Alberta oil sands operations. *Atmospheric Measurement Technique* 8, 9 (2015), 3745–3765.
- [30] GU, H., JIN, J., WU, Y., AND EK, M. Calibration and validation of lake surface temperature simulations with the coupled WRF-lake model. *Climate Change* 129 (2013), 2–3.
- [31] HAUGEN, D. A., KAIMAL, J. C., READINGS, C. J., AND RAYMENT, R. A comparison of balloon-borne and tower-mounted instrumentation for probing the atmospheric boundary layer. *Journal of Applied Meteorology* 14, 4 (1975), 540–545.
- [32] HE, J., YU, Y., YU, L., LIU, N., AND ZHAO, S. Impacts of uncertainty in land surface information on simulated surface temperature and precipitation over China. *Int. J. Climatol.* 37 (2017), 829–847.
- [33] HE, Y. C., CHAN, P. W., AND LI, Q. S. Estimation of roughness length at Hong Kong International Airport via different micrometeorological methods. *Journal of Wind Engineering & Industrial Aerodynamics* 171 (2017), 121–136.
- [34] HEMINGWAY, B. L., FRAZIER, A. E., ELBING, B. R., AND JACOB, J. D. Vertical sampling scales for atmospheric boundary layer measurements from Small Unmanned Aircraft Systems (sUAS). *Atmosphere* 8 (2017), 176–192.

- [35] HOBBY, M. J. Turbulence measurements from a tethered balloon. Tech. rep., University of Leeds, School of Earth & Environment, Leeds, 2013.
- [36] HOLLAND, G. J., WEBSTER, P. J., CURRY, J. A., TYRELL, G., GAUNTLETT, D., BRETT, G., BECKER, J., HOAG, R., AND VAGLIANTI, W. The aerosonde robotic aircraft: A new paradigm for environmental observations. *Bulletin of the American Meteorological Society* 82 (2001), 889–902.
- [37] HOUSTON, A. L., ARGROW, B., ELSTON, J., LAHOWETZ, J., FREW, E. W., AND KENNEDY, P. C. The collaborative Colorado and Nebraska unmanned aircraft system experiment. *Bulletin of the American Meteorological Society* 93 (2012), 39–54.
- [38] HOUZE, R. A. Orographic effects on precipitating clouds. *Reviews of Geophysics* 50, 1 (2012), RG1001.
- [39] JACOB, J. D., CHILSON, P. B., HOUSTON, A. L., AND SMITH, S. W. Considerations for atmospheric measurements with Small Unmanned Aircraft Systems. *Atmosphere* 9, 7 (2018), 252–268.
- [40] JIMÉNEZ, P. A., AND DUDHIA, J. On the ability of the WRF model to reproduce the surface wind direction over complex terrain. *J. Appl. Meteorol. Clim.* 52, 7 (2013), 1610–1617.
- [41] JIMÉNEZ-ESTEVE, B., UDINA, M., SOLER, M. R., PEPIN, N., AND MIRÓ, J. R. Land use and topography influence in a complex terrain area: A high resolution mesoscale modelling study over the Eastern Pyrenees using the WRF model. *Atmospheric Research* 202 (2018), 49–62.
- [42] KLEIN, P., AND CLARK, J. V. Flow variability in a north american downtown street canyon. *Meteorological Applications* 46 (2007), 851–877.
- [43] KUMAR, P., BHATTACHARYA, B. K., AND PAL, P. Impact of vegetation fraction from Indian geostationary satellite on short-range weather forecast. *Agricultural and Forest Meteorology* 168 (2013), 82–92.
- [44] LAM, J., LAU, A., AND FUNG, J. Application of refined land-use categories for high resolution mesoscale atmospheric modelling. *Boundary-Layer Meteorology* 119 (2006), 263–288.
- [45] LAM, J., LAU, A., AND FUNG, J. Estimating the effects of increased urbanization on surface meteorology and ozone concentrations in the new york city metropolitan region. *Atmospheric Environment* 41 (2007), 1803–1818.
- [46] LIGGIO, J., LI, S.-M., HAYDEN, K., TAHA, Y. M., STROUD, C., DARLINGTON, A., DROLLETTE, B. D., GORDON, M., LEE, P., LIU, P., LEITHEAD, A., MOUSSA, S. G., WANG, D., O'BRIEN, J., MITTERMEIER, R. L., BROOK, J. R., LU, G.,

- STAEBLER, R. M., HAN, Y., TOKAREK, T. W., OSTHOFF, H. D., MAKAR, P. A., ZHANG, J., PLATA, D. L., AND GENTNER, D. R. Oil sands operations as a large source of secondary organic aerosols. *Nature* 534 (2016), 91–94.
- [47] LIN, Y.-L., FARLEY, R. D., AND ORVILLE, H. D. Bulk parameterization of the snow field in a cloud model. *Journal of Applied Meteorology and Climatology* 22, 6 (1983), 1065–1092.
- [48] LOTHON, M., LOHOU, F., PINO, D., COUVREUX, F., PARDYJAK, E. R., REUDER, J., VILÀ-GUERAU DE ARELLANO, J., DURAND, P., HARTOGENSIS, O., LEGAIN, D., AUGUSTIN, P., GIOLI, B., LENSCHOW, D. H., FALOONA, I., YAGÜE, C., ALEXANDER, D. C., ANGEVINE, W. M., BARGAIN, E., BARRIÉ, J., BAZILE, E., BEZOMBES, Y., BLAY-CARRERAS, E., VAN DE BOER, A., BOICHARD, J. L., BOURDON, A., BUTET, A., CAMPISTRON, B., DE COSTER, O., CUXART, J., DABAS, A., DARBIEU, C., DEBOUDT, K., DELBARRE, H., DERRIEN, S., FLAMENT, P., FOURMENTIN, M., GARAI, A., GIBERT, F., GRAF, A., GROEBNER, J., GUICHARD, F., JIMÉNEZ, M. A., JONASSEN, M., VAN DEN KROONENBERG, A., MAGLIULO, V., MARTIN, S., MARTINEZ, D., MASTRORILLO, L., MOENE, A. F., MOLINOS, F., MOULIN, E., PIETERSEN, H. P., PIGUET, B., PIQUE, E., ROMÁN-CASCÓN, C., RUFIN-SOLER, C., SAÏD, F., SASTRE-MARUGÁN, M., SEITY, Y., STEENEVELD, G. J., TOSCANO, P., TRAULLÉ, O., TZANOS, D., WACKER, S., WILDMANN, N., AND ZALDEI, A. The bllast field experiment: Boundary-layer late afternoon and sunset turbulence. *Atmospheric Chemistry and Physics* 14, 20 (2014), 10931–10960.
- [49] LUDLOW, J., MERRILL, C., RATCLIFFE, S., AND WOODS, G. Tethered Air Monitoring Balloon (TAMB) Final Design Report. Tech. rep., University of Guelph, Guelph, 2017.
- [50] MAYER, S., SANDVIK, A., JONASSEN, M. O., AND REUDER, J. Atmospheric profiling with the UAS SUMO: a new perspective for the evaluation of fine-scale atmospheric models. *Antarctic Science* 116 (2012), 15–26.
- [51] MEIJ, A. D., AND VINUESA, J. F. Impact of SRTM and Corine Land Cover data on meteorological parameters using WRF. *Atmospheric Research* 143 (2014), 351–370.
- [52] MILRAD, S. *Synoptic Analysis and Forecasting 1st Edition*. Elsevier, 2017.
- [53] NAHIAN, M. R., NAZEM, A., NAMBIAR, M. K., BYERLAY, R., MAHMUD, S., AND ALIABADI, A. A. Complex Meteorology over a Complex Mining Facility: Assessment of Topography, Land Use, Grid Resolution, and PBL Scheme Modifications in WRF. *Journal of Applied Meteorology and Climatology* (Under Review).
- [54] NAMBIAR, M. K., BYERLAY, R., NAZEM, A., NAHIAN, M. R., MORADI, M., AND ALIABADI, A. A. A Tethered And Navigated Air Blimp (TANAB) for observing the

- microclimate over a complex terrain. *Geoscientific Instrumentation, Methods and Data Systems Discussions* (2019), 1–31.
- [55] NTWALI, D., OGWANG, B. A., AND ONGOMA, V. The impacts of topography on spatial and temporal rainfall distribution over Rwanda based on WRF model. *Atmospheric and Climate Sciences* 6, 2 (2016), 145.
- [56] OKE, T. R. Street design and urban canopy layer climate. *Energy and Buildings* 11 (1998), 103–113.
- [57] OLESON, K. W., AND LAWRENCE, D. M. Technical Description of version 4.5 of the Community Land Model (CLM). Tech. rep., National Center for Atmospheric Research (NCAR), Boulder, 2013.
- [58] PINEDA, N., JORBA, O., JORGE, J., AND BALDASANO, J. M. Using NOAA AVHRR and SPOT VGT data to estimate surface parameters: Application to a mesoscale meteorological model. *International Journal of Remote Sensing* 25, 1 (2004), 129–143.
- [59] POLLARD, R. T. The joint air-sea interaction experiment: Jasin 1978. *Bulletin of the American Meteorological Society* 59, 10 (1978), 1310–1318.
- [60] RICHARDSON, S. A. Lewis Fry Richardson (1881-1953): a personal biography. *Journal of Conflict Resolution* 1, 3 (1957), 300–304.
- [61] SANTOS-ALAMILLOS, F. J., POZO-VÁZQUEZ, D., RUIZ-ARIAS, J. A., AND TOVAR-PESCADOR, J. Influence of land-use misrepresentation on the accuracy of WRF wind estimates: Evaluation of GLCC and CORINE land-use maps in southern Spain. *Atmospheric Research* 157 (2015), 17–28.
- [62] SKAMAROCK, W. C., KLEMP, J. B., DUDHIA, J., GILL, D. O., BARKER, D. M., DUDA, M. G., HUANG, X.-Y., WANG, W., AND POWERS, J. G. A Description of the Advanced Research WRF Version 3. Tech. rep., National Center for Atmospheric Research, Boulder, 2008.
- [63] SMITH, F. B. An analysis of vertical wind-fluctuations at heights between 500 and 5,000 ft. *Quarterly Journal of the Royal Meteorological Society* 87, 372 (1961), 180–193.
- [64] SODDELL, J. R., MCGUFFIE, K., AND HOLLAND, G. J. Inter-comparison of atmospheric soundings from the aerosonde and radiosonde. *Journal of Applied Meteorology* 43 (2004), 1260–1269.
- [65] STEVENS, W. R., SQUIER, W., MITCHELL, W., GULLETT, B. K., AND PRESSLEY, C. Measurement of motion corrected wind velocity using an aerostat lofted sonic anemometer. *Atmospheric Measurement Techniques Discussions* 6 (2013), 703–720.
- [66] STOCK, R., CLEMENT, D., AND DORSSERS, J. Tethered and Navigated Air Blimp: Gondola Design Final Design Report. Tech. rep., University of Guelph, Guelph, 2018.

- [67] STRIEDINGER, A. M. Wind farm effects on the atmosphere: A meso-scale and numerical modelling of the offshore boundary layer through parameterized turbine rotors. Tech. rep., Eindhoven University of Technology, Delft University of Technology, Eindhoven, 2014.
- [68] STULL, R. B. *An Introduction to Boundary Layer Meteorology*. Kluwer Academic Publishes, Dordrecht, 1988.
- [69] STULL, R. B. *Practical Meteorology: An Algebra-based Survey of Atmospheric Science*. The University of British Columbia, Vancouver, 2016.
- [70] STURGEON, M. C. Wind tunnel tests of some low-cost sonic anemometers. Tech. rep., National Oceanographic and Atmospheric Administration (NOAA), Sterling, 2005.
- [71] SUBIN, Z. M., RILEY, W. J., AND MIRONOV, D. An improved lake model for climate simulations: Model structure, evaluation, and sensitivity analyses in CESM1. *Journal of Advances in Modelling Earth Systems* 4, 1 (2012), M02001.
- [72] SUMIŃSKA, O. A. Application of a constant temperature anemometer for balloon-borne stratospheric turbulence soundings. Tech. rep., Leibniz Institute for Atmospheric Physics, Kühlungsborn, 2008.
- [73] TALBOT, C., BOU-ZEID, E., AND SMITH, J. Nested mesoscale large-eddy simulations with WRF: performance in real test cases. *Journal of Hydrometeorology* 13, 5 (2012), 1421–1441.
- [74] THOMPSON, N. Turbulence measurements over the sea by a tethered-balloon technique. *Quarterly Journal of the Royal Meteorological Society* 98, 418 (1972), 745–762.
- [75] THOMPSON, N. Tethered balloons. In: *Dobson F., Hasse L., Davis R. (eds) Air-Sea Interaction*. Springer, Boston, MA (1980), 589–604.
- [76] WILCZAK, J., ONCLEY, S., AND STAGE, S. Sonic anemometer tilt correction algorithms. *Boundary-Layer Meteorology* 99 (2001), 127–150.
- [77] YÁÑEZ-MORRONI, G., GIRONÁS, J., CANEO, M., DELGADO, R., AND GARREAUD, R. Using the weather research and forecasting (WRF) model for precipitation forecasting in an Andean region with complex topography. *Atmosphere* 9, 8 (2018), 304.
- [78] ZHENG, Y., ALAPATY, K., HERWEHE, J. A., DEL GENIO, A. D., AND NIYOGI, D. Improving high-resolution weather forecasts using the Weather Research and Forecasting (WRF) Model with an updated Kain-Fritsch scheme. *Monthly Weather Review* 144, 3 (2016), 833–860.

Appendix A

Source Codes

A.1 Fortran Program Converting ASCII to Binary¹

```
PROGRAM asc2bin

INTEGER isigned , i , j , endian , wordsize , nx , ny
REAL xllcorner , yllcorner , cellsize
INTEGER missvalue , nz
REAL scalefactor
ALLOCATABLE rarray ( : , : ) , iarray ( : , : ) , barray ( : , : )
CHARACTER :: head12

isigned = 1
endian = 0
wordsize = 2
scalefactor = 1.0
nz = 1
open ( 10 , file = ' / export / home / users / anazem / Fortran - ASCII To BIN /
      WRFLandUseEditedAsciiCombineVersion1ReadytoBinary . txt ' )
read ( 10 , * ) head12 , nx
read ( 10 , * ) head12 , ny
read ( 10 , * ) head12 , xllcorner
read ( 10 , * ) head12 , yllcorner
read ( 10 , * ) head12 , cellsize
read ( 10 , * ) head12 , missvalue
print * , ' nx , ny ' , nx , ny , xllcorner , yllcorner , cellsize , missvalue
allocate ( rarray ( nx , ny ) )
allocate ( iarray ( nx , ny ) )

do j = 1 , ny
read ( 10 , * ) iarray ( : , j )
end do
```

¹Acquired from [6]

```
do i = 1, nx
do j = 1, ny
  rarray(i,j)=iarray(i,ny-j+1)
end do
end do

do j = 1, ny
do i = 1, nx
  if(iarray(i,ny-j+1) .lt. 0) then
    rarray(i,j) = 0
  end if
end do
end do

call write_geogrid(rarray,nx,ny,nz, isigned , endian , scalefactor , wordsize)
print*, 'Rarray2', rarray(nx,ny)
deallocate(rarray)

stop
end
```

A.2 C Subroutine Converting ASCII to Binary²

```
/* File: write_geogrid.c
```

Sample subroutine to write an array into the geogrid binary format.

Side effects: Upon completion, a file named 00001-<NX>.00001-<NY> is created, where <NX> is the argument nx and <NY> is the argument ny, both in i5.5 format.

Notes: Depending on the compiler and compiler flags, the name of the write_geogrid() routine may need to be adjusted with respect to the number of trailing underscores when calling from Fortran.

Michael G. Duda, NCAR/MMM

```
*/
```

```
#include <stdlib.h>
#include <stdio.h>
#include <string.h>

#ifdef _UNDERSCORE
#define write_geogrid write_geogrid_
#endif
#ifdef _DOUBLEUNDERSCORE
#define write_geogrid write_geogrid__
#endif

#define BIG 0
#define LITTLE 1

int write_geogrid(
    float * rarray,          /* The array to be written */
    int * nx,                /* x-dimension of the array */
    int * ny,                /* y-dimension of the array */
    int * nz,                /* z-dimension of the array */
    int * isigned,          /* 0=unsigned data, 1=signed data */
    int * endian,           /* 0=big , 1=little */
    float * scalefactor,    /* value to divide array elements by before truncation to
        integers */
    int * wordsize )        /* number of bytes to use for each array element */
{
    int i, narray;
    int A2, B2;
    int A3, B3, C3;
    int A4, B4, C4, D4;
    unsigned int * iarray;
    unsigned char * barray;
```

²Acquired from [6]

```

char fname[24];
FILE * bfile;

narray = (*nx) * (*ny) * (*nz);

iarray = (unsigned int *)malloc(sizeof(int) * narray);
barray = (unsigned char *)malloc(sizeof(unsigned char) * narray * (*wordsize));

/* Scale real-valued array by scalefactor and convert to integers */
for (i=0; i<narray; i++)
    iarray[i] = (unsigned int)(rarray[i] / (*scalefactor));

/*
Set up byte offsets for each wordsize depending on byte order.
A, B, C, D give the offsets of the LSB through MSB (i.e., for
word ABCD, A=MSB, D=LSB) in the array from the beginning of a word
*/
if (*endian == BIG) {
    A2 = 0; B2 = 1;
    A3 = 0; B3 = 1; C3 = 2;
    A4 = 0; B4 = 1; C4 = 2; D4 = 3;
}
else {
    B2 = 0; A2 = 1;
    C3 = 0; B3 = 1; A3 = 2;
    D4 = 0; C4 = 1; B4 = 2; A4 = 3;
}

/* Place words into storage byte order */
switch(*wordsize) {
    case 1:
        for(i=0; i<narray; i++) {
            if (iarray[i] < 0 && *isigned) iarray[i] += (1 << 8);
            barray[(*wordsize)*i] = (unsigned char)(iarray[i] & 0xff);
        }
        break;

    case 2:
        for(i=0; i<narray; i++) {
            if (iarray[i] < 0 && *isigned) iarray[i] += (1 << 16);
            barray[(*wordsize)*i+A2] = (unsigned char)((iarray[i] >> 8) & 0xff);
            barray[(*wordsize)*i+B2] = (unsigned char)( iarray[i]          & 0xff);
        }
        break;

    case 3:
        for(i=0; i<narray; i++) {
            if (iarray[i] < 0 && *isigned) iarray[i] += (1 << 24);
            barray[(*wordsize)*i+A3] = (unsigned char)((iarray[i] >> 16) & 0xff);
            barray[(*wordsize)*i+B3] = (unsigned char)((iarray[i] >> 8)  & 0xff);
            barray[(*wordsize)*i+C3] = (unsigned char)( iarray[i]          & 0xff);
        }
}

```

```

        break;

    case 4:
        for(i=0; i<narray; i++) {
            if (iarray[i] < 0 && *isigned) iarray[i] += (1 << 32);
            barray[(*wordsize)*i+A4] = (unsigned char)((iarray[i] >> 24) & 0xff);
            barray[(*wordsize)*i+B4] = (unsigned char)((iarray[i] >> 16) & 0xff);
            barray[(*wordsize)*i+C4] = (unsigned char)((iarray[i] >> 8) & 0xff);
            barray[(*wordsize)*i+D4] = (unsigned char)( iarray[i]          & 0xff);
        }
        break;
}

sprintf(fname, "%5.5i-%5.5i.%5.5i-%5.5i", 1,*nx,1,*ny);

/* Write array to file */
bfile = fopen(fname, "wb");
fwrite(barray, sizeof(unsigned char), narray*(*wordsize), bfile);
fclose(bfile);

free(iarray);
free(barray);

return 0;
}

```

A.3 Linux Command Lines to Compile the Fortran Code³

```
gcc -D\_ UNDERSCORE -DBYTESWAP -DLINUX -DIO\_ NETCDF -DIO\_ BINARY -DIO\_ GRIB1 -D\_ GEOGRID -O -c write\_ geogrid.c
gfortran -c AsciiToBinary.f95
gfortran -o AsciiToBinary.exe AsciiToBinary.o write\_ geogrid.o
./AsciiToBinary.exe
```

³Acquired from [6]

A.4 Python Program for Fast Matrix Element Substitution⁴

```
import numpy
import random
import sys
import matplotlib.pyplot as plt
import numba

from numba import jit

OutputfileName="WRFLandUseEdited12.txt"
outputFile = open(OutputfileName, "w")

# Set "nopython" mode for best performance
FileName01="WRFLandUseEdited11.txt"

WRFTOPO = numpy.loadtxt(FileName01, usecols=[0, 1, 2])
WRFLon = WRFTOPO[:, 1]
WRFLat = WRFTOPO[:, 0]
WRFEle = WRFTOPO[:, 2]

FileName02="SouthGrasslandEditedReadyForSub.txt"

ResetCoordinate1 = numpy.loadtxt(FileName02, usecols=[0, 1, 2])
ResetLon = ResetCoordinate1[:, 1]
ResetLat = ResetCoordinate1[:, 0]
ResetEle = ResetCoordinate1[:, 2]

N = numpy.size(WRFLon)
M = numpy.size(ResetLon)

@jit(nopython=True, parallel=True)
def substitute(ResetEle, ResetLat, ResetLon, WRFLon, WRFLat, WRFEle, N, M):

    for i in range(0, N):
        print(i)
        for j in range(0, M):

            if numpy.abs(WRFLon[i]-ResetLon[j]) < 0.001 and numpy.abs(WRFLat[i]-ResetLat[j])
               <0.001:
                WRFEle[i]=ResetEle[j]
```

⁴Developed by the author.

```
    print(" Substitute Done!")
    #break
return WRFEle
```

```
print(substitute(ResetEle, ResetLat, ResetLon, WRFLon, WRFLat, WRFEle, N, M))
print(WRFEle)
for i in range(0, N):
    outputFile.write("%f\t%f\t%f\n" %
                    (WRFLat[i], WRFLon[i], WRFEle[i]))
```

A.5 Python Program Assigning Latitudes and Longitudes to the LiDAR Data⁵

```
import numpy
import random
import sys
import matplotlib.pyplot as plt

OutputfileName="GeneratedLong.txt"
outputFile = open(OutputfileName, "w")

OutputfileName1="GeneratedLat.txt"
outputFile1 = open(OutputfileName1, "w")

FileName01 = "MineCoordinate.txt"

MineTopo = numpy.loadtxt(FileName01, usecols=[0, 1, 2])
MineX = MineTopo[:, 0]
MineY = MineTopo[:, 1]
MineEle = MineTopo[:, 2]

MineXSorted=numpy.sort(MineX)
MineYSorted=numpy.sort(MineY)

M=numpy.size(MineX)

Q=MineXSorted[M-1]-MineXSorted[0]

N=MineYSorted[M-1]-MineYSorted[0]

DeltaTetaLong=((-111.653425)+112.025779)/Q
DeltaTetaLat=((57.408311)-(57.299783))/N

LatGenerated=numpy.zeros(M)
LongGenerated=numpy.zeros(M)

for i in range(0,M):
    LongGenerated[i]=-112.025779+(MineXSorted[i]-MineXSorted[0])*DeltaTetaLong
    LatGenerated[i]=57.299783+(MineYSorted[i]-MineYSorted[0])*DeltaTetaLat

for i in range(0,M):
    outputFile.write("%f\t\t\n" %
                    (LongGenerated[i]))

for i in range(0,M):
```

⁵Developed by the author.

```
outputFile1.write("%f\t_\n"%  
                  (LatGenerated[i]))
```

A.6 The Content of the Index File Created for Feeding High Resolution Terrain Topography to UEMS

```
type = continuous
signed = yes
projection = regular_ll
dx =0.00027777777785
dy =0.00027777777785
known_x = 1.0
known_y = 1.0
known_lat =56.49958333
known_lon =-112.9998611
wordsize = 2
tile_x = 7200
tile_y = 7200
endian=little
row_order=bottom_top
missing_value=-32768
tile_z = 1
tile_bdr=0
units="meters MSL"
description="SRTM 1-arc-second topography height"
```

A.7 Python Program Extracting Background Roughness Length⁶

```
# Code to extract Background Roughness Length from WRF at a single hour for a single domain

import netCDF4
import matplotlib.pyplot as plt
import datetime as dt
import numpy as np

# Load the NetCDF files for each saved time
wrfout='wrfout_d05_2018-05-30_18_00_00'

# Designate output file name and location
Outputfile="wrfout_d05_2018-05-30_18_00_00.txt"

nc = netCDF4.Dataset(wrfout)
nc.variables.keys()
#Print the list of available variables in the net CDF file , do not repeat this command
print(nc.variables.keys())

#Read WRF XLAT and XLONG
lat = nc.variables['XLAT'][:]
lon = nc.variables['XLONG'][:]
#Read WRF Roughness Length, Potential Temperature at 2m, and Wind Speed at 10m
Height = nc.variables['HGT'][:]
Land = nc.variables['LU_INDEX'][:]
Temperature = nc.variables['TH2'][:]
Velocity=nc.variables['S10_MEAN'][:]
RoughnessLength=nc.variables['ZNT'][:]
U10=nc.variables['U10_MEAN'][:]
V10=nc.variables['V10_MEAN'][:]

print('len(lat[0][0,:])=',len(lat[0,:][0]))
print('len(lon[0,:][0])=',len(lon[0][0,:]))

outputFile = open(Outputfile, "w")
outputFile.write("#0:i\t#1:j\t#2:lon[0][i][j]-(deg)\t#3:lat[0][i][j]-(deg)\t\t"
                "#4:Height[0][i][j]-(m)\t#5:Land_Use_Index\t#6:Potential_Temperature_(K)\t\t"
                "#7:Velocity_(m_s^-1)\t#8:Roughness_Length_(m)\t#9:U10_(m_s^-1)\t\t"
                "#10:V10_(m_s^-1)\n")

#First loop over latitudes
for j in range(0,len(lat[0,:][0])):
```

⁶Developed by the author.

```

#Second loop over longitudes
for i in range(0, len(lon[0][0, :])):
    print('i, j, lon[0][i][j], lat[0][i][j], Temperature[0][i][j]', j, i, lon[0][i][j], lat[0][i][j], Height[0][i][j])
    outputFile.write(
        "%0f\t%0f\t%.8f\t%.8f\t%.0f\t%.0f\t%.2f\t%.2f\t%.2f\t%.2f\t\n" \
        % (j, i, lon[0][i][j], lat[0][i][j], Height[0][i][j], Land[0][i][j], Temperature[0][i][j], Velocity[0][i][j],
            RoughnessLength[0][i][j], U10[0][i][j], V10[0][i][j]))

```

A.8 Python Program Comparing WRFOUT and Soundings (Horizontal Wind Speed)⁷

```
import numpy as np
import matplotlib.pyplot as plt
plt.rcParams.update({'figure.max_open_warning': 0})

#Define text and font

plt.rc('text', usetex=True)
plt.rc('font', family='Times_New_Roman', size='14')

#WRFOUTPUT Already Extracted and Listed in to Columns
filename2="wrfout_d01_2018-05-30_12_00_00.txt"
filename4="wrfout_d01_2018-05-24_12_00_00.txt"
filename5="wrfout_d01_2018-05-18_12_00_00.txt"

data2 = np.loadtxt(filename2)
data4 = np.loadtxt(filename4)
data5 = np.loadtxt(filename5)

#For Horizontal Wind Speed Three-day Averaging is Considered
Time_Mine1=data2[:,0]
Altitude_Mine1=(data2[:,1]+data4[:,1]+data5[:,1])/3
PTWRF=(data2[:,9]+data4[:,9]+data5[:,9])/3

#SOUNDING Data
filename7="71934_YSM_Fort_Smith_Observations_at_12Z_18_May_2018.txt"
filename8="71934_YSM_Fort_Smith_Observations_at_12Z_24_May_2018.txt"
filename9="71934_YSM_Fort_Smith_Observations_at_12Z_30_May_2018.txt"

data7 = np.loadtxt(filename7)
data8 = np.loadtxt(filename8)
data9 = np.loadtxt(filename9)

AveragedAltitude=(data7[:,0]+data8[:,0]+data9[:,0])/3

#For Horizontal Wind Speed Three-day Averaging is Considered
Altitude_Mine2=0.3048*(1-(AveragedAltitude/934)** 0.190284)* 145366.45
```

⁷Developed by the author.

```

S_Mine2=(data7[:,7]+data8[:,7]+data9[:,7])/(3*1.943844)
PTObsereved=(data7[:,8]+data8[:,8]+data9[:,8])/(3)

fig = plt.figure()

plt.plot(PTWRF, Altitude_Mine1, color='m', marker='>', markersize=2, markerfacecolor='m',
         linewidth=0.6, label='WRF')
plt.plot(PTObsereved, Altitude_Mine2, color='g', marker='^', markersize=2, markerfacecolor='g',
         linewidth=0.6, label='Edmonton_Stony_Plain_Observations')
plt.xlabel('Horizontal_Wind_Speed [m_s$^{-1}$]', fontsize=16)
plt.ylabel('Altitude [m]', fontsize=16)
plt.legend(fontsize='10.5')
fig.tight_layout()
plt.savefig('Averaged_Horizontal_Wind_Speed.png', dpi=800)
fig.show()

plt.show()

```

A.9 Python Program Calibrating TriSonicaTM Mini against Pitot Tube⁸

```
import random
import sys
import os
import numpy
import matplotlib.pyplot as plt
import matplotlib.dates as mdates
import datetime
from scipy.cluster.hierarchy import dendrogram, linkage
import latex
```

```
#Reading TriSonica Data Files
```

```
#-----
fileNameEX1T1WL1 = "T2JAN15EXP9WL1.txt"
fileNameEX1T1WL2 = "T2JAN15EXP9WL2.txt"
fileNameEX1T1WL3 = "T2JAN15EXP9WL3.txt"
fileNameEX1T1WL4 = "T2JAN15EXP9WL4.txt"
```

```
fileNameEX2T1WL1 = "T2EXP1WL1.txt"
fileNameEX2T1WL2 = "T2EXP1WL2.txt"
fileNameEX2T1WL3 = "T2EXP1WL3.txt"
fileNameEX2T1WL4 = "T2EXP1WL4.txt"
```

```
fileNameEX3T1WL1 = "T2EXP2WL1.txt"
fileNameEX3T1WL2 = "T2EXP2WL2.txt"
fileNameEX3T1WL3 = "T2EXP2WL3.txt"
fileNameEX3T1WL4 = "T2EXP2WL4.txt"
```

```
fileNameEX4T1WL1 = "T2EXP3WL1.txt"
fileNameEX4T1WL2 = "T2EXP3WL2.txt"
fileNameEX4T1WL3 = "T2EXP3WL3.txt"
fileNameEX4T1WL4 = "T2EXP3WL4.txt"
```

```
#Reading Pitot Tube Data Files
```

```
#-----
fileNameEX1PWL1 = "PJAN15EXP9WL1.txt"
fileNameEX1PWL2 = "PJAN15EXP9WL2.txt"
fileNameEX1PWL3 = "PJAN15EXP9WL3.txt"
fileNameEX1PWL4 = "PJAN15EXP9WL4.txt"
```

```
fileNameEX2PWL1 = "PEXP1WL1.txt"
fileNameEX2PWL2 = "PEXP1WL2.txt"
fileNameEX2PWL3 = "PEXP1WL3.txt"
```

⁸Developed by the author.

```
fileNameEX2PWL4 = "PEXP1WL4.txt"
```

```
fileNameEX3PWL1 = "PEXP2WL1.txt"
```

```
fileNameEX3PWL2 = "PEXP2WL2.txt"
```

```
fileNameEX3PWL3 = "PEXP2WL3.txt"
```

```
fileNameEX3PWL4 = "PEXP2WL4.txt"
```

```
fileNameEX4PWL1 = "PEXP3WL1.txt"
```

```
fileNameEX4PWL2 = "PEXP3WL2.txt"
```

```
fileNameEX4PWL3 = "PEXP3WL3.txt"
```

```
fileNameEX4PWL4 = "PEXP3WL4.txt"
```

#Reading TriSonica Data Column

```
#
```

```
DataT1EXP1WL1=numpy.loadtxt(fileNameEX1T1WL1, usecols=[0,1,2,3,4,5,6])
```

```
DataT1EXP1WL2=numpy.loadtxt(fileNameEX1T1WL2, usecols=[0,1,2,3,4,5,6])
```

```
DataT1EXP1WL3=numpy.loadtxt(fileNameEX1T1WL3, usecols=[0,1,2,3,4,5,6])
```

```
DataT1EXP1WL4=numpy.loadtxt(fileNameEX1T1WL4, usecols=[0,1,2,3,4,5,6])
```

```
DataT1EXP2WL1=numpy.loadtxt(fileNameEX2T1WL1, usecols=[0,1,2,3,4,5,6])
```

```
DataT1EXP2WL2=numpy.loadtxt(fileNameEX2T1WL2, usecols=[0,1,2,3,4,5,6])
```

```
DataT1EXP2WL3=numpy.loadtxt(fileNameEX2T1WL3, usecols=[0,1,2,3,4,5,6])
```

```
DataT1EXP2WL4=numpy.loadtxt(fileNameEX2T1WL4, usecols=[0,1,2,3,4,5,6])
```

```
DataT1EXP3WL1=numpy.loadtxt(fileNameEX3T1WL1, usecols=[0,1,2,3,4,5,6])
```

```
DataT1EXP3WL2=numpy.loadtxt(fileNameEX3T1WL2, usecols=[0,1,2,3,4,5,6])
```

```
DataT1EXP3WL3=numpy.loadtxt(fileNameEX3T1WL3, usecols=[0,1,2,3,4,5,6])
```

```
DataT1EXP3WL4=numpy.loadtxt(fileNameEX3T1WL4, usecols=[0,1,2,3,4,5,6])
```

```
DataT1EXP4WL1=numpy.loadtxt(fileNameEX4T1WL1, usecols=[0,1,2,3,4,5,6])
```

```
DataT1EXP4WL2=numpy.loadtxt(fileNameEX4T1WL2, usecols=[0,1,2,3,4,5,6])
```

```
DataT1EXP4WL3=numpy.loadtxt(fileNameEX4T1WL3, usecols=[0,1,2,3,4,5,6])
```

```
DataT1EXP4WL4=numpy.loadtxt(fileNameEX4T1WL4, usecols=[0,1,2,3,4,5,6])
```

#Averaging the TriSonica Absolute Wind Velocity

```
#
```

```
UABSDDataT1EXP1WL1=numpy.average(DataT1EXP1WL1[:, 6])
```

```
UABSDDataT1EXP1WL2=numpy.average(DataT1EXP1WL2[:, 6])
```

```
UABSDDataT1EXP1WL3=numpy.average(DataT1EXP1WL3[:, 6])
```

```
UABSDDataT1EXP1WL4=numpy.average(DataT1EXP1WL4[:, 6])
```

```
UABSDDataTEXP1=numpy.zeros((1,4))
```

```
UABSDDataTEXP1=[UABSDDataT1EXP1WL1, UABSDDataT1EXP1WL2, UABSDDataT1EXP1WL3, UABSDDataT1EXP1WL4]
```

```
UABSDDataT1EXP2WL1=numpy.average(DataT1EXP2WL1[:, 6])
```

```
UABSDDataT1EXP2WL2=numpy.average(DataT1EXP2WL2[:, 6])
```

```
UABSDDataT1EXP2WL3=numpy.average(DataT1EXP2WL3[:, 6])
```

```

UABSDDataT1EXP2WL4= numpy . average (DataT1EXP2WL4 [: , 6])

UABSDDataT1EXP2= numpy . zeros ((1,4))
UABSDDataT1EXP2=[UABSDDataT1EXP2WL1, UABSDDataT1EXP2WL2, UABSDDataT1EXP2WL3, UABSDDataT1EXP2WL4]

UABSDDataT1EXP3WL1= numpy . average (DataT1EXP3WL1 [: , 6])
UABSDDataT1EXP3WL2= numpy . average (DataT1EXP3WL2 [: , 6])
UABSDDataT1EXP3WL3= numpy . average (DataT1EXP3WL3 [: , 6])
UABSDDataT1EXP3WL4= numpy . average (DataT1EXP3WL4 [: , 6])

UABSDDataT1EXP3= numpy . zeros ((1,4))
UABSDDataT1EXP3=[UABSDDataT1EXP3WL1, UABSDDataT1EXP3WL2, UABSDDataT1EXP3WL3, UABSDDataT1EXP3WL4]

UABSDDataT1EXP4WL1= numpy . average (DataT1EXP4WL1 [: , 6])
UABSDDataT1EXP4WL2= numpy . average (DataT1EXP4WL2 [: , 6])
UABSDDataT1EXP4WL3= numpy . average (DataT1EXP4WL3 [: , 6])
UABSDDataT1EXP4WL4= numpy . average (DataT1EXP4WL4 [: , 6])

UABSDDataT1EXP4= numpy . zeros ((1,4))
UABSDDataT1EXP4=[UABSDDataT1EXP4WL1, UABSDDataT1EXP4WL2, UABSDDataT1EXP4WL3, UABSDDataT1EXP4WL4]

```

#Reading the Pitot Tube Data Columns

#

```

DataPEXP1WL1= numpy . loadtxt (fileNameEX1PWL1 , usecols =[0,1,2,3,4,5,7])
DataPEXP1WL2= numpy . loadtxt (fileNameEX1PWL2 , usecols =[0,1,2,3,4,5,7])
DataPEXP1WL3= numpy . loadtxt (fileNameEX1PWL3 , usecols =[0,1,2,3,4,5,7])
DataPEXP1WL4= numpy . loadtxt (fileNameEX1PWL4 , usecols =[0,1,2,3,4,5,7])

DataPEXP2WL1= numpy . loadtxt (fileNameEX2PWL1 , usecols =[0,1,2,3,4,5,6])
DataPEXP2WL2= numpy . loadtxt (fileNameEX2PWL2 , usecols =[0,1,2,3,4,5,6])
DataPEXP2WL3= numpy . loadtxt (fileNameEX2PWL3 , usecols =[0,1,2,3,4,5,6])
DataPEXP2WL4= numpy . loadtxt (fileNameEX2PWL4 , usecols =[0,1,2,3,4,5,6])

DataPEXP3WL1= numpy . loadtxt (fileNameEX3PWL1 , usecols =[0,1,2,3,4,5,6])
DataPEXP3WL2= numpy . loadtxt (fileNameEX3PWL2 , usecols =[0,1,2,3,4,5,6])
DataPEXP3WL3= numpy . loadtxt (fileNameEX3PWL3 , usecols =[0,1,2,3,4,5,6])
DataPEXP3WL4= numpy . loadtxt (fileNameEX3PWL4 , usecols =[0,1,2,3,4,5,6])
#
DataPEXP4WL1= numpy . loadtxt (fileNameEX4PWL1 , usecols =[0,1,2,3,4,5,6])
DataPEXP4WL2= numpy . loadtxt (fileNameEX4PWL2 , usecols =[0,1,2,3,4,5,6])
DataPEXP4WL3= numpy . loadtxt (fileNameEX4PWL3 , usecols =[0,1,2,3,4,5,6])
DataPEXP4WL4= numpy . loadtxt (fileNameEX4PWL4 , usecols =[0,1,2,3,4,5,6])

```

#Converting the Pitot Tube Voltage OUTPUT to Wind Speed Based on the Calibration Factors and the Bernoulli Equation

#

```

UABSDDataPEXP1WL1=(( numpy . average (DataPEXP1WL1 [: , 6]) *12.458*2)/(1000*1.225))**.5
UABSDDataPEXP1WL2=(( numpy . average (DataPEXP1WL2 [: , 6]) *12.458*2)/(1000*1.225))**.5
UABSDDataPEXP1WL3=(( numpy . average (DataPEXP1WL3 [: , 6]) *12.458*2)/(1000*1.225))**.5
UABSDDataPEXP1WL4=(( numpy . average (DataPEXP1WL4 [: , 6]) *12.458*2)/(1000*1.225))**.5

```

```

UABSDDataPEXP1=numpy.zeros((1,4))
UABSDDataPEXP1=[UABSDDataPEXP1WL1, UABSDDataPEXP1WL2, UABSDDataPEXP1WL3, UABSDDataPEXP1WL4]

UABSDDataPEXP2WL1=((numpy.average(DataPEXP2WL1[:, 6])*12.458*2)/(1000*1.225))**0.5
UABSDDataPEXP2WL2=((numpy.average(DataPEXP2WL2[:, 6])*12.458*2)/(1000*1.225))**0.5
UABSDDataPEXP2WL3=((numpy.average(DataPEXP2WL3[:, 6])*12.458*2)/(1000*1.225))**0.5
UABSDDataPEXP2WL4=((numpy.average(DataPEXP2WL4[:, 6])*12.458*2)/(1000*1.225))**0.5

UABSDDataPEXP2=numpy.zeros((1,4))
UABSDDataPEXP2=[UABSDDataPEXP2WL1, UABSDDataPEXP2WL2, UABSDDataPEXP2WL3, UABSDDataPEXP2WL4]

UABSDDataPEXP3WL1=((numpy.average(DataPEXP3WL1[:, 6])*12.458*2)/(1000*1.225))**0.5
UABSDDataPEXP3WL2=((numpy.average(DataPEXP3WL2[:, 6])*12.458*2)/(1000*1.225))**0.5
UABSDDataPEXP3WL3=((numpy.average(DataPEXP3WL3[:, 6])*12.458*2)/(1000*1.225))**0.5
UABSDDataPEXP3WL4=((numpy.average(DataPEXP3WL4[:, 6])*12.458*2)/(1000*1.225))**0.5

UABSDDataPEXP3=numpy.zeros((1,4))
UABSDDataPEXP3=[UABSDDataPEXP3WL1, UABSDDataPEXP3WL2, UABSDDataPEXP3WL3, UABSDDataPEXP3WL4]

UABSDDataPEXP4WL1=((numpy.average(DataPEXP4WL1[:, 6])*12.458*2)/(1000*1.225))**0.5
UABSDDataPEXP4WL2=((numpy.average(DataPEXP4WL2[:, 6])*12.458*2)/(1000*1.225))**0.5
UABSDDataPEXP4WL3=((numpy.average(DataPEXP4WL3[:, 6])*12.458*2)/(1000*1.225))**0.5
UABSDDataPEXP4WL4=((numpy.average(DataPEXP4WL4[:, 6])*12.458*2)/(1000*1.225))**0.5

UABSDDataPEXP4=numpy.zeros((1,4))
UABSDDataPEXP4=[UABSDDataPEXP4WL1, UABSDDataPEXP4WL2, UABSDDataPEXP4WL3, UABSDDataPEXP4WL4]

```

```
#Passing the Linear Trendlines
```

```
#
```

```

Z1=numpy.polyfit(UABSDDataPEXP1,UABSDDataTEXP1,1)
Dummy=[2,4,6,8,10]
Y1=numpy.polyval(Z1,Dummy)

Z2=numpy.polyfit(UABSDDataPEXP2,UABSDDataTEXP2,1)
Dummy=[2,4,6,8,10]
Y2=numpy.polyval(Z2,Dummy)
#
Z3=numpy.polyfit(UABSDDataPEXP3,UABSDDataTEXP3,1)
Dummy=[2,4,6,8,10]
Y3=numpy.polyval(Z3,Dummy)
#
Z4=numpy.polyfit(UABSDDataPEXP4,UABSDDataTEXP4,1)
Dummy=[2,4,6,8,10]
Y4=numpy.polyval(Z4,Dummy)

```

```

plt.rc('text', usetex=True)
plt.rc('font', family='serif')
#

```

```

fig = plt.figure(figsize=(5,3))
plt.rc('grid', linestyle="—", color='gray')
plt.plot( UABSDDataPEXP1,UABSDDataTEXP1, '+', markersize=12,

)
plt.plot( UABSDDataPEXP2,UABSDDataTEXP2, '+', markersize=12, markeredgecolor='gray')
plt.plot( UABSDDataPEXP3,UABSDDataTEXP3, '+', markersize=12, markeredgecolor='blue')
plt.plot( UABSDDataPEXP4,UABSDDataTEXP4, '+', markersize=12, markeredgecolor='red')

Y10=[0,2,4,6,8,10,12]
Dummy10=[0,2,4,6,8,10,12]

plt.ylabel( '\\textbf{TriSonica}_{m_s^{-1}}', fontsize=18)
plt.xlabel( '\\textbf{Pitot_Tube}_{m_s^{-1}}', fontsize=18)
ax = plt.gca()
ax.tick_params(axis='x', which='major', labelsize=18)
ax.tick_params(axis='y', which='major', labelsize=18)
plt.grid(True)
# plt.xlim(0,12)
# plt.ylim(0,12)

plt.plot(Dummy,Y1, label='Elevation_Angle=0^\circ',linewidth=2)

plt.plot(Dummy,Y2, label='Elevation_Angle=10^\circ',linewidth=2)
#
plt.plot(Dummy,Y3, label='Elevation_Angle=20^\circ',linewidth=2)

plt.plot(Dummy,Y4, label='Elevation_Angle=30^\circ',linewidth=2)

plt.legend(loc='best', bbox_to_anchor=(1.1175, 1.1), fontsize=9)
plt.plot(Dummy10,Y10,linewidth=3)

fig.show()
plt.show()

```

Appendix B

Published Work

B.1 Peer-Reviewed Journal Papers

1. Nazem, A., Lubitz, W. D., Aliabadi, A. A., Performance Characterization of a Mini Ultrasonic Anemometer in a Wind Tunnel. *Environmental Fluid Mechanics*, (in preparation).
2. Nahian, M. R., Nazem, A., Nambiar, M. K., Byerlay, R., Mahmud, S., Seguin, M., Robe, F., Ravenhill, J., and Aliabadi, A. A., Complex Meteorology over a Complex Mining Facility: Assessment of Topography, Land Use, Grid Resolution, and PBL Scheme Modifications in WRF. *Applied Meteorology and Climatology*, (under review).
3. Nambiar, M. K., Byerlay, R., Nazem, A., Nahian, M. R., Moradi, M., and Aliabadi, A. A., A Tethered And Navigated Air Blimp (TANAB) for Observing the Microclimate over a Complex Terrain. *Geoscientific Instrumentation, Methods and Data Systems*, (under review).
4. Byerlay, R., Nambiar, M. K., Nazem, A., Nahian, M. R., Biglarbegan, M., and Aliabadi, A. A., An Imaging Technique to Identify Land Surface Temperatures Using Oblique Angle Airborne Observations. *International Journal of Remote Sensing and Remote Sensing Letters*, (under review).
5. Moradi, M., Dyer, B., Nazem, A., Nambiar, M. K., Nahian, M. R., Bueno, B., Mackey, C., Vasathakumar, S., Nazarian, N., Krayenhoff, E. S., Norford, L. K., and Aliabadi, A. A., The Vertical City Weather Generator (VCWG v1.0.0). *Geoscientific Model Development*, (under review).

B.2 Refereed Conferences

1. Nahian, M. R., Nazem, A., Moradi, M., Mahmud, S., Lubitz, W. D., and Aliabadi, A. A., WRF Simulations of Urban Climate: Do We Need Low or High Topographic Resolution? In *Proceedings of The Joint Canadian Society for Mechanical Engineering (CSME) and CFD Society of Canada (CFDSC) International Congress (2019)*, London, Ontario, Canada.
2. Moradi, M., Kizhakkeniyil, M. K., Nazem, A., Nahian, M. R., Lubitz, W. D., and Aliabadi, A. A., A Vertical Diffusion Model to Predict Profiles of Temperature within the Lower Atmospheric Surface Layer: Simple or Complicated? In *Proceedings of The Joint Canadian Society for Mechanical Engineering (CSME) and CFD Society of Canada (CFDSC) International Congress (2019)*, London, Ontario, Canada.

B.3 Poster Presentations

1. Nazem, A., Nahian, M. R., Nambiar, M. K., Byerlay, R., and Aliabadi, A. A., Complex Meteorology over a Complex Mining Facility. In *Proceedings of The 27th IUGG General Assembly (2019)*, Montréal, Québec, Canada.